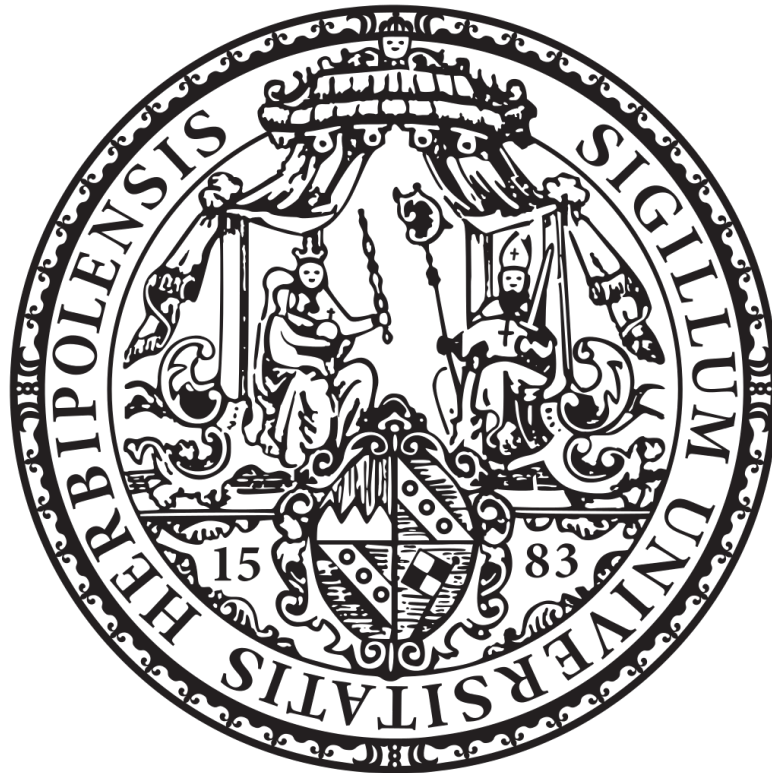


JULIUS-MAXIMILIANS-UNIVERSITÄT WÜRZBURG

Variability Study of High-Peaked BL Lac Objects at Millimeter Wavelengths



by

Florian Eppel

A thesis submitted in partial fulfillment for the
degree of Master of Science

in the

Faculty of Physics and Astronomy

Chair of Astronomy

Supervisor: Prof. Dr. Matthias Kadler

December 2021

“Any measurement that you make without the knowledge of its uncertainty is completely meaningless.”

Walter Lewin

Zusammenfassung

Aktive Galaxienkerne (AGK) zählen zu den stärksten Strahlungsquellen im Universum. In ihrem Zentrum befindet sich ein supermassereiches schwarzes Loch, das Materie akkretiert. Dazu zählen geladene Teilchen, die im extremen Gravitationspotential beschleunigt werden und dadurch Multiwellenlängen-Strahlung vom Radio- bis hin zum γ -Bereich emittieren. Beobachtungen von AGKs erlauben es Astronomen, physikalische Prozesse unter extremen Bedingungen zu untersuchen und so die Entstehung und Entwicklung des Universums zu studieren. Eine interessante Unterklasse der AGKs sind Blazare, welche hochrelativistische, kollimierte Plasmastrahlen (Jets) aufweisen, die direkt in Richtung der Erde zeigen. Ihr Spektrum zeigt eine charakteristische Doppelhöckerstruktur. Das erste Maximum ihres Spektrums liegt im Radio bis Fern-Infrarot Bereich und wird Synchrotron-Strahlung zugeordnet, während das zweite Maximum bei höheren Energien (“High-Energy”) liegt. Die für diese Arbeit relevanten Quellen sind “High-Peaked” BL Lac Objekte (HBLs), eine Unterklasse der Blazare, welche ihre Synchrotron Peak-Frequenz bei $\nu > 10^{15}$ Hz aufweisen. Einige dieser Quellen zeigen sogar deutlich höhere Synchrotron Peak-Frequenzen, zumindest während temporärer Strahlungsausbrüche (Flares), und werden als extreme Blazare (XBLs) bezeichnet. Diese Quellen sind, aufgrund ihrer starken High-Energy Emission im γ -Bereich und “Very-High-Energy” (VHE) Emission im TeV-Bereich besonders spannend. Diese High-Energy Strahlung ist zudem korreliert mit anderen Wellenlängenbereichen, wie z.B. dem Radiobereich (Lico et al., 2017), was sie zu primären Forschungszielen für die Multiwellenlängen-Astronomie macht. Für diese Arbeit wurde eine Auswahl von 18 XBLs und 12 HBLs mit dem Effelsberg 100-m Teleskop im Rahmen des TELAMON Projekts (Kadler et al., 2021) seit August 2020 alle zwei bis vier Wochen beobachtet. Die Beobachtungen wurden bei mehreren Radiofrequenzen im Bereich von 19 GHz bis 44 GHz durchgeführt. Die Auswertung der Daten der ersten ~ 1.2 Jahre (bis Oktober 2021) wird präsentiert und die Flussdichten auf Variabilität untersucht. Zusätzlich wird der zeitliche Verlauf der Spektralindizes analysiert und potentielle Flares untersucht. Im Vergleich zu einer Studie von Blazaren mit geringerer Synchrotron Peak-Frequenz (LBLs) und FSRQs (Flat Spectrum Radio Quasars) auf Basis von F-GAMMA

Daten (Fuhrmann et al., 2016; Angelakis et al., 2019) stellt sich heraus, dass HBLs und XBLs signifikant weniger Variabilität aufweisen. Auch die spektrale Variabilität ist geringer. Invertierte Spektren mit Spektralindex $\alpha > 0.25$ sind bei XBLs und HBLs deutlich seltener als bei LBLs und FSRQs. Für alle detektierten Flares wurden Variabilitäts-Dopplerfaktoren berechnet, welche alle geringer sind, als spektrale Modelle unter Berücksichtigung von High-Energy Daten aus der Literatur vorhersagen. Dies ist typisch für Blazare, die von der Doppler-Krise betroffen sind und trifft für alle HBLs und XBLs zu, von denen Variabilitäts-Dopplerfaktoren bestimmt werden konnten.

Abstract

Active galactic nuclei (AGN) are amongst the most powerful phenomena in the Universe. Their central engine is a super massive black hole that accretes matter including charged particles. These particles are accelerated by the extreme gravitational potential and emit multiwavelength-radiation from radio to γ -rays through various physical processes. Observations of AGN allow astronomers to investigate physics under extreme conditions, which is essential to study the formation and evolution of the Universe. A very interesting subclass of AGN are Blazars which exhibit highly relativistic, collimated plasma jets pointed directly towards Earth. Their spectral energy distribution shows a double-humped structure, with one peak in the radio to far-infrared, attributed to synchrotron emission, and another peak in the high-energy regime. The sources of interest for this thesis are High-Peaked BL Lac objects (HBLs), a subclass of Blazars, which have a synchrotron peak frequency $\nu > 10^{15}$ Hz. Some of them exhibit even higher synchrotron peak frequencies, at least during major flares, and are therefore characterized as Extreme Blazars (XBLs). What makes these sources particularly interesting is their bright high-energy emission in γ -rays and up to very-high-energy (VHE) in the TeV-range, known to be correlated with emission in the radio (Lico et al., 2017). For this thesis, a sample of 18 XBLs and 12 HBLs was observed with the Effelsberg 100-m telescope as part of the TELAMON program (Kadler et al., 2021) every two to four weeks since August 2020. The observations were done at multiple radio frequencies from 19 GHz to 44 GHz. The data of the first ~ 1.2 years (until October 2021) are analyzed and intrinsic modulation indices and spectral indices derived. On top of that, a flare analysis is performed. Comparing the results with previous studies of low-peaked BL Lacs and Flat Spectrum Radio Quasars (FSRQs) by the F-GAMMA program (Fuhrmann et al., 2016; Angelakis et al., 2019), one finds that HBLs and XBLs exhibit less variability in flux density and spectral indices. Significantly inverted spectra with spectral indices $\alpha > 0.25$ are very rare for HBLs and XBLs while they are not uncommon for lower peaked sources and FSRQs. From the flare analysis, variability Doppler factors are derived, which are comparably low to what SED studies suggest for the flaring sources, typical for Blazars affected by the Doppler Crisis.

Contents

Zusammenfassung	ii
Abstract	iv
Abbreviations	vii
1 Introduction	1
2 Active Galactic Nuclei	3
2.1 AGN Unification Model	4
2.2 Classification of AGN - The AGN Zoo	5
2.3 Radiative Processes in AGN	7
2.3.1 Synchrotron Radiation	8
2.3.2 Relativistic Beaming	13
2.3.3 High-Energy Emission	14
2.4 Blazars	15
2.4.1 The Blazar Sequence	15
2.4.2 Extreme Blazars	16
2.4.3 Doppler Crisis	18
2.4.4 Neutrino-Blazar Associations	18
3 Observations & Data Reduction	20
3.1 The Effelsberg 100-m Telescope	21
3.2 Technical Background	22
3.3 General Observing Procedure & Sample	24
3.4 Raw Data Reduction	26
3.4.1 Sub-scan Fitting	26
3.4.2 Data Corrections	30
3.4.3 Calibration	32
3.4.3.1 Calibrator Sources	32
3.4.3.2 Calibration Procedure	33
3.4.3.3 Calibration Cross Check	36
3.4.4 Error Discussion	36
3.5 Analysis	39
3.5.1 Spectral Index Calculation	39
3.5.2 Light Curves & Sub-band Averaging	40

4	Results	43
4.1	Light Curve Variability	43
4.1.1	Variability Measures	43
4.1.2	Likelihood Approach to the Intrinsic Modulation Index	44
4.1.3	Intrinsic Modulation Indices of HBL and Extreme Blazars	46
4.2	Spectral Indices of HBL and Extreme Blazars	50
4.3	Flare Analysis	54
4.3.1	Flare Detection	54
4.3.2	Variability Doppler Factors	56
5	Discussion	58
5.1	Modulation Index	58
5.2	Spectral Index	61
5.3	Flare Analysis	63
6	Summary & Outlook	65
	Bibliography	68
A	Averaged Light Curves	73
B	Spectra	80
C	Intrinsic Modulation Index	87
D	Calibration Factor Evolution	93
E	Tables	95
E.1	Spectral Indices	95
E.2	Intrinsic Modulation Indices	101
E.3	Raw TELAMON Flux Density Data	103
	Acknowledgements	104
	Declaration of Authorship	105

Abbreviations

Acronym	What (it) Stands For
AGN	Active Galactic Nuclei
BH	Black Hole
BLRG	Broad Line Radio Galaxy
CMB	Cosmic Microwave Background
DCF	Discrete Correlation Function
EHT	Event Horizon Telescope
FSRQ	Flat Spectrum Radio Quasar
FWHM	Full-Width Half Maximum
HBL	High-Peaked BL Lac Object
HPBW	Half Power Beam Width
IBL	Intermediate-Peaked BL Lac Object
ICF	Interpolated Correlation Function
LBL	Low-Peaked BL Lac Object
NLRG	Narrow Line Radio Galaxy
OVRO	Owens Valley Radio Observatory
QSO	Quasi-Stellar Object
RFI	Radio Frequency Interference
RG	Radio Galaxy
SED	Spectral Energy Distribution
SMA	Simple Moving Average
TELAMON	TeV Effelsberg Long-Term AGN Monitoring
VHE	Very-High Energy
VLBI	Very Long Baseline Interferometry
XBL	Extreme Blazar

Chapter 1

Introduction

Just about two years ago, almost every person on this planet was talking about one particular active galaxy with most of them not even knowing about it. This was back in April 2019, when the [Event Horizon Telescope Collaboration et al. \(2019\)](#) published the first ever image of a Black Hole (BH) shadow. From newspaper articles to TV shows and internet memes, this image was found all over the place. What most people probably aren't aware of is that the BH imaged by the Event Horizon Telescope (EHT) lies in the center of the active galaxy M87. Active galaxies and in particular active galactic nuclei (AGN) are amongst the most powerful and luminous objects in the Universe. The most luminous AGN, known as Quasars, have in common that their central engine is a supermassive BH which actively accretes matter through an optically thick accretion disk ([Shakura & Sunyaev, 1973](#); [Sun & Malkan, 1989](#)). The accelerated particles emit radiation through the entire electromagnetic spectrum from radio to γ -rays through various physical processes. A very interesting subclass of Quasars are Blazars, which exhibit a highly relativistic, collimated plasma stream (jet) pointed directly towards Earth. These jets can be powered by very strong magnetic fields close to the event horizon, extracting the rotational energy from the BH ([Blandford & Znajek, 1977](#)) or by the accretion flow ([Blandford & Payne, 1982](#)). The spectral energy distribution (SED) of Blazars typically shows a double-humped structure with one peak attributed to synchrotron emission, which peaks from the radio to the far-infrared and another peak in the high-energy regime ([Fossati et al., 1998](#)). The sources of interest for this thesis are High-Peaked BL Lac objects (HBL), which exhibit their synchrotron peak frequency above 10^{15} Hz. Some of them exhibit even higher synchrotron peaks, at least during major flares, and are therefore characterized as Extreme Blazars (XBL). What makes these sources particularly interesting is their bright high-energy emission in γ -rays and up to very-high-energy (VHE) in the TeV-range ([Biteau et al., 2020](#)). This VHE emission was found to be correlated with emission in the radio ([Lico et al., 2017](#)), therefore

these sources are main targets for Multiwavelength Astronomy from the radio to VHE. Additionally, the circumstances under which this emission is produced allows to investigate physics under extreme conditions, which is essential to study the formation and evolution of the Universe. This source class is also of high importance for astroparticle physics as potentially dominant source of ultra-high-energy cosmic-rays (Hillas, 1984) and high-energy neutrinos (Tavecchio et al., 2014; Padovani et al., 2015; Murase et al., 2018; Giommi et al., 2020). In this thesis, a brief overview of the AGN phenomenon will be given in Chap. 2. On top of that, the data of the first ~ 1.2 years of the TELAMON (Kadler et al., 2021) program are analyzed and presented. The TELAMON program is a radio monitoring program, designed to track the evolution of TeV-detected Blazars, especially HBLs and XBLs, with the Effelsberg 100-m telescope in order to understand the physical mechanisms behind these objects. The observations are carried out at high radio frequencies (19 GHz–44 GHz) on a cadence of two to four weeks. A sample of 18 XBLs and 12 HBLs is analyzed for flux density and spectral variability as well as possible radio flares. The data reduction steps of flux density measurements with the Effelberg 100-m telescope are described in detail in Chap. 3, results are presented in Chap. 4. Moreover, a comparison of the TELAMON results for HBL/XBL with previous studies of low-peaked BL Lacs and other Quasars by the F-GAMMA program (Fuhrmann et al., 2016; Angelakis et al., 2019) is presented in Chap. 5.

Chapter 2

Active Galactic Nuclei

If one tries to find AGN by solely looking through an optical telescope, there would be no way to tell them apart from stars from our own galaxy. Actually, it would be quite hard to even identify them, since they are quite faint objects in the optical sky. In the radio- and X-ray sky, things are very different. At these wavelengths, AGN are amongst the brightest emitters and show very complex features. These features have been discovered as early as the 1950s due to the gradual improvement of radio astronomy ([Matthews & Sandage, 1963](#)). Since their optical counterparts often look like stars, the sources were historically referred to as Quasi-Stellar-Objects (QSOs) or Quasi Stellar Radio Sources (Quasars) ([Chiu, 1964](#)). When comparing them to stars from our own galaxy in the optical, one finds a rather unusual spectrum with strong, broad emission lines, that, at first, could not be explained. This changed in 1963, when [Schmidt \(1963\)](#) identified the absorption lines of 3C 273 as radically redshifted ($z \approx 0.16$) Balmer lines. Shortly after, the same could be done for 3C 48, where a redshift of $z \approx 0.37$ was derived ([Greenstein, 1963](#)). This high redshift implies that the sources must be of extragalactic origin and the emission has to come from the nuclear region of a galaxy about 100 times more powerful than previously known radio galaxies. As of today, AGN are of extremely high interest due to their high luminosities produced in a very compact emission region. This emission cannot be explained by typical astronomical emission processes like nuclear fusion in stars, since it is much more powerful. The circumstances under which this emission is produced allows us to investigate physics under extreme conditions, which is essential to study the formation and evolution of the Universe. In this chapter, a brief overview of the AGN phenomenon and the radiative processes involved will be given. On top of that, the most luminous type of AGN, so-called Blazars, will be introduced in detail. The section is mainly based on [Urry & Padovani \(1995\)](#) and the Lecture on Multiwavelength Astronomy, given by Matthias Kadler at the University of Würzburg in the summer term of 2021.

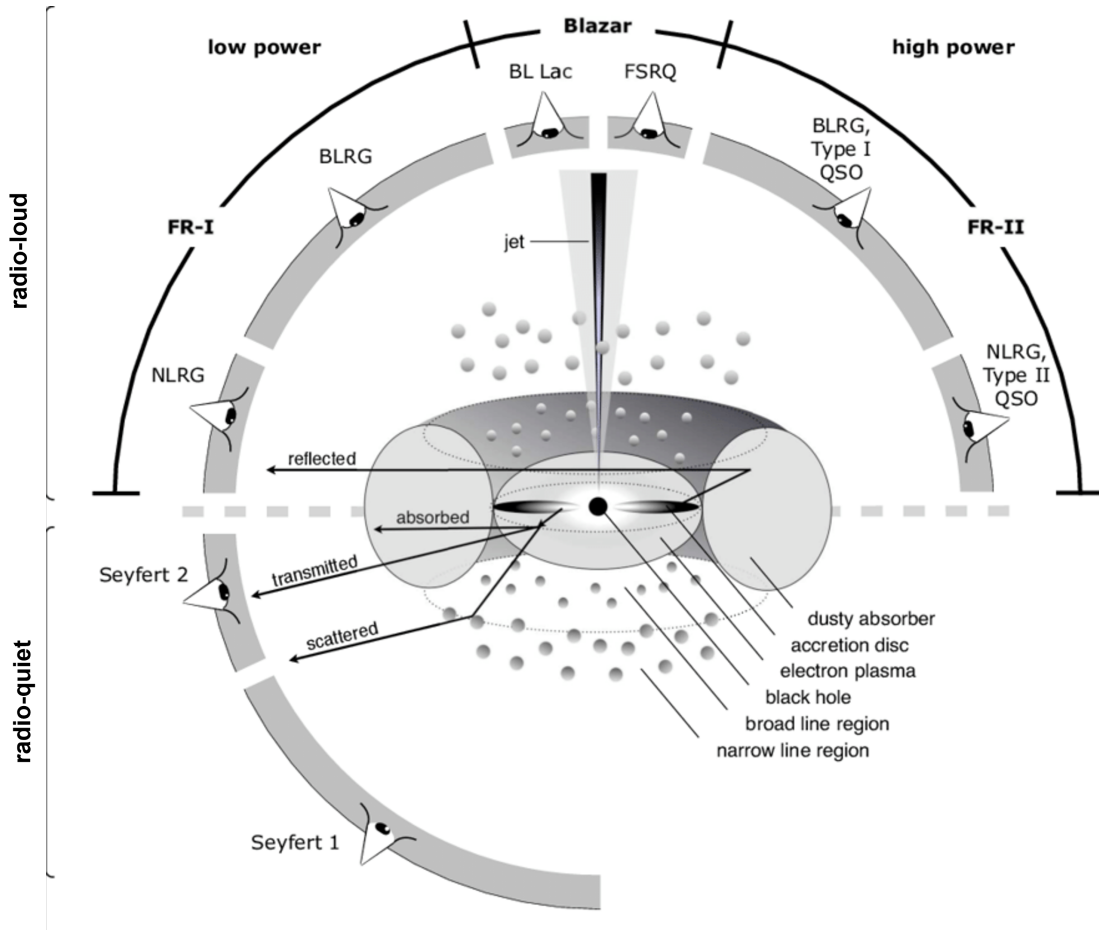


Fig. 2.1: Illustration of the current understanding of an AGN in the unified scheme. Depending on the viewing angle, the power of the central engine and whether the object is radio-loud or radio-quiet, different types of objects (e.g., FSRQ, Seyfert I&II etc.) are observed (adapted from [Beckmann & Shrader, 2012](#))

2.1 AGN Unification Model

The currently prevailing, unified model of AGN (e.g., [Urry & Padovani, 1995](#); [Antonucci, 1993](#)) is illustrated in Fig. 2.1. At the center of each AGN is a supermassive BH, which is also the central engine for the AGN luminosity. Due to its extreme gravitational potential, the BH accretes matter from the accretion disk. During the accretion process, this matter loses angular momentum in form of bright ultraviolet and soft X-ray radiation. Hard X-ray emission is most likely emitted from the hot electron plasma above and below the accretion disk. In the so-called “broad line region” clouds of gas produce strong optical and ultraviolet emission lines. This entire central region is usually framed by a large dust torus, which blocks the view to the central region for more edge-on viewing angles. Beyond the torus, there is another gaseous region, called the “narrow line region”, where slower moving gas produces narrower emission lines as compared to the broad line region. As indicated in Fig. 2.1, one can distinguish between radio-loud

Table 2.1: Classification of AGN depending on the viewing angle, the power of the central engine and whether they are radio-loud or radio-quiet. (Adapted from: Matthias Kadler, Lecture on Multiwavelength Astronomy, SS 2021, University of Wuerzburg)

Type	Radio Loudness	Emission Lines	Luminosity	Radio Morphology
Seyfert I	radio-quiet	B+N	Low	-
Seyfert II	radio-quiet	N	Low	-
QSO (Type I)	radio-quiet	B+N	High	-
QSO (Type II)	radio-quiet	N	High	-
BLRG	radio-loud	B+N	Low	FR 1
	radio-loud	B+N	High	FR 2
NLRG	radio-loud	N	Low	FR 1
	radio-loud	N	High	FR 2
BL Lac	radio-loud	-	Low	Compact
FSRQ	radio-loud	B+N	High	Compact

and radio-quiet AGN. This is usually done by analyzing the ratio of radio and optical flux of the source (Kellermann et al., 1989), defined as

$$R_{r-o} = \frac{F(6 \text{ GHz})}{F(4400 \text{ \AA})}. \quad (2.1)$$

A source is called radio-loud if $10 < R_{r-o} < 1000$ and radio-quiet if $0.1 < R_{r-o} < 1$. Typical for radio-loud AGN are their highly collimated, relativistic, radio-emitting jets. The origin of these jets is still not clear, but in current models, these jets are produced by outflows of energetic particles along the poles of the central region due to extreme magnetic fields (for a review, see Blandford et al., 2019). The jet plasma is ejected at highly relativistic velocities which leads to relativistic beaming effects further described in Sect. 2.3.2. Due to their high ejection velocities, the length of the jets can reach several thousands and up to millions of light years.

2.2 Classification of AGN - The AGN Zoo

A first classification of AGN, into radio-loud and radio-quiet, has already been introduced by Equation (2.1). Initially, the unification scheme introduced in Sect. 2.1 emerged from observations of - on the first impression - very different objects, that will briefly be presented in this section. At the current state of the art, it is believed that all these objects are AGN according to the model presented in Fig. 2.1. The only difference is the viewing angle, the power of the central engine and whether the object is radio-loud or radio-quiet. An overview about these objects and their classification is given in Table 2.1. Let us first discuss radio-quiet AGN very briefly. Here, one finds Seyfert I & II galaxies, as well as Type I & II Quasi Stellar Objects (QSO). All of these objects have in common that one finds (optical) spectral emission lines when observing them. Type I

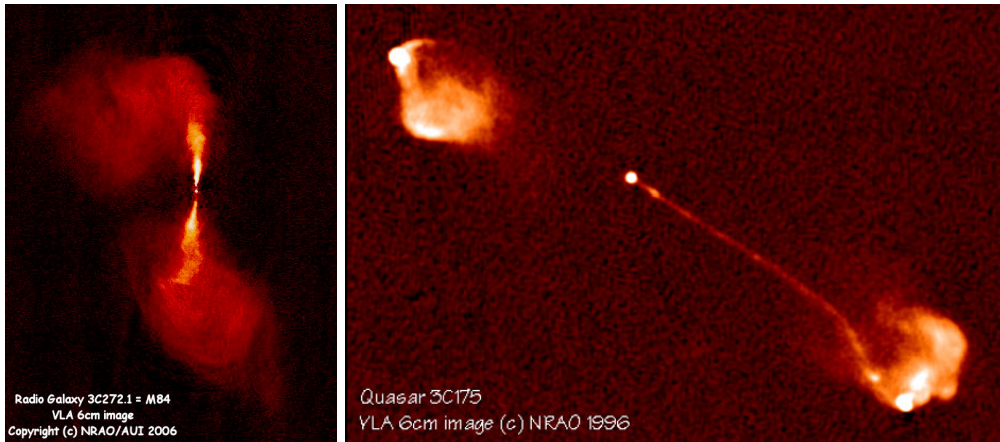


Fig. 2.2: VLA images of the Fanaroff-Riley Type 1 galaxy M84 (left) and the Fanaroff-Riley Type 2 galaxy 3C175 (right). M84 is clearly characterized by the FR1-typical broad and asymmetric jets and a bright core, while the FR2 galaxy 3C175 exhibits dominant radio-lobes at the end of the (one-sided) jet.

always refers to visible broad and narrow emission lines, Type II sources exhibit only narrow emission lines. As mentioned before, one can associate two different emission regions with broad line and narrow line emission in the AGN standard model. This implies that somehow the broad line emission is absorbed for Type II sources (Seyfert II and QSO Type II). Indeed, in the standard model, this is explained by the fact that Type II sources are all observed almost edge-on. As indicated in Fig. 2.1, the light from the central region (where the broad line region is located) is partly absorbed by the dust torus and therefore not observable for edge-on observers. The narrow line region is located beyond the dust torus, and therefore observable from almost any viewing angle. This is different for Type I sources, where one observes narrow line and broad line emission. This effect is simply due to the observing angle, since Type I sources are observed more face-on, one receives radiation from the narrow and broad line region, resulting in the typical Type I spectrum. The classification of radio quiet sources into Seyfert Galaxies and QSOs is mainly due to historical reasons and somewhat arbitrary. Seyfert Galaxies are named after Karl Seyfert, who was among the first to detect their nuclear emission lines (Seyfert, 1943). Sources that are brighter than some magnitude are defined as QSOs, sources that are fainter are considered Seyfert Galaxies.

Only about 15%-20% of AGN are radio-loud (Kellermann et al., 1989), as defined in Equation (2.1). Usually, their non-radio spectra are very similar to radio-quiet AGN and must therefore be produced by similar physical processes. Similar to radio-faint sources, radio-loud AGN are also classified according to their visible (optical) emission lines. Let us first consider Broad Line Radio Galaxies (BLRG) and Narrow Line Radio Galaxies (NLRG), which can be understood as the radio-loud analogues to radio-quiet Type I & II explained above. When a radio-loud AGN is observed almost edge-on, the

broad line emission is absorbed by the dust torus and therefore only narrow emission lines are visible (NLRG). If the AGN is observed at a more face-on angle, one observes broad and narrow emission lines (BLRG). On top of the spectral line classification, radio-loud objects are further classified according to their radio-jet morphology. Early work in the radio-classification of AGN has been done by Fanaroff & Riley (1974). One distinguishes between Fanaroff-Riley Type 1 (FR1) and Fanaroff-Riley Type 2 (FR2) objects. The main difference of these types is of observational nature and can be seen in Fig. 2.2. FR1 galaxies are often low-luminosity sources and usually exhibit symmetric radio jets whose intensity declines with increasing distance from a bright nucleus. A typical FR1 galaxy, M84, can be seen on the left in Fig. 2.2. The characteristic features of FR2 galaxies are highly collimated, often one-sided jets, leading to well-defined lobes with prominent hot spots. A typical FR2 galaxy, 3C175, can be seen on the right in Fig. 2.2. In addition to that, there is another source class that does not fit the FR1/2 classification scheme, called Blazars. These radio-loud AGN are observed almost exactly face-on, which means that the observer looks more or less straight into the radio jet. Typically, these objects show very fast, large amplitude variability and unresolved nuclear emission lines (on arcsec scales). Blazars are further divided into two subclasses. On the one hand, there are BL Lac objects which are characterized by the absence of emission lines (except during low-states). On the other hand, there are Flat Spectrum Radio Quasars (FSRQs) which are in general more luminous than BL Lac sources and exhibit typical broad and narrow emission lines. Blazars are of particular interest in Multiwavelength Astronomy since a large fraction of their emission is at high energies (hard X-ray, γ -ray and up to VHE). Note that all of the objects presented in Table 2.1 have been discovered as individual source classes. Due to their very similar features (e.g., emission lines), they can all be explained by the AGN unification model presented in Sect. 2.1, depending on their viewing angle, the power of the central engine and their radio-loudness. In the following sections, the typical AGN spectrum with focus on the subclass of Blazars will be introduced. Moreover, the radiative processes that generate their emission will be presented.

2.3 Radiative Processes in AGN

Apart from the emission lines, which are produced by nuclear transitions in gas clouds, the broad band spectra of AGN can all be modelled with a power law fit. From a phenomenological point of view, the observed flux density F_ν can always be described by

$$F_\nu \propto \nu^\alpha, \quad (2.2)$$

where ν refers to the observing frequency and the energy index $\alpha \approx -1$. This implies that νF_ν is constant, usually referred to as a flat νF_ν -spectrum. Just from an observational perspective, one can therefore conclude that the radiative processes in AGN must be of non-thermal nature, since this kind of spectrum cannot be explained by thermal emission. In this section, the most important radiative processes that contribute significantly to the spectral energy distribution of AGN are presented, namely synchrotron radiation and inverse Compton scattering. Note that this is only a brief overview of the physical mechanisms, for details it is referred to [Rybicki & Lightman \(1979\)](#), on which this section is also mainly based. Another important reference for this chapter is the lecture on Multiwavelength Astronomy, given by Matthias Kadler at the University of Würzburg in the summer term of 2021.

2.3.1 Synchrotron Radiation

First, let us consider the relativistic motion of a charged particle of mass m and charge q in a magnetic field \vec{B} :

$$\frac{d}{dt}(\gamma m \vec{v}) = \frac{q}{c} \vec{v} \times \vec{B}, \quad (2.3)$$

$$\frac{d}{dt}(\gamma m c^2) = q \vec{v} \cdot \vec{E} = 0, \quad (2.4)$$

where $\gamma = \frac{1}{\sqrt{1-\beta}}$ is the Lorentz factor with $\beta = v/c$. From Equation (2.4) it follows that $\gamma = \text{const.}$, i.e., $v = \text{const.}$, which can be used to simplify Equation (2.3):

$$m\gamma \frac{d\vec{v}}{dt} = \frac{q}{c} \vec{v} \times \vec{B}. \quad (2.5)$$

After separating the velocity \vec{v} into components along the magnetic field \vec{v}_\parallel and in a plane perpendicular to the field \vec{v}_\perp one finds

$$\frac{d\vec{v}_\parallel}{dt} = 0, \quad (2.6)$$

$$\frac{d\vec{v}_\perp}{dt} = \frac{q}{\gamma m c} \vec{v}_\perp \times \vec{B}. \quad (2.7)$$

This implies $\vec{v}_\parallel = \text{const.}$ and also $|\vec{v}_\perp| = \text{const.}$, since it has been established earlier that v needs to be constant. This leaves Equation (2.7) remaining, the differential equation for uniform circular motion. The combination of uniform motion parallel to the magnetic field ($\vec{v}_\parallel = \text{const.}$) and uniform circular motion perpendicular to the field results in a total helical motion of the particle. The rotational frequency is given by

$$\omega_B = \frac{qB}{\gamma m c} = \frac{\omega_L}{\gamma}, \quad (2.8)$$

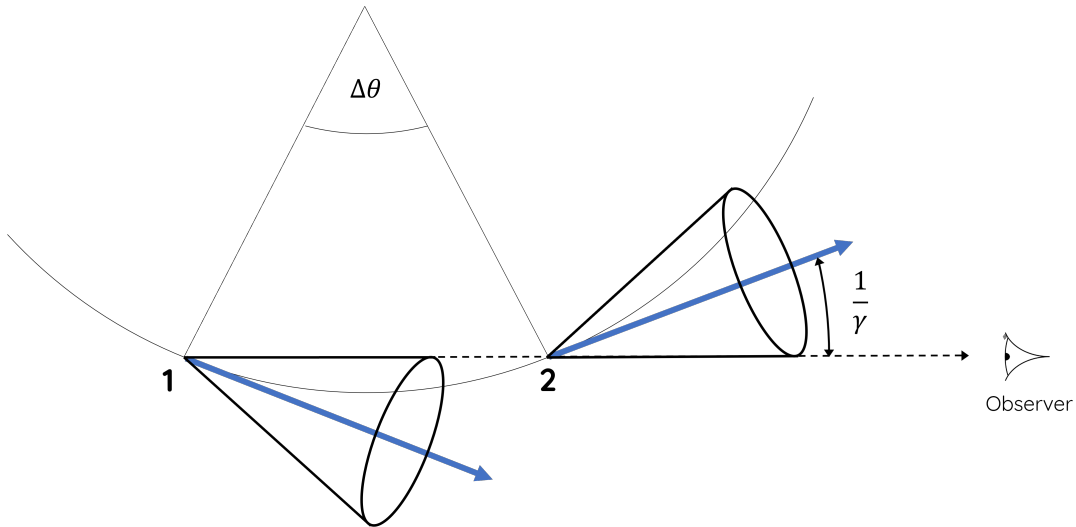


Fig. 2.3: Illustration of synchrotron emission by relativistic electrons with circular motion. Because of beaming effects, the emitted radiation fields are concentrated in a narrow region (cone) pointing in the same direction as the particle's velocity (adapted from [Rybicki & Lightman, 1979](#)).

where the definition of the Larmor frequency $\omega_L = qB/mc$ has been used. Accelerated charged particles emit synchrotron radiation, defined by Larmor's formula:

$$P = \frac{dW}{dt} = \frac{q^2 v^2}{4\pi c^3} \int \sin^2 \theta d\Omega = \frac{2q^2 v^2}{3c^3}. \quad (2.9)$$

If this is averaged over an isotropic distribution of velocities and particles are assumed to be relativistic electrons ($\beta \approx 1, q = e$), one finds for the average emitted power $\langle P \rangle$ of one electron

$$\langle P \rangle = \frac{4}{3} \sigma_T c \beta^2 \gamma^2 U_B, \quad (2.10)$$

where $\sigma_T = 8\pi e^2/3m_e^2 c^4$ is the Thomson cross section and U_B the magnetic energy density $U_B = B^2/8\pi$. Other (heavier) particles like, e.g., protons only contribute marginally to the emitted power, since $\langle P \rangle \propto m^{-2}$.

The synchrotron emission process of a relativistic electron with circular motion is illustrated in Fig. 2.3. Due to relativistic beaming, and the fact that acceleration and velocity of the particles are perpendicular to each other, the radiation is emitted in a concentrated, cone-like shape with opening angle $\Delta\theta \approx 1/\gamma$. In order to get an understanding of the relativistic effects that come into play here, let us first look at the frame of rest of the electron. From this point of view, the beam passes the observer in a time interval

$$\Delta t_e = \frac{\Delta\theta}{\omega_B} = \frac{m_e c \gamma}{e B} \frac{2}{\gamma} = \frac{2}{\omega_L}. \quad (2.11)$$

From the point of view of the observer, things are different. Since the electron moves at relativistic speeds towards the observer, the synchrotron emission gets Doppler-shifted.

Since the electron is closer to the observer at point 2 than at point 1, the (Doppler-shifted) pulse duration in the observer frame is given by

$$\Delta t_o = \left(1 - \frac{v}{c}\right) \Delta t_e = (1 - \beta) \Delta t_e. \quad (2.12)$$

With the intermediate step

$$\frac{1}{\gamma^2} = 1 - \frac{v^2}{c^2} = (1 + \beta)(1 - \beta) \approx 2(1 - \beta), \quad (2.13)$$

which is valid for $\gamma \gg 1$, i.e., $\beta \approx 1$, Equation (2.12) can be rewritten as

$$\Delta t_o = (1 - \beta) \Delta t_e = \frac{2(1 - \beta)}{\omega_L} = \frac{1}{\gamma^2 \omega_L}. \quad (2.14)$$

This expression yields information about the characteristic frequency ω_c of the synchrotron emission

$$\omega_c = \frac{1}{\Delta t_o} = \gamma^2 \omega_L = 280 \left(\frac{\gamma}{100}\right)^2 \left(\frac{B}{1\mu\text{G}}\right) \text{MHz}, \quad (2.15)$$

where numerical values for the Larmor Frequency ω_L have been inserted. One can see that with typical values of $B \approx 1 \text{ G} = 10^{-4} \text{ T}$ and $\gamma \gg 1$ close to the centers of AGN, the radio emission in the GHz regime can be well explained by this emission process.

On top of that, one can actually model the entire synchrotron spectrum P_ν for a given electron distribution $n(\gamma)$. In order to do this, one needs to sum over the different contributions from electrons with different energies:

$$P_\nu = \int_1^\infty \langle P_\nu(\gamma) \rangle n(\gamma) d\gamma. \quad (2.16)$$

For non-thermal synchrotron radiation, the electron energies are assumed to be distributed according to a power law

$$n(\gamma) d\gamma = n_0 \gamma^{-p} d\gamma, \quad (2.17)$$

with some constants n_0 and p . In order to find an expression for the spectral energy distribution $P_\nu(\gamma)$, the expression found in Equation (2.10) is used and a function $\phi_\nu(\gamma)$ inserted, which accounts for the spectral shape:

$$\langle P_\nu(\gamma) \rangle = \langle P(\gamma) \rangle \phi_\nu(\gamma) = \frac{4}{3} \sigma_{\text{TC}} c \beta^2 \gamma^2 U_B \phi_\nu(\gamma). \quad (2.18)$$

It is important to note that $\phi_\nu(\gamma)$ is constrained by

$$\int \phi_\nu(\gamma) d\nu = 1, \quad (2.19)$$

since Equation (2.10) still needs to hold. Further, it is assumed that synchrotron emission is only produced at the characteristic frequency $\nu_c = \omega_c/2\pi = \gamma^2\nu_L$. This is justified since the synchrotron spectrum has a significant and narrow peak at this frequency. Speaking in terms of the spectral shape, this means

$$\phi_\nu(\gamma) = \delta(\nu - \gamma^2\nu_L), \quad (2.20)$$

where ν_L is the Larmor frequency. If now, Equations (2.17), (2.18) and (2.20) are plugged into Equation (2.16), one finds

$$P_\nu = \int_1^\infty \frac{4}{3} \sigma_T c \beta^2 \gamma^2 U_B \delta(\nu - \gamma^2\nu_L) n_0 \gamma^{-p} d\gamma. \quad (2.21)$$

It has already been assumed that $\gamma \gg 1$, which implies $\beta \approx 1$. Therefore, one finds

$$P_\nu = C \int_1^\infty \gamma^{2-p} \delta(\nu - \gamma^2\nu_L) d\gamma, \quad (2.22)$$

with a well defined constant C. Substituting $\nu' = \gamma^2\nu_L$ leads to

$$P_\nu = C^* \int_{\nu_L}^\infty \gamma^{1-p} \delta(\nu - \nu') d\nu', \quad (2.23)$$

with some other constant C^* . According to the substitution $\gamma = \sqrt{\nu'/\nu_L}$, therefore one finds

$$P_\nu = C^* \int_{\nu_L}^\infty \left(\frac{\nu'}{\nu_L}\right)^{\frac{1-p}{2}} \delta(\nu - \nu') d\nu' = C^* \cdot \left(\frac{\nu}{\nu_L}\right)^{-\frac{p-1}{2}}. \quad (2.24)$$

The constant is given by $C^* = \frac{2}{3} c \sigma_T n_0 U_B / \nu_L$. Finally, following from Equation (2.24), one can conclude that for the assumption of a power law electron energy distribution $n(\gamma)$, the emitted spectrum P_ν is also a power law. The emitted spectrum is usually characterized by the so-called spectral index α defined as $\alpha = -\frac{p-1}{2}$. This also means that spectral observations can be used to model physical processes close to the center region of AGN and to derive intrinsic source properties, e.g., the electron distribution. Note that the presented calculations include a lot of approximations, since a detailed calculation would go beyond the scope of this work. The same calculation can also be carried out completely analytically, without any approximations. The reader is encouraged to look at [Rybicki & Lightman \(1979\)](#) for further details.

Another important thing to mention is that the spectrum, as calculated in Equation (2.24), is only valid in regions where the electrons do not interact with the produced

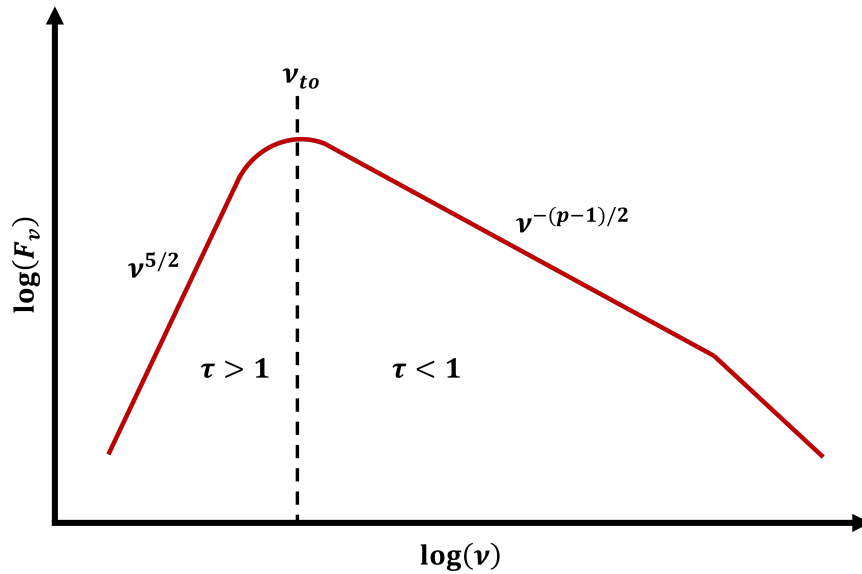


Fig. 2.4: Sketch of a typical synchrotron emission spectrum, with turnover frequency ν_{to} and optically thick ($\tau > 1$) and thin ($\tau < 1$) region (adapted from [Shu, 1991](#))

synchrotron radiation photons. In order to further discuss this, let us first introduce the optical depth

$$\tau_\nu(s) = \int_{s_0}^s \alpha_\nu(s') ds', \quad (2.25)$$

where α_ν is the absorption coefficient and s the travelled distance of a photon. If $\tau_\nu < 1$, a medium is considered optically-thin (transparent) and Equation (2.24) is valid. In AGN there is usually a turnoff at a specific frequency ν_{to} where $\tau_\nu = 1$. For frequencies $\nu > \nu_{to}$, the medium is optically thin ($\tau_\nu < 1$) but for frequencies $\nu < \nu_{to}$, the electrons start to absorb the synchrotron radiation photons in the optically thick (opaque, $\tau > 1$) medium. This process is called Synchrotron-Self-Absorption and affects the spectrum significantly. For frequencies $\nu < \nu_{to}$ the spectrum can be described by a power law with spectral index 5/2, i.e.,

$$P_\nu \propto \nu^{5/2}. \quad (2.26)$$

An exemplary spectrum is plotted in Fig. 2.4, where one can clearly identify the turnover frequency ν_{to} , where $\tau = 1$ and the spectral index changes. Note that at the highest frequencies in Fig. 2.4 the spectrum also steepens. This is due to the highest-energy electrons that radiate away their energy the fastest. The turnoff frequency is highly dependent on the size of the emitting region. Since radio jets usually consist of multiple components of different sizes (usually increasing with distance from the core), the actual spectrum is a superposition of many spectra like the one shown in Fig. 2.4, with different turnoff frequencies. When superposing these spectra with different turnoff frequencies one finds the typical flat radio spectrum of AGN. This is illustrated in Fig. 2.5, where one can see that at lower frequencies, the spectrum mainly consists of a typical synchrotron

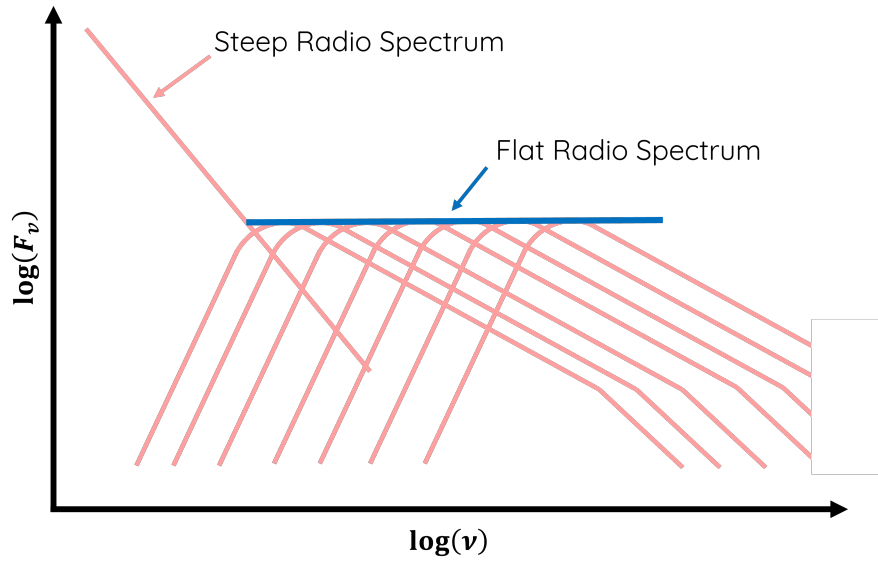


Fig. 2.5: Sketch of the typical flat radio spectrum of AGN, composed by a superposition of multiple jet components. The steep radio spectrum from synchrotron emission of large kpc-scale regions, while the flat spectrum can be attributed to a superposition of multiple pc-scale jet components closer to the core.

spectrum from larger kpc-scale regions, while the higher radio frequencies are dominated by a flat spectrum originating from the superposition of multiple pc-scale jet components. This also means that at different frequencies, different parts of the jets are observed. Observations at high frequencies are usually attributed to more compact regions close to the core, while observations at lower frequencies can be attributed to larger regions more distant from the core.

2.3.2 Relativistic Beaming

On top of the relativistic synchrotron radiation, there are other relativistic effects that influence the radio spectrum of AGN, and in particular Blazars. In this section, the effect of relativistic beaming, which explains why Blazars belong to the brightest sources in the radio-sky, will be explained. To discuss this in detail, let us first introduce the relativistic Doppler factor \mathcal{D} , which describes how emitted radiation with frequency ν_{em} is Doppler-shifted to an observing frequency ν_{obs} :

$$\mathcal{D} = \frac{\nu_{\text{obs}}}{\nu_{\text{em}}} = \frac{1}{\gamma \left(1 - \frac{v}{c} \cos \theta\right)} = \frac{\sqrt{1 - \beta^2}}{1 - \beta \cos \theta}. \quad (2.27)$$

Here, θ is the aspect angle between the line of sight and the velocity component. In [Rybicki & Lightman \(1979\)](#), it is shown that F_ν/ν^3 is invariant under Lorentz transformation. For the observed intensity $I(\nu)$, this means

$$\frac{I(\nu_{\text{obs}})}{\nu_{\text{obs}}^3} = \frac{I(\nu_{\text{em}})}{\nu_{\text{em}}^3}, \quad (2.28)$$

which is equivalent to

$$I(\nu_{\text{obs}}) = \nu_{\text{obs}}^3 \frac{I(\nu_{\text{em}})}{\nu_{\text{em}}^3} = \mathcal{D}^3 I(\nu_{\text{em}}). \quad (2.29)$$

If now a power law spectrum $I(\nu_{\text{em}}) = A \nu_{\text{em}}^\alpha$ is considered, as discussed in Sect. 2.3.1, the observed intensity becomes

$$I(\nu_{\text{obs}}) = \mathcal{D}^3 A \nu_{\text{em}}^\alpha = \mathcal{D}^3 A \mathcal{D}^{-\alpha} \nu_{\text{obs}}^\alpha = \mathcal{D}^{3-\alpha} I(\nu_{\text{em}}). \quad (2.30)$$

The Doppler factor therefore has a big influence on how bright an AGN is observed. Since the jet plasma is usually moving at high relativistic speeds ($\beta \rightarrow 1$), Doppler factors can reach the order of $\sim 10^3$, especially in Blazars, where the aspect angle θ is very small. The synchrotron flux can therefore be boosted by a factor of up to ~ 1000 in the forward direction, while in the backward direction it is reduced by the same factor. But even for mildly relativistic speeds and larger aspect angles, this effect is observable and explains why one usually observes only one-sided jets in FR2-type galaxies (see Fig. 2.2, right). The jet pointing towards the observer is forward boosted and the counter-jet is reduced, since it is moving away from the observer at relativistic speeds. The flux-density ratio of jet (F_1) and counter-jet (F_2) can in general be expressed as

$$\frac{F_1}{F_2} = \left(\frac{1 + \beta \cos \theta}{1 - \beta \cos \theta} \right)^{2-\alpha}. \quad (2.31)$$

Note that the superscript here is $(2 - \alpha)$ instead of $(3 - \alpha)$, since jets usually consist of multiple components and the number of components also scales with the Doppler factor.

2.3.3 High-Energy Emission

While the low-frequency emission of AGN can be well explained by non-thermal synchrotron emission of relativistic electrons, as introduced in Sect. 2.3.1, the source of high-energy emission from AGN is still under debate. Blazars are by far the brightest high-energy emitters among AGN, as they exhibit emission from X-rays to γ -rays and even TeV-energies. However, it is still not clear what mechanisms produce this radiation. In principle, there are two models, which both can explain the high-energy spectrum of AGN. On the one hand, there are leptonic models (e.g., [Blandford & Königl, 1979](#))

and on the other hand, there are hadronic models (e.g., Mannheim, 1993). For leptonic models, the most important process is inverse Compton scattering where relativistic electrons (also responsible for the synchrotron emission) interact with seed photons and boost them to higher energies. In so-called Self-Synchrotron-Compton models (SSC, e.g., Tavecchio et al., 1998) the seed photons originate from the synchrotron radiation produced by the relativistic electrons themselves. Another possible origin of seed photons for the inverse Compton process can be external, e.g., from the accretion disk. This model is called External-Compton model (EC, e.g., Sikora et al., 1994). In hadronic models, high-energy photons are produced by hadronic collisions and decay (e.g., pion decay). These Models are of particular interest because they can explain the possible neutrino emission of AGN (e.g., Kadler et al., 2016; IceCube Collaboration et al., 2018). In order to examine the possible scenarios and to distinguish between different models it is very important to perform long term multi-wavelength studies of the SED of AGN from radio to TeV-energies.

2.4 Blazars

Blazars, the most luminous and variable type of AGN, have already been introduced above. In this section, this AGN class will be presented in more detail, since it is of very high interest for astroparticle physics as possibly dominant neutrino and ultra-high-energy (UHE) cosmic ray emitters.

2.4.1 The Blazar Sequence

The Blazar SED usually exhibits a double-humped structure, as can be seen in Fig. 2.6. The first (low-energy) hump is attributed to non-thermal synchrotron emission, while the second (high-energy) hump has different explanations as described in Sect. 2.3.3. Additionally, in Fig. 2.6, one can see five averaged Blazar SEDs, each representative for a larger sample, that seem to describe a particular pattern, the so-called Blazar Sequence. Fossati et al. (1998) and Donato et al. (2001) found that the SED of more luminous Blazars peaks at lower frequencies as compared to low-luminosity Blazars, which seem to peak at higher frequencies. It is therefore useful to classify Blazars according to their synchrotron peak frequency ν_{peak} . This classification has been introduced by Padovani & Giommi (1995) and divides the class of Blazars into high-peaked (HBL, $\nu_{\text{peak}} > 10^{15}$ Hz), intermediate-peaked (IBL, 10^{14} Hz $< \nu_{\text{peak}} < 10^{15}$ Hz) and low-peaked (LBL, $\nu_{\text{peak}} < 10^{14}$ Hz). In extreme cases, for the so-called Extreme Blazars (XBL), the peaks can be shifted upwards up to two orders of magnitude (e.g., Biteau et al., 2020; Ghisellini, 1999). In general, one can say that Blazars emitting at γ - and TeV-energies are very

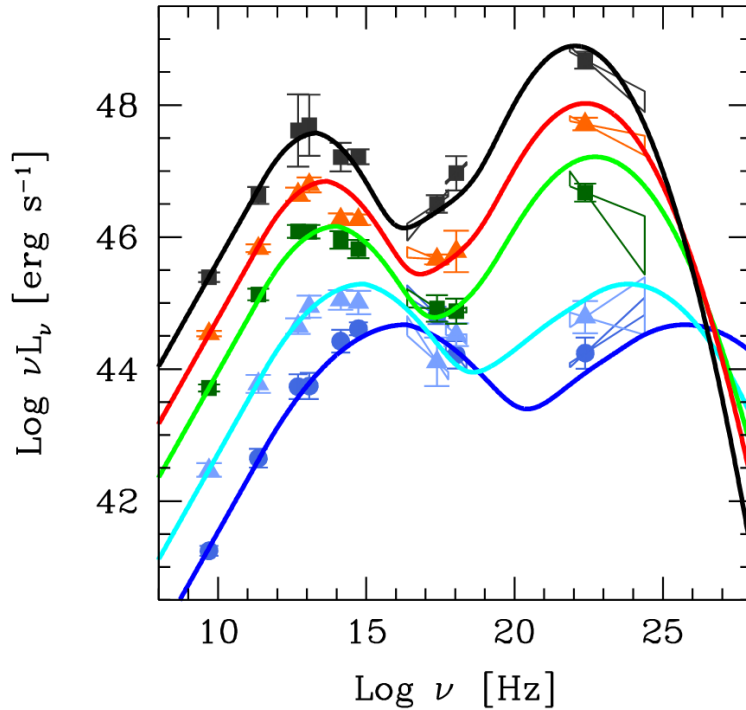


Fig. 2.6: The Blazar Sequence: Average SEDs of multiple Blazars categorized according to their radio luminosity. The plot reveals that sources with lower luminosities tend to have their (synchrotron-)peak at higher frequencies (adapted from Fossati et al., 1998)

faint in the radio and therefore difficult to observe. Due to their luminous high-energy emission, they are possible sources of cosmic-rays and neutrinos which makes them one of the prime targets for Multiwavelength Astronomy. Note that the Blazar Sequence as formulated by Fossati et al. (1998) is currently under discussion, since it is based on EGRET high-energy data which mostly consist of Blazars observed during a flaring state. This observational bias can be reduced by including data of the newer FERMI-LAT mission (e.g., Abdo et al., 2010), for details it is referred to Keenan et al. (2021). The prediction that the class of TeV-emitting Blazars is dominated by HBL objects still holds true. Out of all the 79 TeV-detected Blazars, 55 are HBLs, 9 are IBL and only 2 are LBL.¹

2.4.2 Extreme Blazars

As introduced earlier, Blazars are categorized according to their synchrotron emission peak frequency into LBLs, IBLs, HBLs and XBLs. In this section, the class of XBLs will be introduced in detail, mainly based on Biteau et al. (2020). The definition according to the synchrotron peak frequency is only half of the story for XBLs, since they are

¹<http://tevcat2.uchicago.edu/>

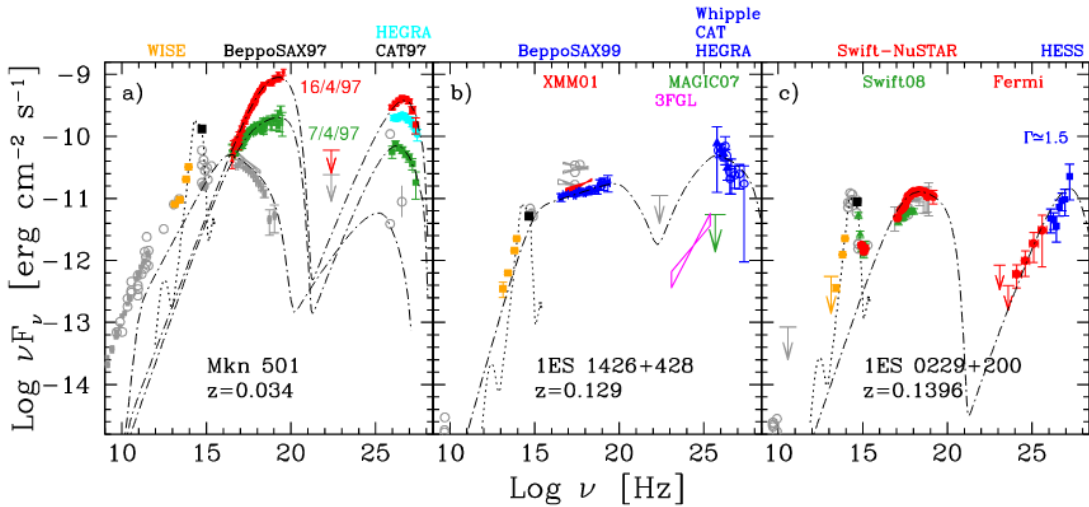


Fig. 2.7: Exemplary SED evolution of the three different types of extreme behaviour in Blazars. There are sources which exhibit extreme behaviour only in flaring episodes (a), sources with a persistently high synchrotron peak but no persistent TeV emission (b) and persistent TeV emitters with synchrotron peaks typically in the X-ray band (c) (adapted from Biteau et al., 2020)

divided into two different sub-classes, the extreme-synchrotron sources and the extreme-TeV sources. Extreme-synchrotron sources are defined via their synchrotron peak energy $h\nu_{\text{peak}} > 1 \text{ keV}$ ($\approx 10^{17} \text{ Hz}$), while extreme-TeV sources are defined via their γ -ray peak energy $h\nu_{\text{peak}} > 1 \text{ TeV}$ ($\approx 10^{26} \text{ Hz}$). Both classes are considered Extreme Blazars. To date, there are 24 Extreme Blazars known with redshift and published TeV spectrum. All of these sources are also detected at GeV-energies by Fermi-LAT (Abdollahi et al., 2020). 23 of these sources are extreme-synchrotron emitters, while 13 of them are also extreme-TeV sources. Only one source is known to be an extreme-TeV source but not an extreme-synchrotron source. As depicted in Fig. 2.7, the SED evolution of Extreme Blazars tends to be divided into three different behaviours. There are sources which become extreme during flaring episodes, i.e., both peaks (synchrotron- and high-energy-peak) shift to higher energies. During their low states, they exhibit regular HBL properties. An example of this behaviour is Mrk 501, as illustrated on the left of Fig. 2.7. This source is also one of the first blazars, whose extreme behaviour was identified in the late 1990s (Pian et al., 1998). Secondly, there are sources which exhibit a continuously hard synchrotron spectrum, but no persistent TeV emission. An example of this can be seen in the center of Fig. 2.7 with the source 1ES 1426+428. Lastly, there are sources which show a continuously hard γ -ray spectrum (peaking above several TeV). Their synchrotron peak is usually located in the X-ray band. An example of this behaviour is the source 1ES 0229+200, depicted on the right of Fig. 2.7. This source is also of particular interest because it has the highest γ -ray peak energy ($\geq 10 \text{ TeV}$) of any Extreme Blazar known to date (Aharonian et al., 2007). In general, all XBLs are very faint in the radio regime,

since their emission peaks are shifted to higher energies. This makes it challenging to observe these sources at typical GHz radio frequencies and requires telescopes with a very high sensitivity, e.g., the Effelsberg 100-m telescope.

2.4.3 Doppler Crisis

Another characteristic feature of TeV-emitting blazars is that almost all of them are affected by the Doppler Crisis. Usually, the highly variable TeV-emission of blazars is explained by involving very high Doppler factors up to $\mathcal{D} > 40$ (e.g., [Tavecchio et al., 2010](#)). In contrast to this, radio observations have found that HBL jets typically move at comparatively low speeds, indicative of low Doppler factors. This apparent paradox has become known as the “bulk Lorentz-factor crisis” or “Doppler crisis” ([Henri & Saugé, 2006](#)). One possible explanation is that the radio emission and the variable γ -ray emission may not originate from the same emitting region. [Ghisellini et al. \(2005\)](#) suggest that this could be realized in form of a “spine-sheath” structure where the outer layers of the relativistic jet (sheath) have slower bulk velocity along the jet axis than the inner layers (spine) and can serve as a seed-photon field for inverse-Compton processes within the spine. In principle, VLBI observations can reveal such spine-sheath structures (e.g., [Giroletti et al., 2004, 2008](#)), creating a possibly very important connection between radio and TeV emission. However, this connection is still unclear, since most VLBI observations of TeV blazars were made at comparably low frequencies and during low radio states ([Piner & Edwards, 2018](#), and references therein). Further coordinated radio and high-energy observations of these sources, especially during high-states, possibly triggered by the TELAMON program (see Sect. 3.3), are therefore required to investigate the Doppler Crisis and proposed models.

2.4.4 Neutrino-Blazar Associations

At the end of this introductory chapter, some interesting Blazars that have been associated with possible neutrino emission will be introduced, which underlines the relevance of this source type for the astronomical community. Especially HBLs and XBLs are prime candidates for possible neutrino emission, due to their strong VHE-emission. Let us first introduce the Blazar PKS 1424-418, which has been associated with the ~ 2 PeV IceCube Neutrino event IC 35 (“Big Bird”) by [Kadler et al. \(2016\)](#) at 2σ significance. The source exhibited a bright γ -ray outburst shortly after the neutrino detection and a coincident increase of VLBI core flux density was detected. Another interesting Blazar is TXS 0506+056. This source has been associated with the IceCube-170922A Event in 2017 ([IceCube Collaboration et al., 2018](#)). During the time of neutrino-detection the

source was in a flaring state of high γ -ray emission, which makes it a likely source of the detected neutrino. A multiwavelength campaign by [Padovani et al. \(2018\)](#) was triggered shortly after the alert, which found that TXS 0506+056 is the only counterpart of all the neutrino emission in the event region and therefore the most plausible, first non-stellar neutrino and, hence, cosmic ray source. However, there is still no 3σ neutrino-Blazar association, which would be required for the association to be widely accepted. There is more and more evidence piling up that Blazars are one of the main neutrino sources in the sky. PKS 1502+106, e.g., was identified as another possible neutrino source by [Rodrigues et al. \(2021\)](#). On top of that, independent studies by [Plavin et al. \(2020, 2021\)](#) and [Hovatta et al. \(2021\)](#) show that radio flares in Blazars are very likely correlated with neutrino emission. In order to pin down Blazars as neutrino emitters, one needs to build up a statistical database of multiple neutrino-blazar associations, therefore more (multiwavelength-)data is required to finally resolve this important question. This can be realized, e.g., by performing follow-up observations of IceCube Bronze/Gold neutrino track alerts ([Blaufuss et al., 2019](#)) at different wavelengths.

Chapter 3

Observations & Data Reduction

The first astronomical radio waves were detected by Karl G. Jansky in 1932 using an antenna built to study radio receiver noise (Jansky, 1933). What Jansky initially identified as a hiss noise signal turned out to be radiation from the center of the Milky Way Galaxy. This observation has laid the foundation for an entirely new field, called Radio Astronomy. As radio waves are able to pass through most kinds of matter, they can reach Earth without being absorbed or scattered by its atmosphere. This gives radio astronomy a critical advantage over other observing techniques, e.g., gamma-ray astronomy, as it can be done from the ground, rather than needing satellites in space. On top of that, unlike other ground based observations, e.g., in the optical, radio telescopes can be used in the daytime as well as at night. Even though AGN are amongst the strongest radio sources in the sky, their observable radiation is extremely weak, so radio telescopes require large antennas and dishes to collect enough radiation to study them, and extremely sensitive receiving equipment. Radio astronomers are usually interested in how “bright” an object is and have therefore defined the emitted power per unit solid angle and frequency as the flux density S of a source. In honor of Karl G. Jansky the commonly used unit is called Jansky, defined as $10^{-26} \text{ Wm}^{-2}\text{Hz}^{-1}$. In this chapter, an overview of the basic techniques of single-dish radio astronomy with focus on the Effelsberg 100-m telescope will be given. Moreover, the TELAMON program, which is using the Effelsberg 100-m telescope to monitor radio spectra of AGN, is introduced and the sample and data reduction used for these observations is explained in detail. On top of that, the calibration procedure and several secondary analysis steps that help to study the variability and spectra of AGN are presented.

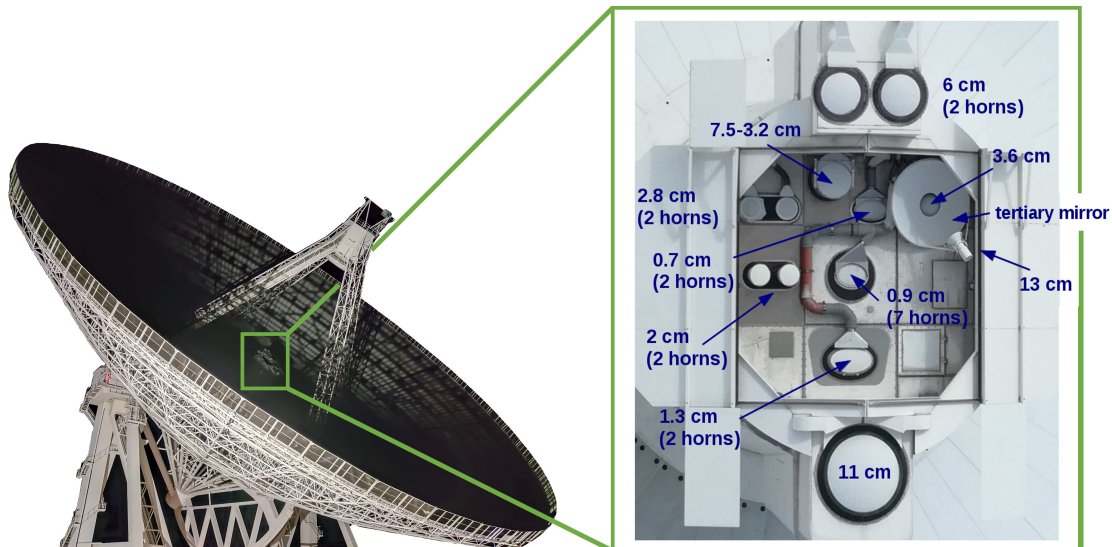


Fig. 3.1: *Left:* The Effelsberg 100-m-telescope located in Effelsberg, Germany. *Right:* Picture of the secondary receiver cabin including the used receivers at 14 mm (here: 1.3 cm) and 7 mm (adapted from the Effelsberg Wiki¹)

3.1 The Effelsberg 100-m Telescope

For all observations presented in this thesis, the Effelsberg 100-m telescope, located in Effelsberg, Germany, was used. Detailed information can be found in [Bach & Kraus \(2018\)](#), on which this section is also mainly based. The telescope is operated by the Max-Planck Institute for Radio Astronomy in Bonn, Germany. It is one of the largest fully steerable single-dish radio telescopes in the world and a unique high-frequency radio telescope in Europe. The telescope can be used to observe radio emission from celestial objects in a wavelength range from 90 cm (300 MHz) down to 3.5 mm (90 GHz). The reflector dish has a very high surface accuracy with a mean deviation from ideal parabolic shape of only ~ 0.5 mm (rms). On top of that, the telescope is constructed in such a way that the pull from gravity keeps the dish in a parabolic shape (with well-defined, but shifted focal point), regardless of the current elevation. This principle is called 'homologous distortion' and enables very sensitive observations to be made at high radio frequencies (i.e., $\nu > 10$ GHz). The telescope is able to perform a wide variety of observations due to the good angular resolution, the high sensitivity and a large number of receivers in the primary and in the secondary focus (see Fig. 3.1). There are a number of different back-ends available that allow for different observing modes, i.e., spectroscopic observations (atomic and molecular transitions in a wide frequency range), high time-resolution (pulsars, Fast Radio Bursts) or mapping of extended areas of the sky. The telescope is also part of some of the most important interferometric networks (e.g., IVS, mm-VLBI, EVN and Global-VLBI). For this work, the 14 mm and 7 mm secondary focus receivers are used in continuum observing mode.

3.2 Technical Background

When observing astronomical sources with a telescope, one somehow has to measure their signal or emitted power. In this section, a brief explanation of how this process works for radio telescopes in general is given. For further details, the reader is encouraged to look at the main resource of this section by [Kraus \(1966\)](#). First, let us introduce the angular resolution Θ of a telescope, which describes the ability to distinguish two distinct features of an observed object. The angular resolution is limited by the Rayleigh criterion

$$\Theta \approx \frac{\lambda}{D}, \quad (3.1)$$

where λ denotes the observed wavelength and D the telescope diameter. If two emitters lie within Θ as seen from the telescope, they appear as one source in the received signal. For the Effelsberg telescope ($D = 100$ m), a typical angular resolution when observing, e.g., with the 14 mm receiver is $\Theta \sim 35''$. The main beam B of a radio telescope with diameter D , observing at wavelength λ , is described by a Gaussian with Half Power Beam Width (HPBW) equal to the angular resolution Θ :

$$B = \exp \left[-4 \ln(2) \left(\frac{\phi}{\Theta} \right)^2 \right], \quad (3.2)$$

where ϕ is the radial angle on the sky as measured from the beam center. The signal received by a telescope is the convolution of the intrinsic source distribution and the antenna beam B . This is illustrated in [Fig. 3.2](#), where one can see an exemplary source distribution and its convolution with the antenna pattern B . First, one can see that point-like sources are observed as a Gaussian signal. If two point sources are too close together (below the angular resolution limit defined in [Equation \(3.1\)](#)), they also appear as one Gaussian curve. Note that the telescope beam is usually more complex than just a Gaussian curve, i.e., including sidelobe structures, however, a detailed presentation of this would go beyond the scope of this work. The received power P from a source depends on the source flux density S , the collecting area A of the antenna, the aperture efficiency η_a of the telescope and the receiver bandwidth $\Delta\nu$. It is given by

$$P = \frac{1}{2} \cdot S \cdot A_{\text{eff}} \cdot \Delta\nu \quad (3.3)$$

with $A_{\text{eff}} = \eta_a A$. The aperture efficiency η_a accounts for various losses that reduce the gain of the antenna from the maximum that could be achieved with the given aperture. In theory, it can be calculated by

$$\eta_a = \eta_0 \cdot \exp \left[-\alpha \left(\frac{4\pi\sigma}{\lambda} \right)^2 \right]. \quad (3.4)$$

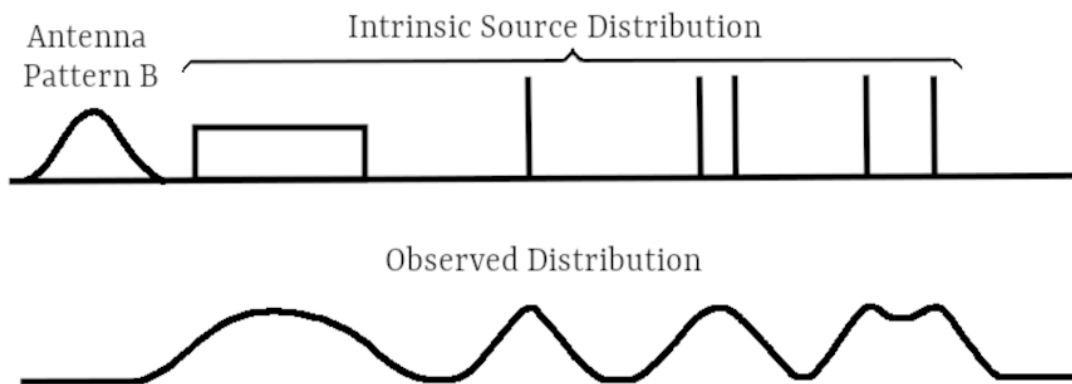


Fig. 3.2: Exemplary source distribution (top) and the same distribution convoluted with the antenna pattern B (bottom). A point source is always observed as a Gaussian signal, if the antenna pattern is Gaussian (adapted from Kraus, 1966).

η_a depends on the wavelength λ , the rms of the reflector σ and a constant η_0 . α is the Ruze loss correction factor that describes the gain loss due to the reflector shape and can vary between 0 and 1 (Ruze, 1966). For the Effelsberg telescope in its current configuration, these values have been determined by Bach et al. (2007) as $\eta_0 = 0.55$, $\alpha = 0.78$ and $\sigma = 0.9$ mm. If the equivalence of power and temperature

$$P = k_B \cdot T \cdot \Delta\nu \quad (3.5)$$

is considered, with Boltzmann constant k_B , one can associate an antenna temperature T_{src} with every observed radio source of flux density S via

$$T_{\text{src}} = \frac{SA_{\text{eff}}}{2k_B} = S \cdot \Gamma, \quad (3.6)$$

where $\Gamma = \frac{A_{\text{eff}}}{2k_B}$ is called the sensitivity of the telescope. With the telescope one usually measures T_{src} (plus background, see Sect. 3.4.2). The relevant quantity, however, is the flux density S of the source. This means, the sensitivity Γ of the telescope needs to be determined in order to convert T_{src} into units of flux density. In principle, one can calculate Γ by its definition

$$\Gamma = \frac{A_{\text{eff}}}{2k_B} = \frac{\eta_a A}{2k_B} = \frac{\eta_a \pi D^2}{8k_B}, \quad (3.7)$$

using the telescope specific parameters D and η_a . As introduced earlier, η_a depends on multiple parameters, i.e., the wavelength λ , the surface accuracy σ or aperture blocking. As a result of this, it is not easy to determine η_a precisely. Therefore, it is common practice to measure the sensitivity Γ by observing calibrator sources with known flux

density S_{cal} , multiple times during an observing session. From the observed antenna temperature of the calibrator source T_{obs} one can derive the sensitivity

$$\Gamma = \frac{T_{\text{obs}}}{S_{\text{cal}}}. \quad (3.8)$$

In this context, it is convenient to define the inverse sensitivity as the calibration factor $\Gamma_{\text{c}} = \Gamma^{-1}$.

3.3 General Observing Procedure & Sample

This thesis is mainly based on observations carried out with the Effelsberg 100-m telescope, as part of the TELAMON (TeV Effelsberg Long-Term AGN Monitoring) program (Kadler et al., 2021). This program is designed to monitor the radio spectra of AGN, namely TeV-blazars and candidate neutrino AGN with the Effelsberg telescope since August 2020. The main TELAMON sample consists of TeV-detected and neutrino-candidate AGN, excluding bright low-peaked blazars, which are well covered in other monitoring programs. As a selection criterion, all sources whose low-state flux density falls below 500 mJy are included. The complete sample, consisting of 44 sources is presented in Table 3.1. It consists of 18 XBLs (i.e., $\nu_{\text{peak}} > 10^{17}$ Hz, and sources from Biteau et al., 2020), 12 HBLs (i.e., 10^{15} Hz $< \nu_{\text{peak}} < 10^{17}$ Hz), 6 FSRQs, 5 IBLs, 1 LBL and 1 Radio Galaxy (RG). J0509+0541 (TXS 0506+056) is included in the HBL count due to its high peak frequency found in the literature. For J0316+4119 (IC 310), a clear characterization is not yet possible since the source shows some Blazar-like properties but its jet might be misaligned by 10–20° from the line of sight (Ahnen et al., 2017). The prime research subject of the TELAMON program are HBLs and XBLs, other sources are included to allow for statistical comparison. Every two to four weeks, high-cadence observations of these sources are performed at multiple high radio frequencies up to $\nu = 44$ GHz. For the observations, the 14 mm and 7 mm receivers of the Effelsberg 100-m telescope are used in continuum observing mode with the backend “dual-spec-OPTOCBE” since August 2020. This results in four sub-bands (centered at 19.25 GHz, 21.15 GHz, 22.85 GHz and 24.75 GHz) for the 14 mm receiver and another four sub-bands (centered at 36.25 GHz, 38.75 GHz, 41.25 GHz, 43.75 GHz) for the 7 mm receiver. Since spring 2021, the 20 mm receiver has been added, but due to the limited data available is not analyzed in this thesis. All receivers are equipped with two horns. The first horn is pointed directly at the target and passes the signal directly to the receiver. The second horn is pointed at the atmosphere off-source and is used to subtract weather effects from the first horn. This is important, because at the observed frequencies Earth’s atmosphere (especially on cloudy days) emits thermal radiation that

Table 3.1: The TELAMON sample of TeV-emitting and neutrino-candidate AGN. The classification into XBL, HBL, IBL and LBL is performed according to the synchrotron peak frequency found in the literature. The presented references are related to the synchrotron peak frequency and the redshift value.

ID (J2000)	Alternative Name	Class	Synchr. Peak $\text{Log}_{10} \left(\frac{\nu_{\text{peak}}}{\text{Hz}} \right)$	Redshift ^a	Reference ^b
J0035+5950	1ES 0033+595	XBL	18.2	0.086	[1]
J0112+2244	S2 0109+22	IBL	~ 15	0.4	[2]
J0214+5144	TXS 0210+515	XBL	17.3	0.049	[1]
J0221+3556	S3 0218+35	FSRQ	-	0.954	[3]
J0222+4302	3C 66A	HBL	15.63	0.34	[4]
J0232+2017	1ES 0229+200	XBL	18.5	0.139	[1]
J0242+1101	PKS 0239+108	FSRQ	-	2.68	[7]
J0303-2407	PKS 0301-243	HBL	15.7	0.266	[1]
J0316+4119	IC 310	RG/XBL	17	0.0189	[6]
J0416+0105	1ES 0414+009	XBL	16.5	0.287	[1]
J0507+6737	1ES 0502+675	XBL	17.9	0.34	[1]
J0509+0541	TXS 0506+056	IBL/HBL	15.34	0.3365	[4]
J0521+2112	RGB J0521+212	IBL	15.1	0.108	[1]
J0650+2502	1ES 0647+250	HBL	16.7	0.203	[1]
J0658+0637	NVSS J065844+063711	HBL	15.5	0.23	[1]
J0913-2103	MRC 0910-208	XBL	17.1	0.198	[1]
J0955+3551	3HSP J095507.9+355101	XBL	17.7	0.557	[1]
J1015+4926	1ES 1011+496	HBL	16.4	0.2	[1]
J1058+2817	GB6 J1058+2817	XBL	18.37	0.4793	[4]
J1104+3812	Mrk 421	XBL	16.3	0.03	[1]
J1136+7009	Mrk 180	HBL	16.8	0.045	[1]
J1145+1936	3C 264	RG	-	0.0216	[5]
J1217+3007	ON 325	HBL	15.58	0.131	[4]
J1221+2813	W Comae	IBL	14.84	0.102	[4]
J1221+3010	1ES 1218+304	XBL	16.8	0.18	[1]
J1230+2518	ON 246	IBL	15.0	0.135	[1]
J1422+3223	OQ 334	FSRQ	-	0.681	[8]
J1427+2348	OQ 240	HBL	15.7	0.647	[4]
J1428+4240	1ES 1426+428	XBL	18.1	0.129	[1]
J1443+2501	PKS 1441+25	FSRQ	-	0.939	[9]
J1518-2731	TXS 1515-273	HBL	15.3	0.14	[1]
J1542+6129	GB6 J1542+6129	IBL	14.72	0.507	[4]
J1555+1111	PG 1553+113	HBL	15.6	0.36	[1]
J1653+3945	Mrk 501	XBL	17.9	0.03	[1]
J1728+1215	PKS 1725+123	FSRQ	-	0.586	[10]
J1728+5013	IZw 187	XBL	17.0	0.055	[1]
J1743+1935	1ES 1741+196	XBL	17.8	0.08	[1]
J1813+3144	B2 1811+31	FSRQ	15.0	0.117	[1]
J1958-3011	1RXS J195815.6-301119	XBL	17.0	0.119	[1]
J1959+6508	1ES 1959+650	XBL	16.9	0.047	[1]
J2018+3851	TXS 2016+386	LBL	13.508	-	[11]
J2158-3013	PKS 2155-304	HBL	15.4	0.117	[1]
J2243+2021	RGB J2243+203	XBL	15.1	-	[1]
J2347+5142	1ES 2344+514	XBL	17.7	0.044	[1]

^a For some sources, no redshift was found in the given reference. In these cases, if available, the redshift value was taken from either SIMBAD (<http://simbad.u-strasbg.fr/simbad/>) or NED (<https://ned.ipac.caltech.edu/>). For a couple of sources, the redshift is still undetermined. ^b Reference for redshift and peak frequency: [1] Chang et al. (2019), [2] Ciprini et al. (2004), [3] Paiano et al. (2017), [4] Nieppola et al. (2006), [5] Ahn et al. (2012), [6] Ahnen et al. (2017), [7] Sowards-Emmerd et al. (2005), [8] Abazajian et al. (2009), [9] Shaw et al. (2012), [10] Shaw et al. (2013), [11] Ackermann et al. (2015)

needs to be accounted for. In order to measure the flux densities of the sources, cross-scans are performed on the targets, consisting of typically 8 sub-scans at 14 mm and 16 sub-scans at 7 mm. A “cross-scan” means that the telescope hovers over the point-like source region in azimuth- and elevation-direction multiple times while measuring the antenna temperature of the receiver. About every four hours, a calibrator source is observed in order to focus the telescope and to extract calibration factors (see Sect. 3.4.3). This setup is well suited to trace dynamical processes in the compact parsec-scale jets of blazars related to high-energy flares or neutrino detections.

3.4 Raw Data Reduction

The general data analysis for pointed flux density measurements with the Effelsberg 100-m telescope is described in detail by Heßdörfer (2021), as well as by Angelakis et al. (2019). Some of the most important aspects will be recited here, but the focus will mainly be on the changes and improvements implemented since Heßdörfer (2021). The major improvements presented here are a semi-automated flag algorithm, a new calibration procedure and an in-depth error discussion. The raw data output of every scan, namely radiation temperatures, need to be converted into astrophysical units, that can be interpreted and compared with other measurements. In this section, the process of deriving flux density values from the observed data is explained. On top of that, secondary analysis steps, i.e., a sub-band averaging process and the derivation of spectral indices are presented.

3.4.1 Sub-scan Fitting

As mentioned in Sect. 3.3, every scan of a source at a specific frequency consists of multiple sub-scans. An example of this is shown at the bottom of Fig. 3.3, where one can see four sub-scans in azimuth (blue) and four sub-scans in elevation (orange). These multiple sub-scans are used to calculate one flux density value for each frequency per scan. First of all, for every scan, all azimuth sub-scans are used to generate a single average azimuth scan and all elevation sub-scans are used to generate a single average elevation scan. In Fig. 3.3, these averaged scans are shown at the top. Since all of the sample sources are assumed to be point-like, a Gauss curve is fitted to both average scans (see Fig. 3.3, top). At this point, it is important to perform a data quality check, to see if all sub-scans can be considered “good” scans. This is important, since some sub-scans might be damaged due to radio frequency interference (RFI), telescope errors or atmospheric effects, and therefore might lead to errors in the flux density values.

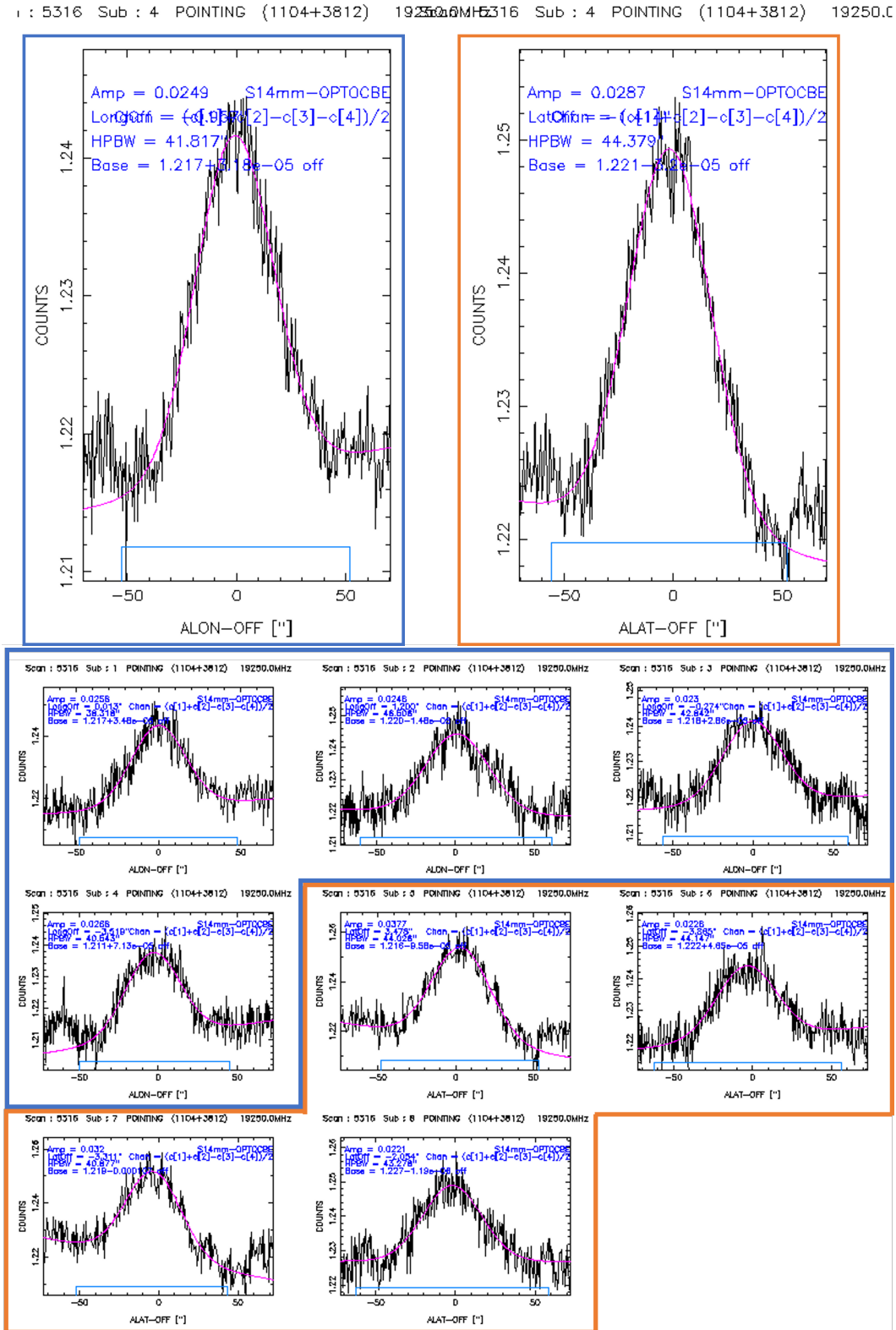


Fig. 3.3: Example of a typical flux density measurement performed as a cross-scan from the Effelsberg analysis tool (Mrk 421 at 19.25 GHz on July 28th, 2021). *Top:* Averaged Longitude (left) and Latitude (right) scan on the source. A Gaussian fit is performed (pink line) which is used to derive the source temperature (amplitude). *Bottom:* Sub-scans of the averaged scan above. The combination of the first four scans (blue) is used to construct the average scan in Longitude. The combination of the last four scans (orange) is used to construct the average scan in Latitude.

In order to filter out “bad” sub-scans, a flagging system has been developed, that uses multiple criteria to detect bad scans. A scan is flagged if at least one of the following criteria applies:

- The full-width at half maximum (FWHM) of the Gauss fit of either the azimuth or elevation or both average scans deviates by more than 30% from the HPBW (depending on frequency: 19.25 GHz \rightarrow 40”; 21.15 GHz \rightarrow 38”; 22.85 GHz \rightarrow 36”; 24.75 GHz \rightarrow 34”; 36.25 GHz \rightarrow 24”; 38.25 GHz \rightarrow 22”; 41.25 GHz \rightarrow 20”; 43.75 GHz \rightarrow 19”). *Reason: The FWHM of a point-source scan is restricted by the angular resolution limit (beam width), depending on the observing frequency. Therefore, it should stay constant for each frequency and not vary too much from source to source. There can be small positional telescope uncertainties throughout the sub-scans that lead to a slightly different FWHM of the averaged source scan, but these changes should not exceed 30%. This flag type is typical for windy observing sessions, where the telescope’s position changes slightly from sub-scan to sub-scan by wind gusts, or in cases where the source is below the detection limit and atmospheric background is fitted.*
- The Gaussian fit of either azimuth or elevation or both average scans has negative amplitude. *Reason: The sources are expected to be point-like radio emitters, this means one expects to observe a Gauss signal with peak. Since a negative amplitude indicates a dip in the Gaussian, there is something wrong with one or more sub-scans. It can also indicate that the source is below the detection limit and not visible at all, i.e., only background noise is fitted.*
- The maximum of the Gauss fit of either azimuth or elevation or both average scans has an offset from the scan center greater than 20% of the HPBW. *Reason: The Gauss fit is expected to be centered in azimuth and elevation scans. If this is not the case, the cross scan has missed the source center by several arcseconds. In principle, these cases are corrected in the analysis (see Sect. 3.4.2), but at a level of more than 20% of the beam width this offset correction is not accurate anymore.*
- The amplitudes of the Gauss fits of azimuth and elevation average scans differ by more than 15%. *Reason: The source is expected to be point-like and centered in azimuth and elevation scans. This means the average scans in azimuth and elevation should have similar amplitudes. If amplitudes differ by more than 15% this is an indication of bad underlying sub-scans included in the average scan.*

Note that the exact limits that indicate when a scan is flagged rely on experience. The chosen values have proven to be well suited for the analysis in the used frequency bands.

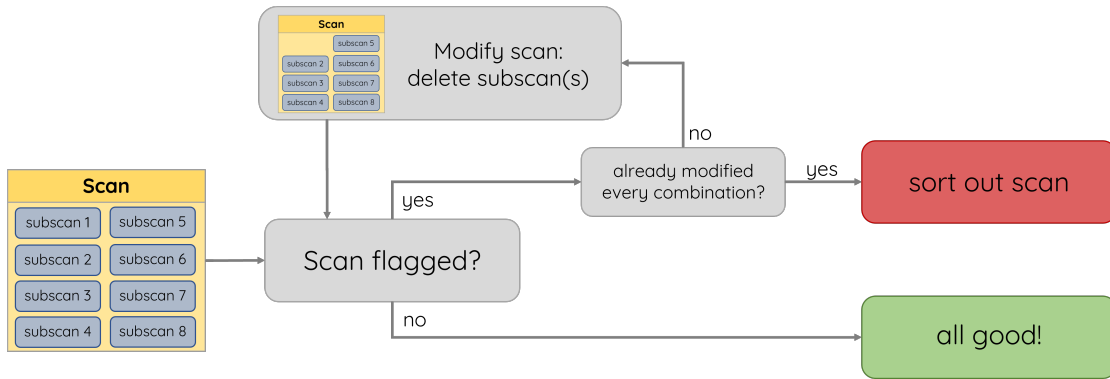


Fig. 3.4: Scheme of the semi-automated flag algorithm used to sort out bad (sub-)scans.

If an averaged scan is flagged according to these criteria, it is not trivial to judge whether the source was below the detection limit (not visible in all sub-scans) or if there were simply a few “bad” sub-scans by not looking at the individual sub-scans for every source. As shown by Heßdörfer (2021), a manual analysis of individual sub-scans is possible but very tedious, time-consuming, and also not clearly reproducible since it depends on the analyzer’s individual eyes. Therefore, a semi-automated analysis tool has been developed which takes care of detecting and sorting-out “bad” sub-scans. The general principle of the algorithm is illustrated in Fig. 3.4. For every scan (usually consisting of 8 or 16 sub-scans), it is first checked if the averaged scan is flagged. If the scan is not flagged, it will be used as-is for the next analysis steps without performing any changes. If the scan is flagged, the algorithm tries to remove one (arbitrary) sub-scan and checks if the average scan (excluding the removed sub-scan) is still flagged. If this new average scan is not flagged, the average scan, excluding the deleted scan, will be used for further analysis steps. If the new average scan is still flagged this procedure goes on until the algorithm has found a combination of removed sub-scans that leads to a non-flagged average scan. To be conservative, the algorithm allows for only one sub-scan in total to be removed from the initial scan. If the average scan is still flagged after trying to remove all sub-scan combinations, the scan is sorted out as a “bad” scan and it is not used for further analysis. On first note, this brute-force approach may sound quite time consuming, since in the worst case (scan sorted out) every scan has to be averaged and flag-checked up to 8 times. Moreover, a typical outcome of an observing epoch is in the range of 50-100 scans per frequency, so this number adds up quite a lot. In order to enhance computational performance, parallel processing with up to 24 CPU cores (and therefore 24 scans iterated over simultaneously) is used for the analysis. This is realized in `python3` using the `joblib`, `parallel` libraries. A typical observing epoch can then be analyzed in $\lesssim 1$ hour compared to ~ 4 hours in the manual case. The automated analysis quality is superior to the manual analysis since every sub-scan deletion can be tried out, instead of simply judging by the human eye what sub-scan deletion might

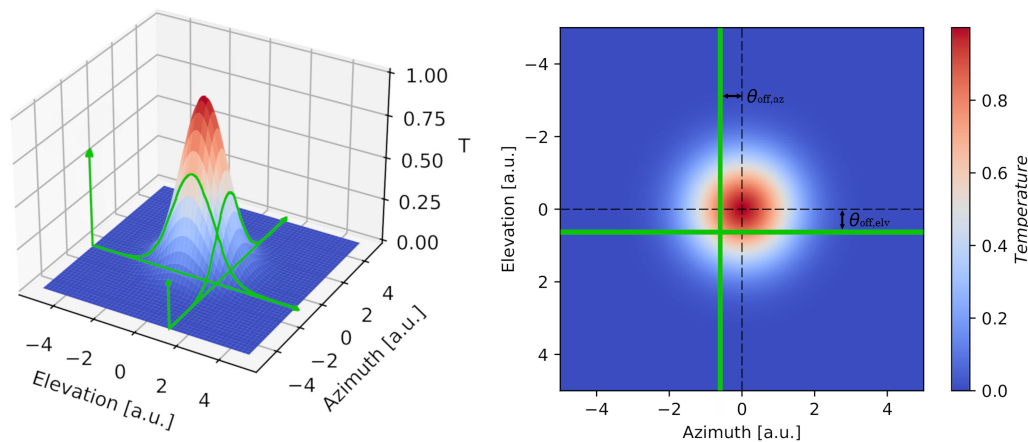


Fig. 3.5: 3D (left) and 2D (right) profile of an ideal point source in k-space. The green lines illustrates a slightly off-source cross-scan that requires pointing correction.

improve the overall fit quality. On top of that, due to the appointed flagging criteria, it is completely reproducible. As a final check, the data are again inspected manually to sort out any outliers and left-over bad scans that the algorithm was not able to detect.

3.4.2 Data Corrections

In Sect. 3.3, the source temperature T_{src} was introduced, but the telescope actually measures a signal T_{obs} in units of counts, that needs to be translated into units of temperature. In order to do this, one needs the temperature of the receiver noise diode T_{cal} in Kelvin, which depends on receiver and frequency but is well known and documented.² From this, the actual antenna temperature T_{A} can be calculated:

$$T_{\text{A}} = T_{\text{cal}} \cdot T_{\text{obs}}. \quad (3.9)$$

As mentioned earlier, cross-scans are performed on every source, but it is almost impossible to center these scans at the exact source position. This is illustrated in Fig. 3.5. Since all of the sample sources are assumed to be point-like, their signal, shown on both plots in Fig. 3.5, is expected to be Gaussian. If a cross-scan misses the center of a source (as illustrated by the green lines) the measured amplitudes in elevation and azimuth scans are lower than the peak amplitude. But this peak amplitude is what is needed to calculate the flux density of the source. Since offsets for elevation and azimuth scan $\theta_{\text{off,az/elv}}$ are determined from the fit, both scans can be combined to calculate the peak

²https://eff100mwiki.mpifr-bonn.mpg.de/doku.php?id=information_for_astronomers:rx_list

amplitude of the (3D-)Gauss distribution

$$T'_A = T_{A,\text{elv/az}} \exp \left[4 \ln 2 \left(\frac{\theta_{\text{off,az/elv}}}{\theta_{\text{HP}}} \right)^2 \right]. \quad (3.10)$$

Here, $T_{A,\text{elv/az}}$ denotes the antenna temperature of elevation or azimuth scan, respectively. $\theta_{\text{off,az/elv}}$ stands for the offset of the Gaussian fit from the scan center of azimuth or elevation scan as indicated in Fig. 3.5. θ_{HP} is the HPBW of the observed frequency and should be equal for azimuth and elevation scan. Notice, that Equation (3.10) is actually two equations, since one can calculate either $T'_A(T_{A,\text{elv}}; \theta_{\text{off,az}})$ or $T'_A(T_{A,\text{az}}; \theta_{\text{off,elv}})$. The mean of these two values is used as a final value for T'_A . The antenna temperature T'_A is still not equivalent to the source temperature T_{src} , it rather is a combination of various background noise and T_{src} . First of all, there is the temperature of the receiver itself, T_{rec} , that contributes to the thermal noise. In order to minimize this effect, the receivers of the telescope are cooled, which results in T_{rec} values from a few to several tens of Kelvin. In addition, depending on antenna and elevation, the telescope receives a spill-over (thermal radiation) signal, T_{ground} , from the ground. Finally, there is also noise coming from the sky, T_{sky} , which includes any form of radiation from the sky including the source itself and other forms of radiation, e.g., atmospheric radiation or cosmic microwave background (CMB) radiation. Therefore, the temperature measured by the telescope system is defined as

$$T_{\text{sys}} = T_{\text{rec}} + T_{\text{ground}} + T_{\text{sky}} (\text{incl. } T_{\text{src}}). \quad (3.11)$$

As already mentioned, T_{rec} is usually on the order of a few Kelvin and kept under control by cooling the receiver. The same goes for T_{ground} , its impact is small, therefore one can focus on T_{sky} to extract T_{src} . T_{sky} includes the source temperature but also CMB radiation and atmospheric radiation. Again, one should note that CMB and atmospheric radiation are on the order of a few Kelvin and can therefore be neglected. This would imply that $T_{\text{sys}} = T_{\text{src}}$ is assumed, but Earth's atmosphere absorbs some parts of the radiation. As shown in Fig. 3.6, the amount of atmosphere that the radiation passes through depends on the elevation of the source at the time when it was observed. When observing at high elevation, the atmospheric absorption is lower than when observing at low elevation. Therefore, an additional correction has to be applied to the antenna temperature T'_A :

$$T''_A := T'_A \cdot e^{\tau \cdot AM}, \quad (3.12)$$

where τ denotes the zenith opacity and AM is the ‘‘airmass’’, defined as $AM = 1/\sin(\epsilon)$. The zenith opacity τ is determined by a water-vapor radiometer near the telescope by measuring the strength of the 22 GHz water-vapor line.

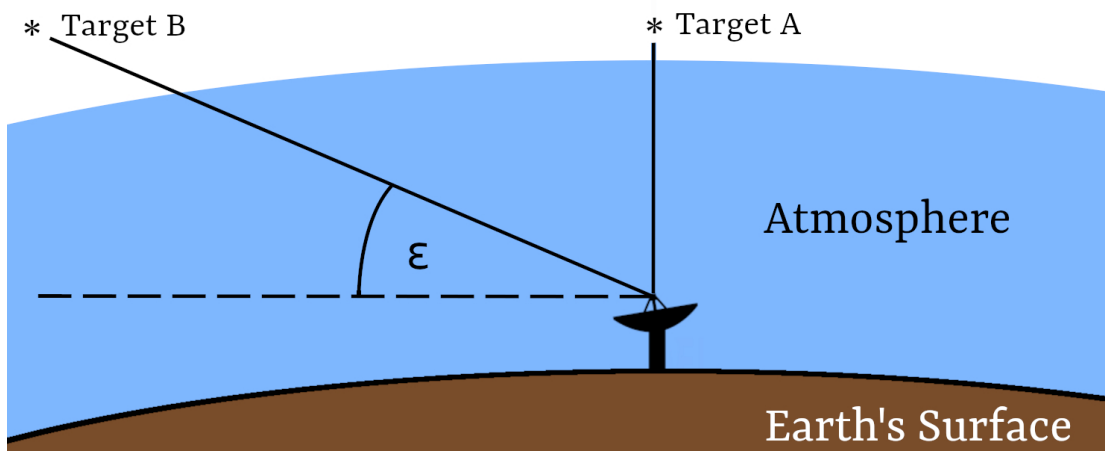


Fig. 3.6: Illustration of the effect of “airmass”: If one observes Target A at zenith (elevation 90°) the radiation passes through a much shorter distance of atmosphere (airmass) as compared to observing Target B at lower elevation ϵ . Since Earth’s atmosphere absorbs radiation, this effect needs to be taken into account when reducing the data.

Finally, one needs to account for the gain curve, which is also dependent on the elevation. The Effelsberg telescope is optimized to a parabola at 32° elevation. As mentioned in Sect. 3.1, the telescope uses the principle of homologous distortion to keep this parabola shape at other elevations, but this results in a gain drop at higher and lower elevations. The gain curve G is parametrized as a polynomial of second order

$$G(\epsilon) = A_0 + A_1 \cdot \epsilon + A_2 \cdot \epsilon^2, \quad (3.13)$$

which depends on the elevation ϵ . The parameters A_i are well determined and can be found on the receiver information website cited earlier. The final source temperature, including all of the previously performed corrections, is given by

$$T_{\text{src}} = \frac{T''_{\text{A}}}{G(\epsilon)} = \frac{T'_{\text{A}} \cdot e^{\tau \cdot AM}}{G(\epsilon)}, \quad (3.14)$$

where T'_{A} is the pointing-corrected antenna temperature, as defined in Equation (3.10).

3.4.3 Calibration

3.4.3.1 Calibrator Sources

Previously, it was shown how T_{src} can be translated into flux density values by using the sensitivity Γ , as defined in Equation (3.8) or its inverse, the calibration factor Γ_c . In this section, it is discussed how exactly the calibration factor for the analysis is determined. Calibration of telescopes is a highly non-trivial process. Since one wants to measure and compare source flux densities in units of Jy, some kind of absolute flux

density scale to compare measurements with is required. Early works in this field (e.g., Baars et al., 1977, and references therein) used small single dish telescopes with well known aperture efficiency (and therefore well known sensitivity) to measure the flux density of very bright, compact sources, e.g., Cas A, that can then be used to determine the sensitivity of larger telescopes. However, these bright sources are very rare and therefore not well suited as daily calibrators. On top of that, their high flux densities in comparison to potential observing targets could lead to non-linearity problems in low-noise receivers. Therefore, Baars et al. (1977) have introduced a set of secondary calibrators that can be used on a day-to-day basis for calibration purposes. Their flux density is very constant over long periods of time (several decades) and they are also very compact sources. These secondary calibrators have been further investigated and monitored by Ott et al. (1994) and most lately by Perley & Butler (2013, 2017). According to the latest publication (Perley & Butler, 2017), the best suited calibrators in the TELAMON frequency range (19 GHz–44 GHz) are 3C 286 and 3C 295. They are therefore used as calibrator sources in this work. Perley & Butler (2017) provide parametrized spectra for these sources, that are used to calculate the frequency dependent calibrator flux densities for this thesis. Since 3C 295 is quite faint ($\lesssim 1 Jy$) at higher frequencies ($\nu \gtrsim 35 GHz$) and therefore not always detectable (especially during bad weather sessions), the sources NGC 7027 and W3(OH) are also included as calibrator sources. NGC 7027 is a planetary nebula and has been proposed as a secondary calibrator by Baars et al. (1977) but has later been found to be variable. Still, this source can be used as a calibrator, since its variability has been well characterized by Zijlstra et al. (2008). The spectral model provided in this paper is used to calculate time-dependent calibration flux densities for NGC 7027. W3(OH) is a star forming region that exhibits a strong water maser in the 14 mm band (Hachisuka et al., 2006). Therefore, it is excluded for 14 mm calibration, but since the source is very bright at 7 mm ($\approx 3 Jy$) it is useful as a substitute for 3C 295 in this band. The spectral model of W3(OH) used for the calibration has been created by Alex Kraus (priv. comm.) using Effelsberg data and assuming a free-free emission model. Due to their brightness, the two main calibrators observed with highest priority are 3C 286 and NGC 7027. 3C 295 is used as a backup calibrator at 14 mm and W3(OH) as a backup calibrator at 7 mm.

3.4.3.2 Calibration Procedure

As mentioned in Sect. 3.3, usually one of the secondary calibrator sources are observed every four hours during an observing session to determine the calibration factor. This calibration measurement typically consists of up to three scans per frequency on the calibrator. Equation (3.8) is used to determine the calibration factor ($\Gamma_c = 1/\Gamma$) for

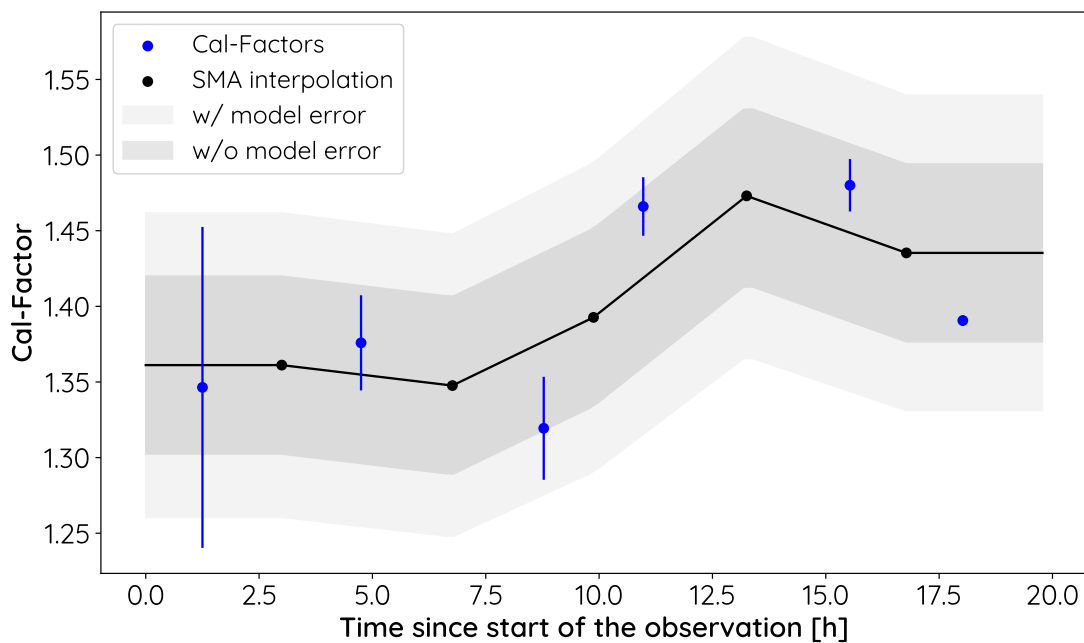


Fig. 3.7: Exemplary calibration factor evolution at 38.75 GHz during the observing session on Oct 24, 2021. The blue data points correspond to the (sub-)averaged calibration factor measurements $\Gamma_{c,i}$. The black line indicates the SMA-interpolated calibration factor $\Gamma_{\text{SMA},i}$ (see Equation (3.15)), as used in the final analysis. The dark gray area represents the calibrator scatter $\sigma_{sc,\nu}$, while the light gray area represents the total calibration uncertainty σ_{cal} , including the model error σ_{model} and $\sigma_{sc,\nu}$.

each one of these scans. If there was more than one scan on the calibrator at the same time, the mean and standard deviation are calculated to get a value with error for the total calibration factor at any given time. In the special case of only one calibrator measurement the error is estimated, depending on the frequency (see Sect. 3.4.4). For each observing session, one therefore gets a calibration factor for every ~ 4 hours, in the ideal case. In a lot of epochs, especially during the beginning of the program, there are less calibration measurements, due to a still inexperienced observer team. An example is given in Fig. 3.7, where all calibration factor data points (blue) are averages of the underlying (multiple) calibrator scans at the time. When talking about calibration factors in the following, it is referred to these, already (sub-)averaged calibration factors like the (blue) ones presented in Fig. 3.7.

In principle, the calibration factor only depends on the telescope's sensitivity at a given frequency and should therefore be constant throughout an observing session (for a given frequency). As one can see in Fig. 3.7 this is not always the case. The calibration factor does change throughout the observing session, mostly due to temperature changes which affect the ideal focus position. If the telescope is out of focus, the received signal is weaker and therefore the calibration factor rises. The telescope is being kept in focus by readjusting the focus every four hours (or more often in the case of significant

temperature drops) to keep the calibration factor constant, but still the calibration factor varies throughout the observation. The de-focusing of the telescope also turns out to be a major issue in early epochs due to the limited number of calibration and focus scans performed by the still inexperienced observer team. Modelling the behaviour of the focus is non-trivial, since it is unknown how much of the calibration factor fluctuation is statistical and how much is systematic due to, e.g., shifting focus. If the fluctuation was solely statistical, one would have to take the mean calibration factor throughout the entire session. If the fluctuation was solely systematic it would be best to linearly interpolate between the calibration factors. In the present case, however, interpolation between all data points would be an over-interpretation of the data and taking the mean cannot account for the fluctuation of the calibration factor. In order to take this fluctuation into account and also not to over-interpret the data points, the calibration factor is modelled using a simple moving average (SMA) interpolation (Chou, 1975). This is essentially a combination of both methods, since first, the mean between two adjacent calibration factor values is taken and then it is interpolated between these mean values. If the calibration factor at time t_i is $\Gamma_{c,i}$, the interpolated values are calculated following

$$\Gamma_{\text{SMA},i} = \frac{\Gamma_{c,i} + \Gamma_{c,i+1}}{2}, \quad (3.15)$$

where $\Gamma_{c,i+1}$ is the calibration factor adjacent to $\Gamma_{c,i}$. The same procedure is used for the time interpolation

$$t_{\text{SMA},i} = \frac{t_i + t_{i+1}}{2}. \quad (3.16)$$

If initially there are n calibration factors $\Gamma_{c,i}$, this interpolation will result in $n - 1$ interpolated calibration factors $\Gamma_{\text{SMA},i}$. As indicated by the black line in Fig. 3.7, it is interpolated linearly between the $(t_{\text{SMA},i}, \Gamma_{\text{SMA},i})$ values to get a general expression for the calibration factor, at any given time. For times $t < t_{\text{SMA},1}$, the calibration factor is modelled as constant $\Gamma_{\text{SMA},1}$. Analogously, for times $t > t_{\text{SMA},n-1}$, the calibration factor is modelled as constant $\Gamma_{\text{SMA},n-1}$. If there is only one or two calibration factors available ($n = 1, 2$), a constant calibration factor is assumed for the entire epoch. The interpolation (black line) is used to determine the calibration factor at any given time during the observing session. This means, for every source scan, one calculates the corresponding calibration factor Γ_c using the SMA-interpolation and then uses this calibration factor to calculate the flux density of the source S_{source} following:

$$S_{\text{source}} = T_{\text{src}} \cdot \Gamma_c. \quad (3.17)$$

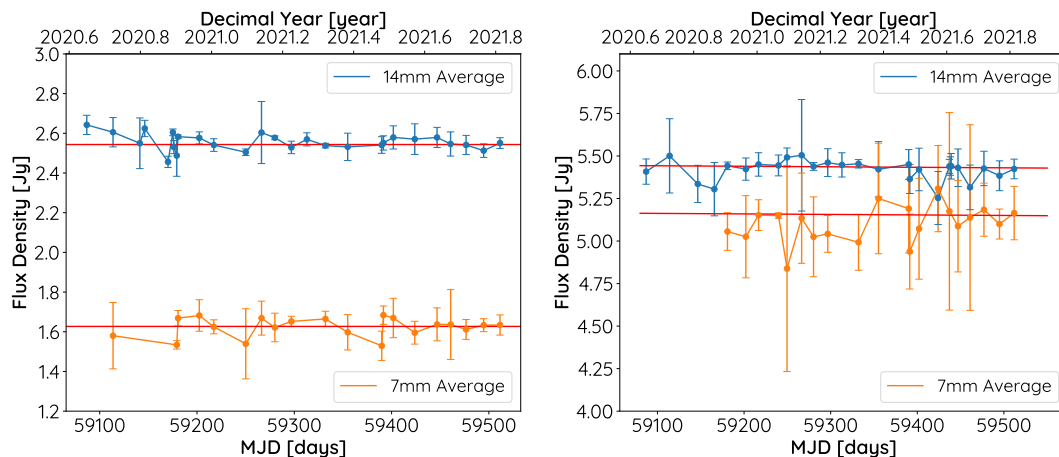


Fig. 3.8: Sub-band averaged light curves of the two main calibrator sources 3C 286 (left) and NGC 7027 (right) at 14 mm and 7 mm. The utilized calibrator model is depicted as a red line which was calculated for the receiver center frequencies 22 GHz (14 mm) and 40 GHz (7 mm) here.

3.4.3.3 Calibration Cross Check

In order to verify that the calibration procedure introduced above is a sensible way to do the calibration, the sub-band averaged light curves of the two main calibrators (3C 286 and NGC7027) are depicted in Fig. 3.8. The sub-band averaging process is described in detail in Sect. 3.5.2, later in this chapter. In Fig. 3.8, one can see the average flux densities for the 14 mm and 7 mm receiver, as well as the utilized calibrator models in red. The calibrator models here are calculated for the receiver center frequencies at 22 GHz (14 mm) and 40 GHz (7 mm). The reduced χ^2 was calculated for all four light curves, in comparison with the underlying calibrator model. Every χ_{red}^2 is on the order of 10^{-2} . This usually indicates that the data describe the model well, but the uncertainties are too large. In the present case, however, the uncertainties represent the error on the average flux density within each band (for details, see Sect. 3.5.2). This corresponds to a frequency range of 19 GHz–25 GHz (14 mm) and 36 GHz–44 GHz (7 mm), while the calibrator model for the plots has been calculated at the exact frequencies 22 GHz (14 mm) and 40 GHz (7 mm). This means, in the present case, $\chi_{\text{red}}^2 \ll 1$ is just an indicator that the calibration procedure works well and justifies the use of the calibration procedure as introduced above.

3.4.4 Error Discussion

In this section, the determination of the total flux density uncertainties σ_{tot} is discussed. The final error has to include the main errors due to the sub-scan-fitting process with the data corrections, σ_{fit} , and the uncertainty of the calibration factor, σ_{cal} .

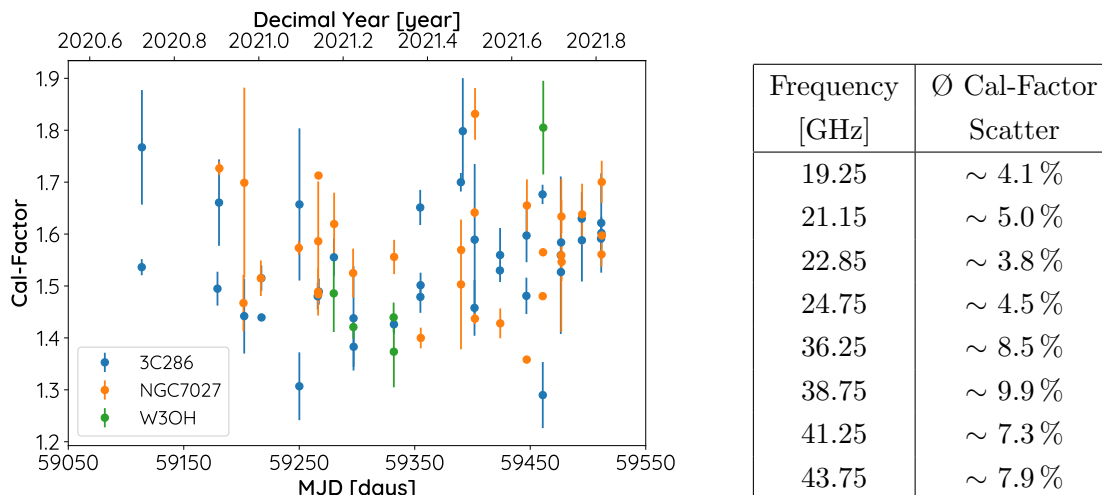


Fig. 3.9 & Table 3.2: Exemplary calibration factor evolution at 41.25 GHz throughout the entire program (left). The table to the right indicates the average calibration factor scattering (standard deviation) since August 2020 for every frequency. The 41.25 GHz value corresponds to the standard deviation of the values on the left.

Let us first discuss the uncertainty due to sub-scan fitting and data corrections, σ_{fit} . This error is calculated through Gaussian error propagation from the fitting and data correction process explained in Sect. 3.4.2. Note that the gain curve is assumed to be free of error here, since the accuracy of the gain curve is also reflected in the fluctuation of the calibration factors and therefore included in the calibration error σ_{cal} . Usually, atmospheric corrections have the biggest impact on the data correction error, especially during bad weather sessions. In total, σ_{fit} is on average of the order $\sim 1\%$.

The main contribution of the flux density uncertainties comes from the calibration error, σ_{cal} . There are two sources of error that determine the total calibration error. First, one needs to consider the fluctuation of the calibration factor $\sigma_{\text{sc},\nu}$ for each frequency and observing epoch. Secondly, one needs to account for the uncertainty of the underlying calibrator model σ_{model} . Let us first discuss how $\sigma_{\text{sc},\nu}$ is determined. As explained in the previous section, an SMA-interpolation is used to calculate interpolated calibration factors. To be conservative, the error of the interpolated calibration factors is assumed to be constant. Therefore, the standard deviation of all (non-interpolated) calibration factors for each frequency and observing epoch is used as the error

$$\sigma_{\text{sc},\nu} = \sqrt{\frac{1}{n-1} \sum_{i=1}^n (\Gamma_{c,i} - \overline{\Gamma_c})^2}, \quad (3.18)$$

where $\overline{\Gamma_c}$ is the mean over the non-interpolated calibration factors $\Gamma_{c,i}$. This error is also illustrated in Fig. 3.7 by the gray background. In the special case where only one calibration factor was measured during an observing epoch, it is non-trivial to determine

a sensible value for this error. In order to deal with this special case, the calibration factor scattering for each frequency from all observing epochs has been analyzed. An exemplary plot of the calibration factor evolution at 41.25 GHz throughout the entire program since August 2020 is shown in Fig. 3.9. In order to derive a sensible error for these epochs, the standard deviation of all calibration factors throughout the program is used to get an estimate of the average calibration factor scatter. This analysis is performed for every frequency band and the typical fluctuation values are given in Table 3.2. The calibration factor scatter plots for all frequencies can be found in Appendix D. As a conservative estimate, a calibration error of 5 % is used at 14 mm and 10 % at 7 mm for epochs with only one calibration factor, following the values from Table 3.2. In Fig. 3.9, one can also see that for some epochs the calibration factor varies more than for others. This is due to focusing problems mainly during early observing sessions, shortly after the beginning of the program. During the early epochs the 4 hour calibration rhythm was not always kept and less calibration/focus measurements were performed. Therefore, most of the epochs where only one calibration measurement was made are during the first months.

On top of the calibration factor scattering $\sigma_{sc,\nu}$, one also needs to take into account the accuracy of the calibrator models σ_{model} . The models of 3C 295 and 3C 286 by Perley & Butler (2017) have an estimated accuracy of 3 % to 5 %, with the larger errors at the lowest (~ 50 MHz) and highest (~ 50 GHz) ends. Since the observations take place from 19 GHz–44 GHz, which is at the higher end of their scale, an error of 5 % for the 3C 295 and 3C 286 models is assumed. For the timely variable model of NGC 7027, Zijlstra et al. (2008) provide an uncertainty of 6 %. It is estimated that the uncertainty for the W3(OH) model is also in the same range, since it has a similar underlying free-free emission model. As a conservative estimate, a general accuracy of the calibrator models of $\sigma_{model}/\Gamma_c = 6\%$ is assumed, which is the maximum error out of the models. One must not use the Gaussian law of error propagation to combine the uncertainties of the different models, since they are not statistically independent and all based on the same flux density scale by Baars et al. (1977). To calculate the total calibration uncertainty σ_{cal} , Gauss addition is performed of the estimated model error σ_{model} and the calibration scatter $\sigma_{sc,\nu}$, which is individual for every epoch and frequency, as described above. The total calibration error is therefore given by

$$\sigma_{cal} = \sqrt{\sigma_{model}^2 + \sigma_{sc,\nu}^2}. \quad (3.19)$$

In order to obtain the total flux density error σ_{tot} , one needs to combine σ_{cal} with the fitting error σ_{fit} . This is done by Gaussian error propagation. Following Equation (3.17), one finds

$$\frac{\sigma_{tot}}{S_{source}} = \sqrt{\left(\frac{\sigma_{cal}}{\Gamma_c}\right)^2 + \left(\frac{\sigma_{fit}}{T_{src}}\right)^2} \quad (3.20)$$

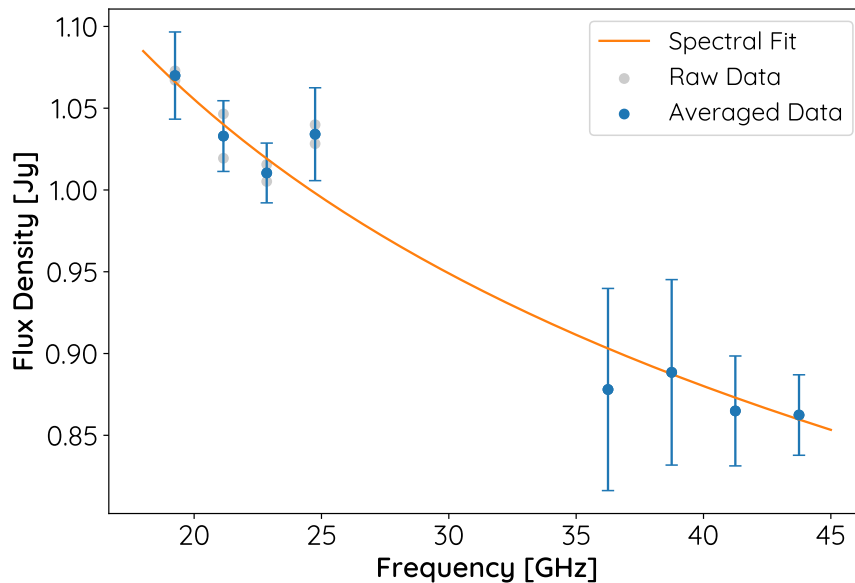


Fig. 3.10: Example of the spectral fitting process (Mrk 501 on July 28, 2021). The light gray dots indicate the raw data, errors are not shown to enhance readability. For every frequency, where more than one raw flux density value is available, the flux densities are averaged (blue dots). The averaged flux densities are then fitted with a power-law spectrum. In the presented case, one finds $\alpha = -0.262 \pm 0.021$.

for the total flux density error. Note that for the following analysis the model error is considered to be zero, since it is purely systematic throughout the entire program. Using it would therefore lead to an overestimation of the statistical flux density error, since the variability only within the program is analyzed in this thesis. If the presented flux density values would be combined with other radio data (using a different flux density scale), or if the absolute flux density values are of interest, the model error has to be taken into account.

3.5 Analysis

In this section, several secondary analysis steps are presented. The calibrated flux density values themselves are difficult to interpret, therefore a sub-band averaging method for multi-frequency light curves is presented. On top of that, the method used for the spectral index calculation is introduced.

3.5.1 Spectral Index Calculation

The calibrated data of the 14 mm and 7 mm receivers consist of flux density values for the frequency sub-bands 19.25 GHz, 21.15 GHz, 22.85 GHz, 24.75 GHz (14 mm) and

36.25 GHz, 38.75 GHz, 41.25 GHz, 43.75 GHz (7 mm). An example of a calibrated source measurement at these frequencies is shown in Fig. 3.10. As established earlier, sometimes, there are two detections of a source per epoch, which means that there is more than one flux density value for the same frequency. This can be seen in the example presented in Fig. 3.10 (gray dots). In this case, the average flux density per frequency is calculated by taking the mean. If there is only one flux density value per frequency available, it is used as-is. The averaged values are depicted as blue dots in Fig. 3.10. The error is determined by Gaussian error propagation, since distinct scans are considered independent measurements. After this first averaging process, a spectral power-law fit is performed to the data for every source at every observed epoch, following Equation (2.2). This is done for all sources where at least four distinct sub-frequencies are detected with at least one at 14 mm and one at 7 mm, per epoch. The fit is performed using a Levenberg-Marquardt fitting algorithm (Moré, 1978) and the python package `lmfit`. Since the spectrum is expected to be flat ($\alpha \sim 0$), the spectral index is bounded to $|\alpha| < 1$. If a spectral index reaches the boundary after the fit, it is not used for the spectral index analysis in Sect. 4.2, since in most cases this suggests that there are outliers in the data. An exemplary fit of Mrk 501 on July 28, 2021 is presented in Fig. 3.10, which results in a spectral index $\alpha = -0.262 \pm 0.021$. This analysis is applied to the entire data set, wherever 14 mm and 7 mm data are available for the same epoch and source. The spectra of all sources obtained during the first ~ 1.2 years of the TELAMON program can be found in Appendix B.

3.5.2 Light Curves & Sub-band Averaging

In order to enhance the analysis and to present sensible light curves, the observed flux densities of every source and epoch are averaged for the 14 mm and 7 mm receivers. In some cases, not every of the four sub-bands of each receiver shows a significant source detection. This can be due to RFI, because the source is too weak at the highest frequencies, or due to background noise. Averaging over the sub-bands of each receiver will make it possible to compare all epochs with each other, even if a sub-band flux density value might be vacant. However, taking the mean or the weighted mean of all measured values does not suffice to ensure the comparability of epochs. If, e.g., a source was detected at 19.25 GHz and 21.15 GHz at Epoch A and at another Epoch B at 22.85 GHz and 24.75 GHz, taking the mean will shift the mean frequency of this average. Since the spectrum of the sample sources is in general not always flat ($S(\nu) \neq \text{const.}$), this could turn out to be problematic when comparing flux densities from two distinct epochs. Therefore, for each receiver (7 mm and 14 mm), at first a power-law spectral fit $S(\nu)$ is performed to the raw data, following Equation (2.2). Similar to Sect. 3.5.1, a

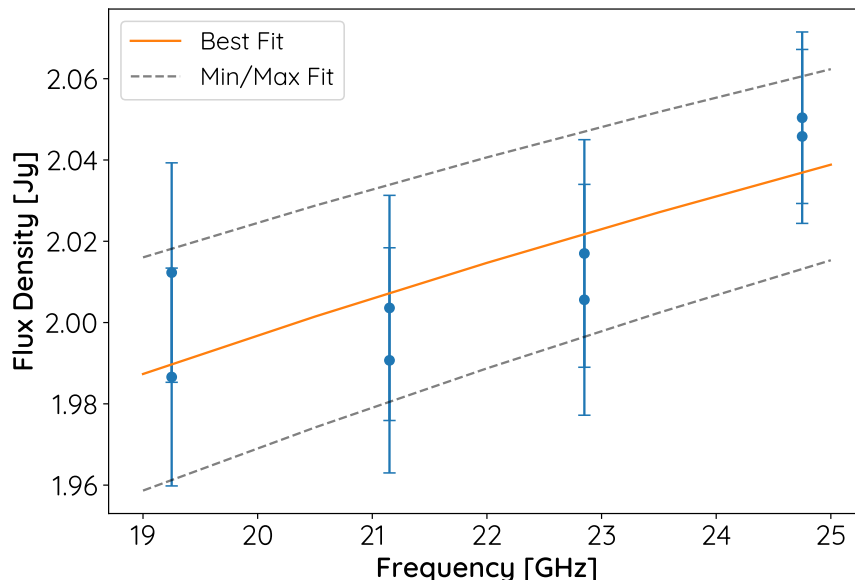


Fig. 3.11: Example of the sub-band averaging process (TXS 0506+056 on Jan 2, 2021 at 14 mm). The average flux density is calculated by taking the integral of the best fit between 19 GHz and 25 GHz. The errors are determined by integrating the Min/Max fits.

Levenberg-Marquart fitting algorithm is used to calculate the fit with the spectral index bounded to $|\alpha| < 0.5$. Note that here, the bound on α is even more conservative than for the spectral index calculation, since the analysis presented here is more sensitive to outliers. From the fit, the average flux density \bar{S} in the range of the receiver bandwidth is calculated:

$$\bar{S} = \frac{\int_{\nu_1}^{\nu_2} S(\nu) d\nu}{\nu_2 - \nu_1}. \quad (3.21)$$

For the 14 mm receiver, the integration limits are $\nu_1 = 19$ GHz and $\nu_2 = 25$ GHz, for the 7 mm receiver $\nu_1 = 36$ GHz and $\nu_2 = 44$ GHz. This method ensures that the average flux density is always calculated from the same frequency range, with best knowledge about the intrinsic spectrum of the source for each epoch. In the special case where only data for one sub-frequency (e.g., only for 19.25 GHz) are available, it is not possible to perform a sensible fit. In these cases, a flat spectrum ($\alpha = 0$) is assumed, since this is typical for the sources in the sample.

In order to define an error for the average flux density values, different approaches are used according to how many sub-bands are detected. In the case of two, three or four (i.e., all) sub-frequencies detected, two additional (error-)fits are performed. One with the errors subtracted from the measured flux density values and the other one with the errors added to the measured values. This is justified since in this case, the error mostly consists of systematic calibration uncertainty, i.e., the measured values may all together be higher (or lower) than the best values but relative to each other, they are known much more precisely. This procedure is illustrated in Fig. 3.11. The error is

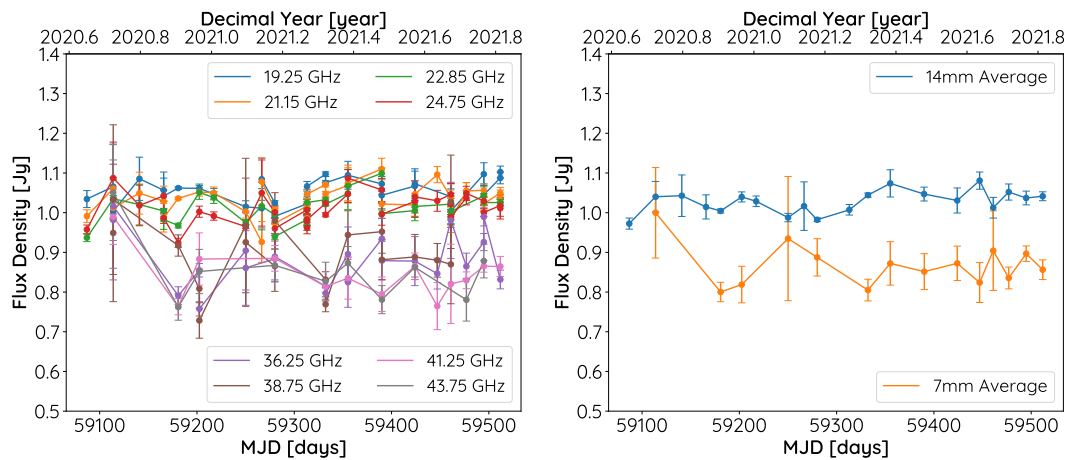


Fig. 3.12: Light curve of Mrk 501 with raw data (left) and sub-band-averaged data (right).

determined by the difference between min/max-fit and best fit. In the case of only one sub-frequency detected, this is vastly different, since no sensible fits can be performed. As stated earlier, the best value is therefore calculated by assuming a flat spectrum ($\alpha=0$). The uncertainty of this value is estimated in a similar manner to the min/max-fits mentioned earlier. Again, the measurement uncertainties are subtracted/added to the flux density value. Then, different spectral distributions with $\alpha \in \{-0.5; 0; 0.5\}$, originating at the min/max flux densities, are considered. This means, one gets three alternate spectral distributions for max and min flux density, respectively. Analogous to the previous calculations, the difference between the integrated alternate spectral distributions and the integrated best fit (in this case the flat spectrum) is calculated. The maximum difference is then used as the average flux density error.

The advantages of this sub-band averaging process become clear when looking at Fig. 3.12. On the left, one can see the raw data light curves. Every frequency describes a single light curve and it is very hard to characterize the source's behaviour. On the right, one can see the sub-band-averaged light curve, for the 14mm and 7mm receiver. In this representation, it is much easier to analyze the source variability and to identify flares.

In the following sections, when referring to flux densities at 7 mm and 14 mm, this always means the sub-band-averaged flux density in each band, calculated using the method introduced in this section. The sub-band averaged light curves of all sources obtained during the first ~ 1.2 years of the TELAMON program can be found in Appendix A.

Chapter 4

Results

In this section, the results of the TELAMON data analysis are reported. Variability properties and spectral indices of the sub-sample of HBLs and XBLs are presented. On top of that, a flare analysis is performed and variability Doppler factors are derived. The TELAMON data of the first ~ 1.2 years of the program from August 2020 to October 2021 (33 distinct epochs) at 14 mm and 7 mm are used to characterize the evolution of HBLs and XBLs, for the first time at multiple frequencies. All HBL and XBL objects from Table 3.1 are considered for the analysis. This leads to a total number of 30 sources, 18 of them being XBLs and 12 HBLs. Five of these sources (J0507+6737, J0658+0637, J0913-2103, J1428+4240, J1958-3011) were detected in less than three epochs and only at 14 mm. One source (J0955+3551) was not detected at all. Therefore, these sources are excluded from the presented analysis.

4.1 Light Curve Variability

4.1.1 Variability Measures

Characterizing the variability and flux density fluctuation of light curves is a non trivial process. There have been a lot of different approaches to variability studies in the past, through the variability index (e.g., [Aller et al., 1992](#)), the fluctuation index (e.g., [Aller et al., 2003](#)), the modulation index (e.g., [Kraus et al., 2003](#)), the fractional variability amplitude (e.g., [Edelson et al., 2002](#); [Soldi et al., 2008](#)), but also statistical tests of a null hypothesis of non-variability.

All of these tools allow for different analysis of the variability, but they all differ in terms of weighting and biases. Let us take as an example the variability index V of a light

curve, defined as

$$V = \frac{(S_{\max} - \sigma_{\max}) - (S_{\min} + \sigma_{\min})}{(S_{\max} - \sigma_{\max}) + (S_{\min} + \sigma_{\min})}, \quad (4.1)$$

with S_{\max} and S_{\min} being the maximum and minimum flux densities, respectively. σ_{\max} and σ_{\min} correspond to the errors of these two values. This index characterizes the variability of a source quite well if the source variability is much greater than the measurement uncertainties. Due to this, it might actually become negative if the uncertainties are large, compared to the flux density fluctuation. Moreover, this method is very sensitive to one-off flaring events which will lead to a high variability index even if the source is usually in a very stable state. Another important measure of variability is the modulation index

$$m_{\text{data}} = \frac{\sqrt{\frac{1}{N} \sum_{i=1}^N \left(S_i - \frac{1}{N} \sum_{i=1}^N S_i \right)^2}}{\frac{1}{N} \sum_{i=1}^N S_i}. \quad (4.2)$$

This can also be interpreted as the standard deviation of the flux density measurements divided by the average flux density. In contrast to the variability index V , this quantity is always positive and also more stable against one-off events like flares. However, the measurement uncertainties are still not accounted for in m_{data} . For example, if a source is quite faint and the flux density uncertainties are quite large, compared to the mean flux density, this will most likely result in a high modulation index, even if the source is actually quite stable within the measured uncertainties. Additionally, the quantity is still highly dependent on the sample size i.e., how many flux density measurements of a specific source are available.

In order to account for measurement uncertainties and to provide an uncertainty on the variability measure itself, [Richards et al. \(2011\)](#) have introduced the intrinsic modulation index

$$\bar{m} = \frac{\sigma_0}{S_0}. \quad (4.3)$$

Note that this is similar to the modulation index in Equation (4.2) but here, σ_0 represents the **intrinsic** standard deviation and S_0 is the **intrinsic** mean flux density of the source. The word intrinsic implies values that would be obtained if the observational uncertainties were non-existent and with an infinite sampling rate. Therefore, \bar{m} is a measure of the true (intrinsic) variability of the source.

4.1.2 Likelihood Approach to the Intrinsic Modulation Index

For the variability studies in this thesis, the intrinsic modulation index \bar{m} , as defined in Equation (4.3), is used. In order to calculate this intrinsic quantity, a likelihood approach is used, following [Richards et al. \(2011\)](#). It is assumed that the true flux densities for

each source are normally distributed with intrinsic mean flux density S_0 and intrinsic standard deviation σ_0 . Each light curve consists of N flux density measurements S_i , with an associated observational uncertainty σ_i . If a source has a true flux density of S_t at some time t , the probability to observe the flux density S_i at this time is given by

$$p(S_t, S_i, \sigma_i) = \frac{1}{\sigma_i \sqrt{2\pi}} \exp \left[-\frac{(S_t - S_i)^2}{2\sigma_i^2} \right], \quad (4.4)$$

where σ_i denotes the observational uncertainty. On the other hand, the probability that the source flux density at some time t is S_t , when the source flux density is normally distributed with intrinsic mean S_0 and intrinsic standard deviation σ_0 , is given by

$$p(S_t, S_0, \sigma_0) = \frac{1}{\sigma_0 \sqrt{2\pi}} \exp \left[-\frac{(S_t - S_0)^2}{2\sigma_0^2} \right]. \quad (4.5)$$

Combining these two probabilities, the total probability of observing a flux density S_i from a source with intrinsic mean flux density S_0 and intrinsic standard deviation σ_0 is

$$P_i = \int_{S_t} dS_t p(S_t, S_i, \sigma_i) p(S_t, S_0, \sigma_0) = \int_{S_t} dS_t \frac{\exp \left[-\frac{(S_t - S_i)^2}{2\sigma_i^2} \right]}{\sigma_i \sqrt{2\pi}} \frac{\exp \left[-\frac{(S_t - S_0)^2}{2\sigma_0^2} \right]}{\sigma_0 \sqrt{2\pi}} \quad (4.6)$$

This integral has an analytic solution if the limits $S_t \in]-\infty, \infty[$ are chosen (see, e.g., [Venters & Pavlidou \(2007\)](#)):

$$P_i = \frac{1}{\sqrt{2\pi(\sigma_0^2 + \sigma_i^2)}} \exp \left[-\frac{(S_i - S_0)^2}{2(\sigma_i^2 + \sigma_0^2)} \right]. \quad (4.7)$$

The likelihood of a certain light curve (equivalent to N measurements (S_i, σ_i)) can then be calculated by

$$\mathcal{L}(S_0, \sigma_0) = \prod_{i=1}^N P_i = \left(\prod_{i=1}^N \frac{1}{\sqrt{2\pi(\sigma_0^2 + \sigma_i^2)}} \right) \exp \left[-\frac{1}{2} \sum_{i=1}^N \frac{(S_i - S_0)^2}{\sigma_i^2 + \sigma_0^2} \right]. \quad (4.8)$$

On top of that, after using Equation (4.3) to substitute $\sigma_0 = \bar{m}S_0$, one finds

$$\mathcal{L}(S_0, \bar{m}) = S_0 \left(\prod_{i=1}^N \frac{1}{\sqrt{2\pi(\bar{m}^2 S_0^2 + \sigma_i^2)}} \right) \exp \left[-\frac{1}{2} \sum_{i=1}^N \frac{(S_i - S_0)^2}{\sigma_i^2 + \bar{m}^2 S_0^2} \right], \quad (4.9)$$

which only depends on the intrinsic source parameters S_0 and \bar{m} that need to be determined for every source. Note that $\mathcal{L}(S_0, \bar{m})$ is symmetric in \bar{m} and therefore guarantees non-negative modulation indices. In order to find the most likely values for the intrinsic source parameters S_0 and σ_0 , one needs to maximize the likelihood $\mathcal{L}(S_0, \bar{m})$, for every

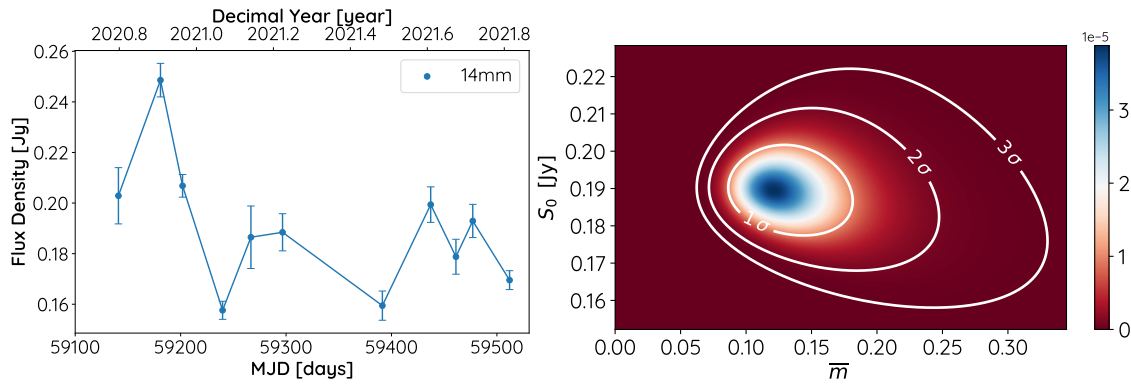


Fig. 4.1: Left: Light curve of the source J0303–2407 (averaged over all sub-bands); Right: Likelihood map of the 14 mm light curve of J0303–2407, used to determine the intrinsic modulation index. The color map corresponds to the likelihood $\mathcal{L}(S_0, \bar{m})$ of each (S_0, \bar{m}) combination for this light curve. The contour lines correspond to the $1\sigma, 2\sigma$ and 3σ uncertainty regions.

light curve. An example of this maximum likelihood analysis is presented in Fig. 4.1. On the right hand side, one can see the likelihood map $\mathcal{L}(S_0, \bar{m})$ for the 14 mm light curve of J0303–2407. From this likelihood map, estimates of S_0 and \bar{m} can be derived. The 1σ , 2σ and 3σ iso-likelihood contours contain 68.26 %, 95.45 % and 99.73 % of the total likelihood, respectively. In order to derive the most likely value of the intrinsic modulation index \bar{m} , independent of S_0 , one can sum over all S_0 values. This results in a one-dimensional likelihood distribution $\mathcal{L}(\bar{m})$ instead of the likelihood map. The value \bar{m} that maximizes $\mathcal{L}(\bar{m})$ is the most likely value for \bar{m} . In order to determine its error the iso-likelihood values \bar{m}_1 and \bar{m}_2 are calculated, for which

$$\mathcal{L}(\bar{m}_1) = \mathcal{L}(\bar{m}_2) \quad (4.10)$$

and

$$\frac{\int_{\bar{m}_1}^{\bar{m}_2} \mathcal{L}(\bar{m}) d\bar{m}}{\int_0^{\infty} \mathcal{L}(\bar{m}) d\bar{m}} = 68.26 \%. \quad (4.11)$$

This procedure can also be used to determine the 2σ and 3σ uncertainties and will usually lead to asymmetric errors, as can be seen in Table 4.1. Similar to Richards et al. (2011), statistically significant variability is only established if the maximum likelihood is more than 3σ away from $\bar{m} = 0$.

4.1.3 Intrinsic Modulation Indices of HBL and Extreme Blazars

The likelihood approach explained above has been applied to the sub-band averaged 14 mm and 7 mm light curves of HBLs and XBLs from the TELAMON sample, in order to determine their intrinsic modulation indices at these wavelengths. All results are presented in Table 4.1. Four sources (J0035+5950, J1058+2817, J1518-2731, J2243+2021)

Table 4.1: Intrinsic modulation indices of HBL and XBL sources from the TELAMON sample at 14 mm ($\overline{m}_{14\text{ mm}}$) and 7 mm ($\overline{m}_{7\text{ mm}}$). For the sources where no modulation index is presented, there were not enough lightcurve data available to calculate the modulation index.

Source	Alt Name	$\overline{m}_{14\text{ mm}}$	$\overline{m}_{7\text{ mm}}$
J0035+5950*	1ES 0033+595	$0.050^{+0.036}_{-0.027}$	-
J0214+5144	TXS 0210+515	$0.137^{+0.052}_{-0.033}$	-
J0222+4302	3C 66A	$0.054^{+0.014}_{-0.010}$	$0.151^{+0.051}_{-0.034}$
J0232+2017	1ES 0229+200	$0.377^{+0.168}_{-0.104}$	-
J0303-2407	PKS 0301-243	$0.126^{+0.039}_{-0.026}$	-
J0416+0105	1ES 0414+009	$0.204^{+0.098}_{-0.059}$	-
J0507+6737	1ES 0502+675	-	-
J0509+0541	TXS 0506+056	$0.280^{+0.060}_{-0.044}$	$0.310^{+0.081}_{-0.057}$
J0650+2502	1ES 0647+250	$0.085^{+0.041}_{-0.026}$	-
J0658+0637	NVSS J065844+063711	-	-
J0913-2103	MRC 0910-208	-	-
J0955+3551	3HSP J095507.9+355101	-	-
J1015+4926	1ES 1011+496	$0.056^{+0.022}_{-0.016}$	-
J1058+2817*	GB6 J1058+2817	$0.040^{+0.031}_{-0.037}$	-
J1104+3812	Mrk 421	$0.114^{+0.020}_{-0.016}$	$0.143^{+0.040}_{-0.029}$
J1136+7009	Mrk 180	$0.081^{+0.030}_{-0.020}$	-
J1217+3007	ON 325	$0.128^{+0.033}_{-0.023}$	$0.175^{+0.056}_{-0.038}$
J1221+3010	1ES 1218+304	$0.216^{+0.113}_{-0.065}$	-
J1427+2348	OQ 240	$0.050^{+0.013}_{-0.010}$	$0.136^{+0.061}_{-0.039}$
J1428+4240	1ES 1426+428	-	-
J1518-2731*	TXS 1515-273	$0.066^{+0.074}_{-0.033}$	-
J1555+1111	PG 1553+113	$0.093^{+0.019}_{-0.014}$	$0.156^{+0.110}_{-0.062}$
J1653+3945	Mrk 501	$0.024^{+0.006}_{-0.005}$	$0.030^{+0.018}_{-0.015}$
J1728+5013	I Zw 187	$0.088^{+0.020}_{-0.015}$	-
J1743+1935	1ES 1741+196	$0.084^{+0.018}_{-0.014}$	-
J1958-3011	1RXS J195815.6-301110	-	-
J1959+6508	1ES 1959+650	$0.070^{+0.019}_{-0.014}$	-
J2158-3013	PKS 2155-304	$0.138^{+0.079}_{-0.046}$	-
J2243+2021*	RGB J2243+203	$0.077^{+0.064}_{-0.034}$	-
J2347+5142	1ES 2344+514	$0.050^{+0.015}_{-0.011}$	-

* For these sources no significant variability could be established (i.e., $\overline{m}=0$ within $3\text{-}\sigma$ uncertainty region)

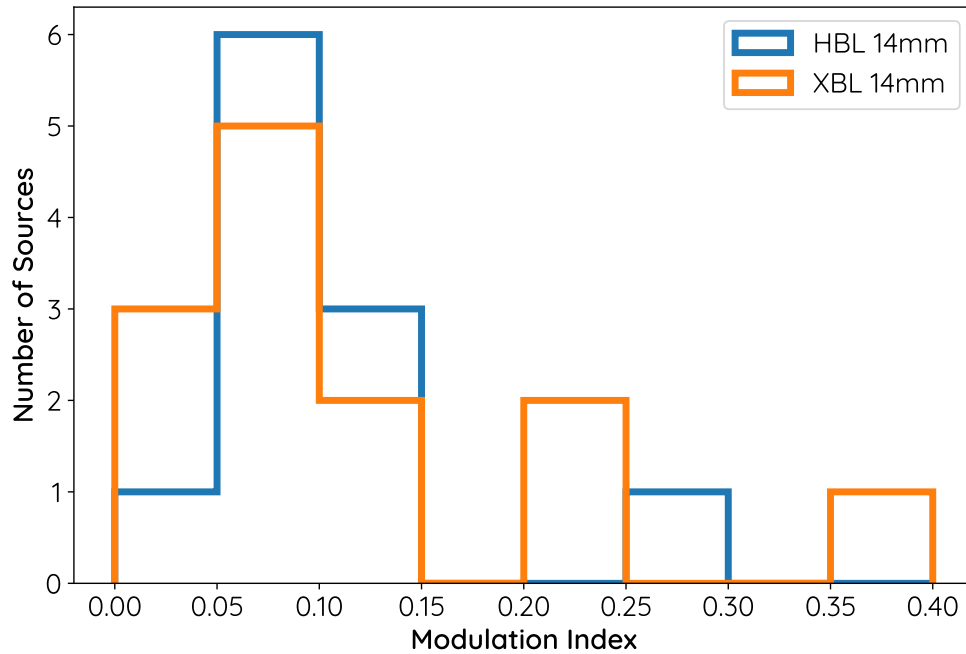


Fig. 4.2: Histogram of the intrinsic modulation index for TELAMON monitored HBL and XBL at 14 mm.

exhibit 3σ uncertainty regions of the modulation index including zero, which means that no significant variability can be established. All other sources with sufficient sampling (i.e., > 2 observations) are variable with a significance of more than 3σ . Still, modulation indices of all sources with sufficient sampling are presented here, in order to ensure completeness of the sample. Excluding the four sources which are not significantly variable would bias the analysis on significantly variable sources. The average modulation index at 14 mm, calculated from 24 individual sources, is 0.112 with a maximum of 0.377 and a minimum of 0.024. Assuming a Gaussian distribution, the standard deviation is 0.082. The average error on the values is 0.037, with a maximum error of 0.17. The average modulation index at 7 mm, calculated from seven individual sources is 0.158, with a maximum of 0.31 and a minimum of 0.030. Assuming a Gaussian distribution, the standard deviation is 0.078. The average error on the values is 0.049 with a maximum error of 0.10. Note that the number of derived modulation indices at 7 mm ($n=7$) is much smaller than at 14 mm ($n=24$) since most of the sources are faint and therefore challenging to detect at higher frequencies. In order to characterize HBLs and XBLs and to analyze possible differences, their intrinsic modulation index distributions at 14 mm are plotted in Fig. 4.2. The sample sizes of HBL ($n=11$) and XBL ($n=13$) are very similar and can therefore be compared well. In Fig. 4.2 both distributions look very similar, with the exception that three Extreme Blazars (J0232+2017, J0416+0105, J1217+3007) show comparably large modulation indices $\bar{m} > 0.2$, while only one HBL (J0509+0541) shows a modulation index $\bar{m} > 0.2$. The high modulation indices that the three XBLs

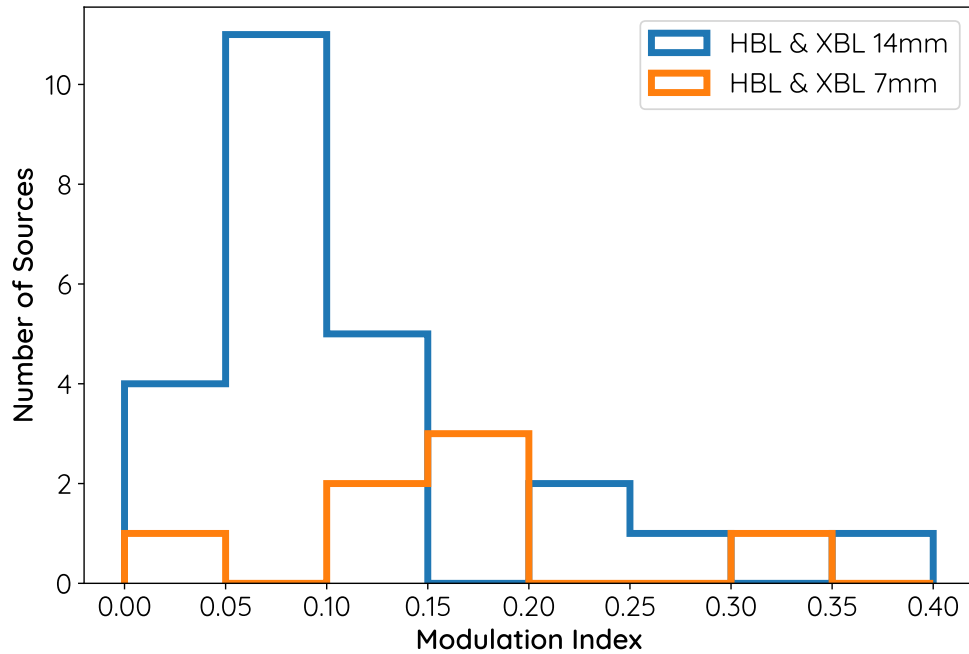


Fig. 4.3: Histogram of the intrinsic modulation index for TELAMON monitored HBL and XBL compared at 14 mm and 7 mm.

exhibit can be explained by flaring episodes (see Sect. 4.3.2), that have a big impact on the modulation index during the relatively short campaign time of ~ 1.2 years. The highly variable HBL, J0509+0541, shows a steady decline in flux density throughout the program which leads to the comparably high modulation index. In order to test if both samples (HBL & XBL) are statistically different from each other, a Kolmogorov-Smirnov test (KS-test) is performed. The KS-test leads to a p -value of $p = 0.99$, indicating that a statistical difference of both distributions cannot be established. It is therefore assumed that at 14 mm wavelengths, HBLs and XBLs cannot be distinguished by their intrinsic modulation index distribution. For the following analysis, the modulation indices of HBLs and XBLs are therefore combined and treated as a single sample of HBL/XBL.

The limited sample size at 7 mm makes it hard to draw significant conclusions from comparing 14 mm and 7 mm modulation indices, nevertheless, the modulation indices for HBLs & XBLs at 14 mm and 7 mm are compared in Fig. 4.3. It is evident that the modulation indices at 7 mm seem to be shifted upwards, compared to 14 mm, meaning that the sources are more variable at higher frequencies. This is also the case for all seven individual sources, where modulation indices both at 14 mm and 7 mm could be derived. For every single source, one finds $\bar{m}_{7\text{mm}} > \bar{m}_{14\text{mm}}$. A KS-test ($p = 0.022$) indicates that it is very unlikely that both distributions have the same underlying statistics, supporting the first visual impression. The significance of this result is very limited, due to the limited number of detections at 7 mm. For further discussion of this, see Sect. 5.1.

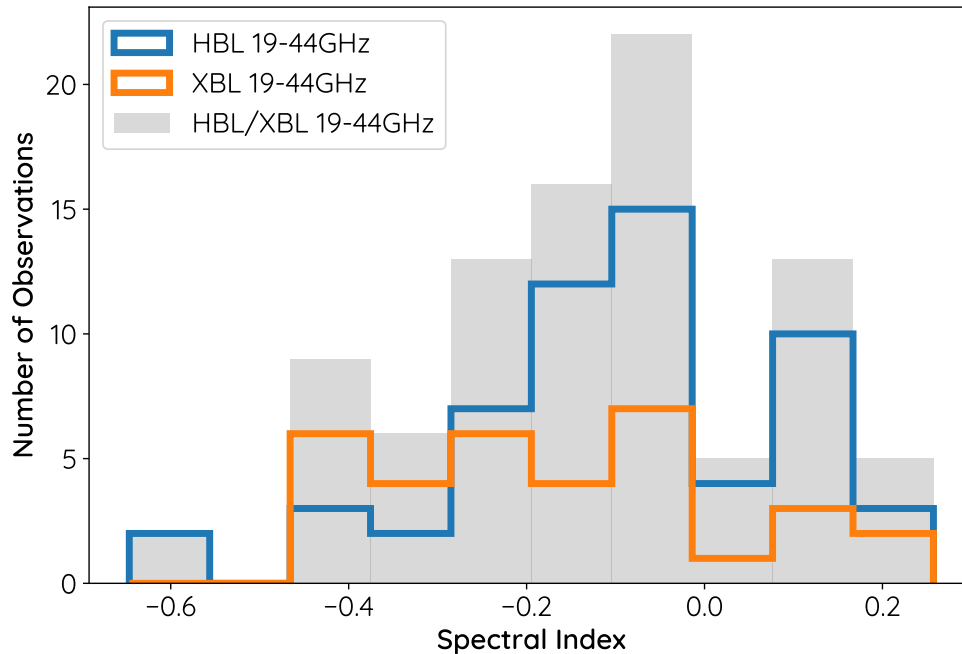


Fig. 4.4: Spectral index distribution of HBLs and XBLs in the TELAMON sample throughout the first 1.2 years. The blue bars represent HBLs, the orange bars represent XBLs. For the data presented here, 14 mm and 7 mm flux densities (19 GHz-44 GHz) are used to fit a power-law spectrum to determine the spectral index, as described in Sect. 3.5.1.

4.2 Spectral Indices of HBL and Extreme Blazars

Since most of the sources in the TELAMON HBL/XBL sample are relatively faint, and therefore challenging to detect at 7 mm, one can only derive spectral indices as described in Sect. 3.5.1 for six HBL sources (J0222+4302, J0509+0541, J1015+4926, J1217+3007, J1427+2348, J1555+1111) and four XBLs (J0214+5144, J1104+3812, J1653+3945, J1959+6508). Three of these ten sources (J1015+4926, J0214+5144, J1959+6508) have very limited 7 mm data available, which means that spectral indices can only be derived for less than 3 epochs. For the remaining seven sources, spectral indices for at least six distinct epochs could be derived, leading to a total number of 86 individual spectral index measurements. The spectral indices for all sources and epochs are presented in a histogram plot in Fig. 4.4 and in Table E.1 in Appendix E. On the first look, the distributions of HBLs and XBLs spectral indices seem to differ, therefore a KS-test is performed to see if this can be quantified. The KS-test finds a p -value of $p = 0.078$, which means one cannot conclude that both distributions are different. This conclusion is however not very significant due to the limited sample sizes which is also reflected in the low p -value. The XBL distribution is mainly driven by only two sources (J1104+3812 & J1653+3945), while the HBL sample is mainly driven by four sources (J0222+4302, J0509+0541, J1217+3007, J1427+2348). It is assumed that these limited number of sources are not representative for either sub-sample. This fact will also not improve

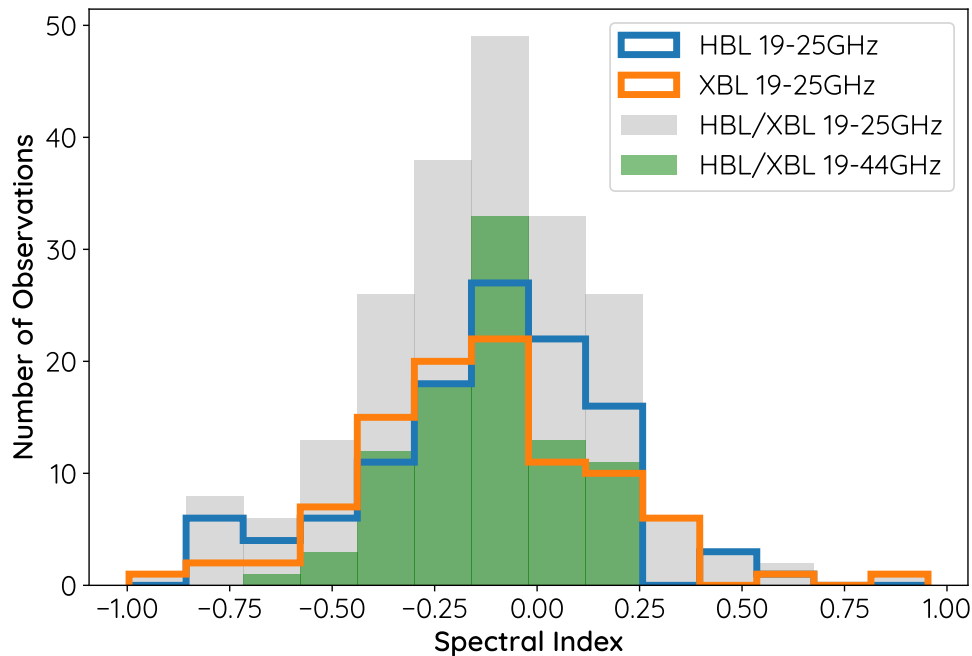


Fig. 4.5: Spectral index distribution of HBLs and XBLs in the TELAMON sample throughout the first 1.2 years. The blue bars represent HBLs, the orange bars represent XBLs. For the data presented here, only 14 mm data (19 GHz–25 GHz) are used to fit a power-law spectrum to determine the spectral index. For comparison the distribution of HBLs/XBLs considering 14 mm and 7 mm data (19 GHz–44 GHz) from Fig. 4.4 is shown in green.

significantly with longer monitoring periods, since most HBL and XBL are simply too faint at 7 mm to be detectable.

In order to improve the sample size, an additional spectral index calculation was performed, this time by only using data from the 14 mm receiver (4 sub-bands: 19.25 GHz, 21.15 GHz, 22.85 GHz, 24.75 GHz), but otherwise analogous to Sect. 3.5.1. The spectral index was only calculated if a source was detected in all four sub-bands. This analysis greatly improves the sample size to 11 HBL sources and 11 Extreme Blazars where spectral indices could be derived for at least one epoch. The derived spectral indices for HBL, XBL and both combined are presented in Fig. 4.5, together with the previously presented HBL/XBL spectral indices from 19 GHz–44 GHz. First, it needs to be tested if the spectral index calculation in the reduced frequency span of 19 GHz–25 GHz is representative for the spectral index calculation in the frequency span used before (19 GHz–44 GHz). In order to test this, multiple KS-tests were performed comparing the spectral index distributions calculated from 19 GHz–25 GHz and 19 GHz–44 GHz for XBL ($p = 0.64$), HBL ($p = 0.29$) and the combined sample of HBL/XBL ($p = 0.43$). All of these tests indicate that the use of 14 mm data only, to calculate the spectral indices is indeed a sensible way to improve the sample size. If the statistical coincidence of HBL and XBL sources is compared now, a p -value of $p = 0.19$ is found, as

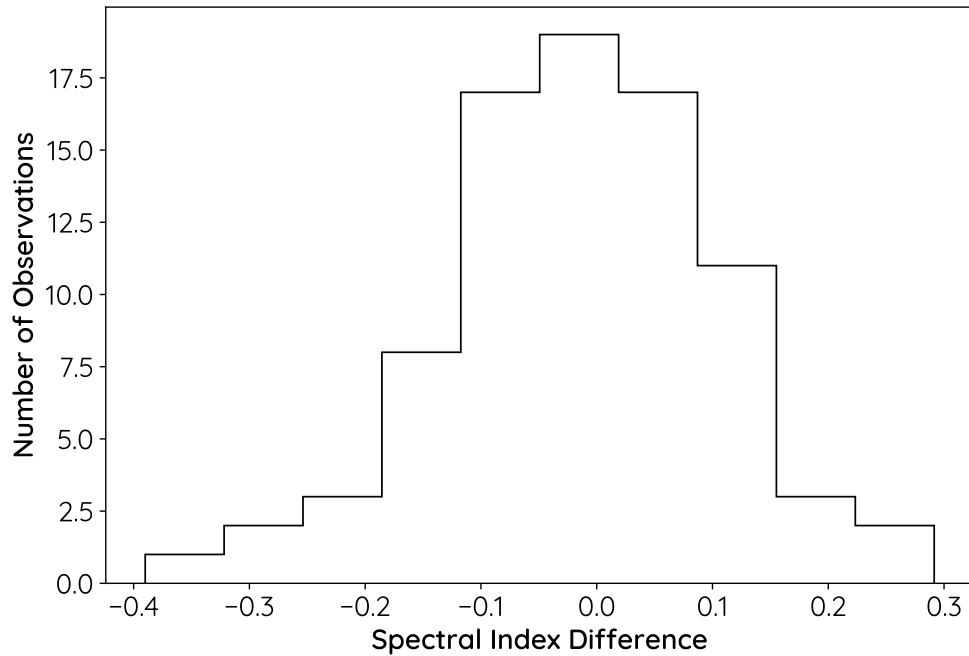


Fig. 4.6: Histogram of the difference between individual spectral indices calculated from 19 GHz–44 GHz and 19 GHz–25 GHz. The average difference is -0.01 while the standard deviation is 0.12 .

compared to $p = 0.078$ earlier, when using the limited sample of spectral indices from 19 GHz–44 GHz. This makes the rejection of the null-hypothesis of different distributions for HBL and XBL sources even more significant. As suspected, the lower p -value of $p = 0.078$ was mainly driven by only two sources in the XBL sample which seem to not be representative for the entire sample of XBLs. This means that, analogous to the intrinsic modulation index discussed in Sect. 4.1.3, HBL and XBL can also not be distinguished from each other based on their spectral index evolution and distribution.

To further justify the use of 14 mm spectral indices in favor of the larger sample size, the spectral indices themselves can be compared. For each individual spectral index calculated from 19 GHz–44 GHz one can also derive a spectral index using only the 19 GHz–25 GHz data. These two spectral indices are compared for all available measurements by calculating the difference of each pair, to see if they differ significantly or in a systematic fashion. If the 19 GHz–25 GHz spectral indices are representative for the 19 GHz–44 GHz spectral indices, one would expect a Gaussian distribution around zero. The distribution of the difference between spectral indices calculated from 19 GHz–25 GHz and 19 GHz–44 GHz is displayed in Fig. 4.6. The distribution is centered around zero with a mean value of -0.01 and a standard deviation of 0.12 . A Shapiro-Wilk-test (Shapiro & Wilk, 1965) confirms the normal distribution with a p -value of $p = 0.75$. This provides another argument, favoring the 19 GHz–25 GHz spectral indices, since they mostly coincide with the values calculated from 19 GHz–44 GHz. The

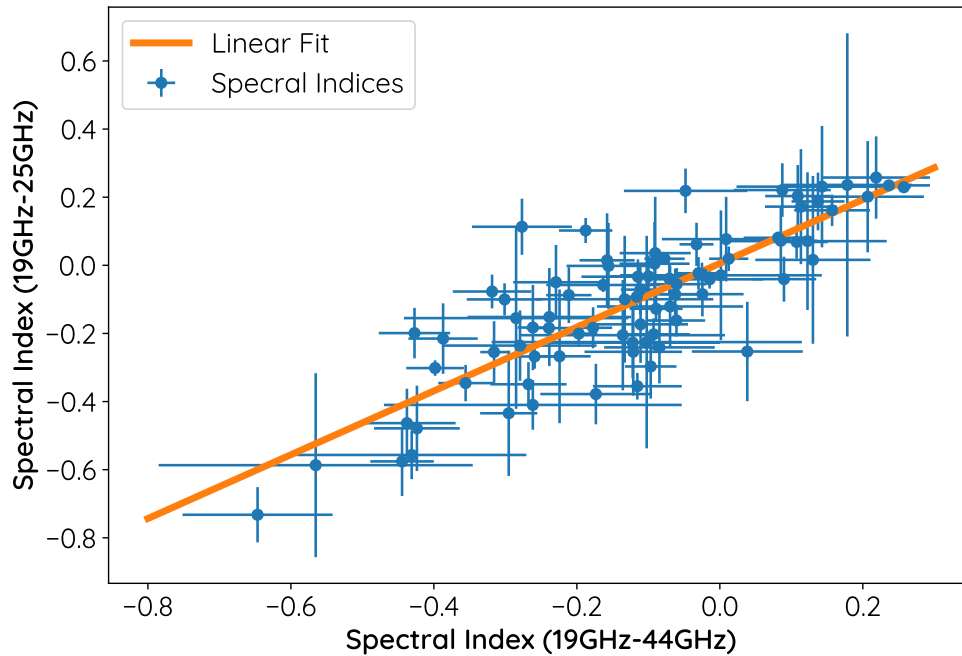


Fig. 4.7: Scatter plot of all observations where spectral indices were derived from 19GHz–25GHz and from 19GHz–44GHz. A linear fit has been performed to the data (orange).

standard deviation of 0.12 is smaller than the average error of the spectral indices from 19 GHz–25 GHz, which is 0.23. Compared to the average error of spectral indices from 19 GHz–44 GHz, which is 0.067, this is quite large. The large error of 0.23 is, however, overestimated due to the Levenberg-Marquardt fitting process, which takes into account the mostly systematic flux density errors within the 14 mm band. The statistical error of the spectral indices from 19 GHz–25 GHz should therefore be smaller which is also supported by the standard deviation of 0.12 of the difference distribution.

In order to verify this, the spectral indices derived from 19 GHz–25 GHz are plotted against the spectral indices from 19 GHz–44 GHz in Fig. 4.7. A linear fit leads to a slope of 0.936 ± 0.071 and $y_0 = 0.006 \pm 0.016$ with a reduced $\chi^2 \approx 0.015$. This also clearly indicates that the spectral indices derived from 19 GHz–25 GHz are representative for the spectral indices from 19 GHz–44 GHz. Although the individual errors on the spectral index values are smaller for 19 GHz–44 GHz, the spectral indices from 19 GHz–25 GHz are much more useful for statistical analysis due to their larger sample size, which increases the significance of these kind of analysis drastically. Therefore, in the following, only the 19 GHz–25 GHz spectral indices are discussed. On top of that, since one cannot statistically distinguish between HBLs and XBLs, both distributions are combined to a single HBL/XBL sample that will be compared with other publications in Sect. 5.2.

4.3 Flare Analysis

On top of the long-term light curve variability analyzed in Sect. 4.1.3, Blazars typically exhibit flaring episodes that can last from several minutes to days or even years (Romero et al., 2017). Especially Extreme Blazars can show fast variations in their flux density and spectrum (Biteau et al., 2020). In this section, possible flaring states found in the TELAMON HBL/XBL sample are analyzed and associated variability brightness temperatures and variability Doppler factors are calculated.

4.3.1 Flare Detection

The detection of flaring states and their timescales is a highly non-trivial process. In the literature, several methods are used to detect such flares (e.g., Singh & Meintjes, 2020). Due to the very limited sampling rate in the TELAMON data, a sensible flare analysis is very difficult. Especially for HBLs and XBLs, there are not enough 7 mm data available to perform a flare analysis at this wavelength. The 14 mm data are also very sparse but compared to the 7 mm coverage, clearly better. Analogous to the analysis of the intrinsic modulation coefficients in Sect. 4.1.3, the flare analysis will therefore be carried out only for the 14 mm data. As already mentioned, an automated statistical flare analysis with this kind of limited data points is not sensible, therefore a manual flare analysis is performed. For every source, all flux density values that are significantly higher than one sigma above the average flux density of the source are pre-flagged as possible flaring states. The light curves with pre-flagged flaring states are then inspected manually to see if an actual flare can be identified. This method is sensitive to human errors, but with the given data it is still considered to be the most efficient approach. Following this method, one finds nine flares in the TELAMON HBL/XBL sample during the first 1.2 years. The identified flares are highlighted in the light curves in Appendix A. Eight of these flares come from the sample of XBLs, while only one flare (J0303-2407) was detected in the HBL sample. Since the total number of HBLs in the sample ($n=12$) is similar to the number of XBLs in the sample ($n=18$), this is quite remarkable. On top of that, six of the sources were not included in the flare analysis due to limited number of detections. This means, the total number of sources considered for the flare analysis comprises 13 XBLs and 11 HBLs. Using these numbers to calculate flare statistics leads to an average annual flare rate of ~ 0.076 per HBL source and ~ 0.5 per XBL source. The annual flare rate for the combined sample of HBL/XBL is ~ 0.3 . These flare rates are subject to high uncertainties due to the limited data available, but they clearly indicate that XBLs seem to flare much more frequently than regular HBL sources.

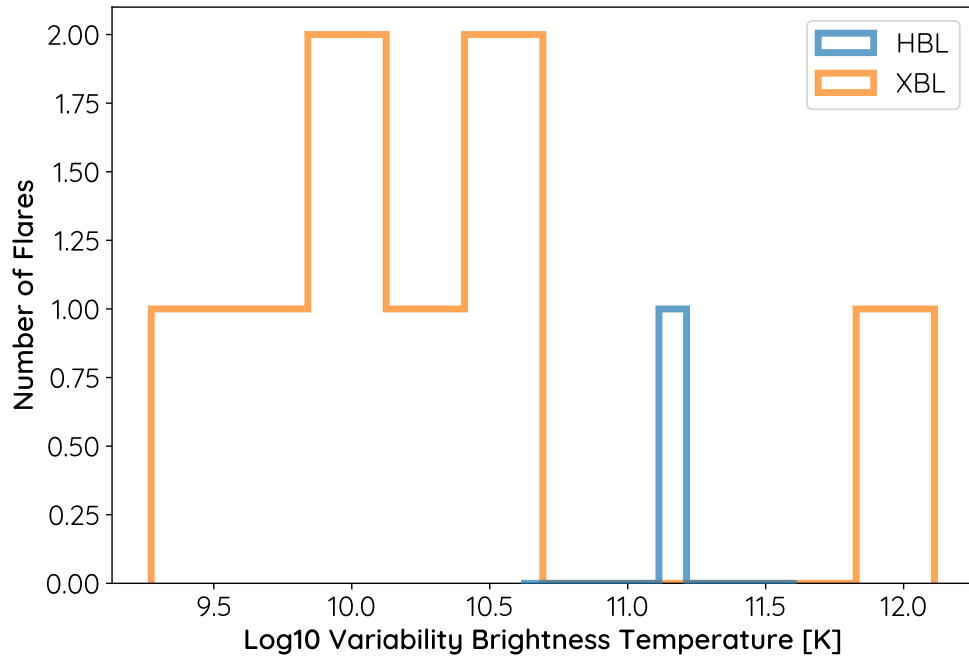


Fig. 4.8: Histogram plot of the variability brightness temperatures derived from the nine flares found in the TELAMON XBL/HBL dataset. Eight flares come from the sample of XBL (orange), while only one flare is attributed to the sample of HBL (blue).

In order to analyze the flares in detail, the rise time and flare amplitude were estimated using flux density measurements that were identified as start point and peak point of the flare. The identified start and end points of the flares are highlighted in the light curve plots in Appendix A. This method is subject to large errors due to the under-sampled light curves, but other methods, i.e., exponential fits were not possible for the same reason, either. The determined flare rise times are therefore treated as upper limits of the actual rise time, and the flare amplitudes are treated as lower limits of the actual flare amplitude. The variability brightness temperatures and variability Doppler factors derived later are therefore lower limits to the actual values. For every flare, the associated variability brightness temperature T_{var} has been calculated, similar to the studies by [Liodakis et al. \(2017\)](#) and [Fuhrmann et al. \(2016\)](#). This is done by using the relation

$$T_{\text{var}} = 1.47 \cdot 10^{13} \frac{D_{\text{L}}^2 \Delta S_{\text{flare}}(\nu)}{\nu^2 t_{\text{var}}^2 (1+z)^4}, \quad (4.12)$$

where D_{L} is the luminosity distance in Mpc, $\Delta S_{\text{flare}}(\nu)$ the flare amplitude in Jy, t_{var} the flare rise time in days, z the redshift and ν the observing frequency ([Blandford & Königl, 1979](#)). The luminosity distance D_{L} is calculated from the redshift using the relation $D_{\text{L}} = zc/H_0$, with the speed of light c and the Hubble Constant $H_0 = 72.8 \frac{\text{km/s}}{\text{Mpc}}$ from [Dhawan et al. \(2018\)](#). The variability brightness temperatures for the nine flares are displayed as a histogram plot in Fig. 4.8. One can see that the majority of flares from XBLs have comparably low variability brightness temperatures $< 10^{11}$ K, which is

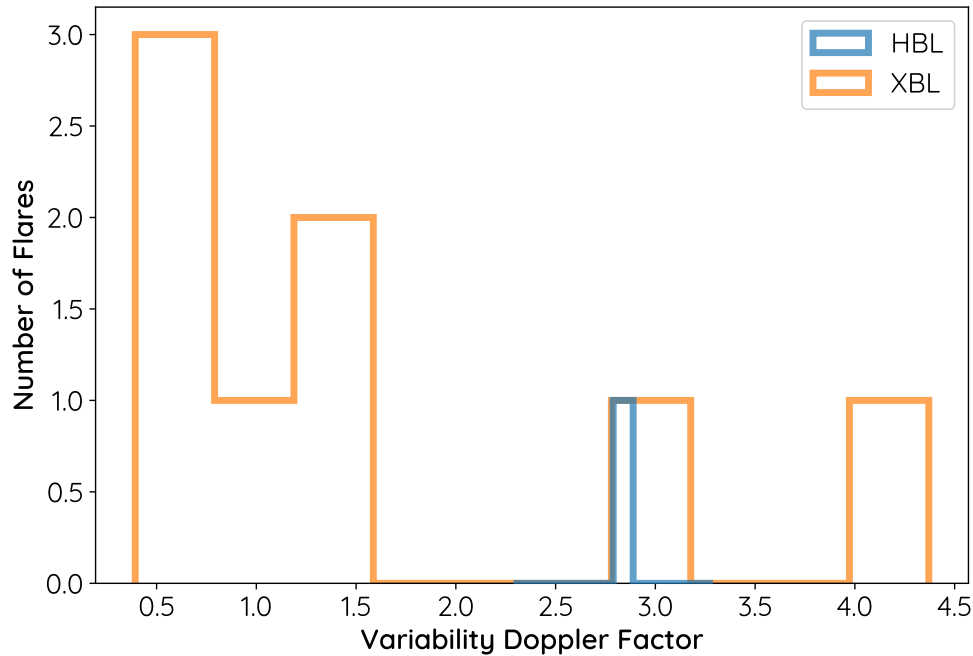


Fig. 4.9: Histogram plot of the variability Doppler factors derived from the nine flares found in the TELAMON XBL/HBL dataset.

indicative for smaller flares. In contrast, the variability brightness temperature of the only HBL flare is greater than the variability brightness temperature of seven of the XBL flares. Only one XBL flare exhibits a larger variability brightness temperature than the HBL flare. This could indicate that XBLs show frequent smaller flares ($T_{\text{var}} \lesssim 10^{11}$), but the flare rate of more significant major flares ($T_{\text{var}} \gtrsim 10^{11}$) is similar for HBL and XBL objects.

4.3.2 Variability Doppler Factors

If one assumes that sources reach equipartition while flaring, the intrinsic brightness temperature is equal to the equipartition brightness temperature $T_{\text{eq}} = 5 \cdot 10^{10}$ K (Readhead, 1994; Lahteenmaki et al., 1999). Therefore, the excess of observed brightness temperature compared to the intrinsic brightness temperature can be used to derive a variability Doppler factor

$$\delta_{\text{var}} = (1+z)^3 \sqrt[3]{\frac{T_{\text{var}}}{T_{\text{eq}}}}. \quad (4.13)$$

For a full derivation of Equation (4.13), it is referred to Appendix A in Liodakis et al. (2017). For all flares, the variability Doppler factor has been calculated and its distribution is shown in Fig. 4.9. Again, these values are to be treated as lower limits of the actual variability Doppler factor for the same reasons explained above. Here, a similar picture emerges as with the variability brightness temperatures. Most of the XBL

flares exhibit comparably low variability Doppler factors, only two flares have associated variability Doppler factors > 2.5 . The single HBL flare has a rather high associated variability Doppler factor of ~ 2.79 . These low variability Doppler factors found here are typical for sources affected by the Doppler crisis. For a more detailed discussion on this, see Sect. [5.3](#).

Chapter 5

Discussion

In this chapter, the results presented in Chap. 4 are compared with a similar study with a largely coincident sample by Lindfors et al. (2016) and with similar studies of lower peaked Blazars and FSRQs by the F-GAMMA program (Angelakis et al., 2019; Fuhrmann et al., 2016). On top of that, the variability Doppler factors derived from TELAMON flares are discussed in light of the Doppler crisis phenomenon.

5.1 Modulation Index

In addition to the TELAMON program, a previous study by Lindfors et al. (2016) has carried out a similar monitoring program of a largely coincident sample (19 overlapping HBL/XBL targets) using the OVRO Observatory for ~ 2.5 years, but with radio coverage only at 15 GHz. For their sources, they also calculated intrinsic modulation indices. The intrinsic modulation index distributions of both programs are depicted in Fig. 5.1. Both distributions look very similar, again, apart from the previously discussed flaring sources in the TELAMON data, that exhibit comparably high modulation indices. A KS-test with the null hypotheses of different underlying distributions leads to a rejection of the null hypotheses with high significance. This means, both distributions are likely the same or in other words, the TELAMON data presented in this thesis are consistent with Lindfors et al. (2016).

The mean value of intrinsic modulation indices presented by Lindfors et al. (2016) is 0.13, i.e., slightly higher than the one found in TELAMON data (0.11), but well within the TELAMON standard deviation of 0.082. Moreover, one should note that the Lindfors et al. (2016) data have smaller uncertainties (on average 0.01), compared to the TELAMON data (on average 0.037). This can be explained by the longer monitoring period

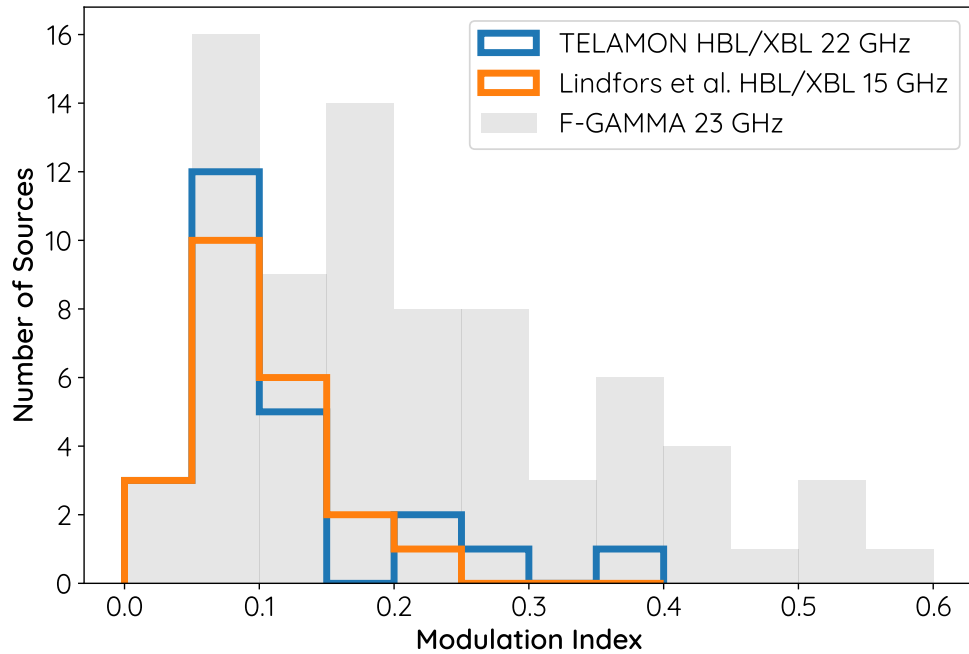


Fig. 5.1: Histogram of the intrinsic modulation index for TELAMON HBL and XBL sources at 14 mm (blue, centered at 22 GHz) compared to HBL and XBL data from Lindfors et al. (2016) at 15 GHz (orange). In the background (grey) one can see the intrinsic modulation index distribution of the F-GAMMA program at 23 GHz derived from data published by Angelakis et al. (2019).

of the Lindfors et al. (2016) program, producing more flux density measurements than are currently available from TELAMON. The deviation between the average intrinsic modulation indices is therefore probably of statistical nature. To further analyze this, one can compare the intrinsic modulation indices of the 19 sources that are monitored by both programs. For 12 of the sources, TELAMON data suggest smaller intrinsic modulation indices, for 7 of the sources, TELAMON data suggest larger intrinsic modulation indices. The larger modulation coefficients are mainly driven by flares, that have a huge impact on the modulation index considering the short monitoring time scale of only ~ 1.2 years. On the other hand, the absence of flares in some sources can also lead to under-estimation of the modulation index. It is expected that, with increasing TELAMON data over time, the deviation of TELAMON and Lindfors et al. (2016) modulation indices will become even smaller.

Apart from the OVRO monitoring by Lindfors et al. (2016), there have been other previous Blazar radio monitoring programs, e.g., the F-GAMMA program (Fuhrmann et al., 2016; Angelakis et al., 2019). In contrast to the two previously introduced studies, the F-GAMMA sample mostly consists of FSRQs and lower peaked Blazars, i.e., a very different sample, that can be used to find differences between FSRQs and HBLs/XBLs. For this purpose, F-GAMMA data from Angelakis et al. (2019) at 23.05 GHz were used

to calculate the intrinsic modulation indices for the F-GAMMA sample. Fuhrmann et al. (2016) also present their own variability studies at multiple frequencies, but since they are analyzing different frequencies and are not using the intrinsic modulation index, it was more convenient to derive the intrinsic modulation indices directly from the raw F-GAMMA data¹. This is again done using the maximum likelihood-approach explained in detail in Sect. 4.1.2. The intrinsic modulation index distribution of the F-GAMMA sample is plotted on top of the TELAMON and Lindfors et al. (2016) modulation indices in Fig. 5.1. Both HBL/XBL distributions look very different and again a KS-test is performed, to test if the TELAMON HBL/XBL intrinsic modulation indices and F-GAMMA modulation indices come from statistically distinct distributions. The KS-test leads to a p-value of $p = 5.2 \cdot 10^{-5}$, which indicates that both distributions are different, with very high significance. The modulation indices of F-GAMMA sources (FSRQs, LBLs) are scattered over a larger range (0–0.6) and exhibit larger modulation indices on average than HBL/XBL objects. This can be explained by three possible scenarios: 1. This is an intrinsic source property of HBL and XBL objects, which stands in contrast to the expected extreme variability of these objects (e.g., Biteau et al., 2020) - 2. Since most HBLs/XBLs are very faint sources, their relative flux density uncertainties are higher compared to brighter sources like FSRQs, which makes it more difficult to find variability and might lead to under-estimation of the modulation index. Note that this scenario could be tested with a selected sample of low luminosity Blazars including lower peaked BL Lacs and FSRQs. - 3. The available TELAMON data do show high modulation indices for some HBLs/XBLs where flares have been detected. The monitored time scale of ~ 1.2 years is not sufficient to observe flares in all HBL/XBL objects in the sample. Therefore, the modulation indices of a few flaring sources are over estimated and the modulation indices of many non-flaring sources are under-estimated. With increasing TELAMON data over time, one will be able to tell, what the favored scenario out of these three is. More sensitive observations of HBLs and XBLs, e.g., with VLBI, can also help to investigate if the telescope sensitivity is really a factor here, as suggested in scenario 2. Note that the use of the intrinsic modulation index in the presented analysis has a lot of advantages, but might also cause several problems. In order to calculate the intrinsic modulation coefficients it is assumed that the flux densities are distributed according to a Gauss distribution. In general, this does not always have to be true. Sometimes, Blazar variability is modelled by other distributions (e.g. log-normal), especially in the high-energy regime when investigating the duty cycle of Blazars (Sacahui et al., 2021). On top of that, the calculation of intrinsic modulation coefficients only takes into account the number of flux density measurements and not their sampling frequency. This means a less observed source with one flare detection might have a larger modulation index than a better sampled source with the same flare.

¹<https://cdsarc.cds.unistra.fr/viz-bin/cat/J/A+A/626/A60>

In Sect. 4.1.3, it was shown that variability at 7 mm seems to be stronger compared to 14 mm in the TELAMON data. Due to the limited sample size of the 7 mm modulation indices, it is hard to make conclusions about the significance of this trend. To check if this trend is reflected in a larger sample, the modulation indices at 43 GHz of the F-GAMMA data have been calculated, in addition to 23.05 GHz. Here, the trend is very significant: The mean modulation index at 23.05 GHz is 0.22 while the mean modulation index at 43 GHz is 0.30. A KS-test also suggests that both distributions are distinct, with a p-value of $p=0.0051$. In addition to that, for the very limited number of HBL/XBL sources in the F-GAMMA sample, one finds that all of them have higher variability at 43 GHz than at 23.05 GHz. Therefore, it is assumed that the trend, that TELAMON HBLs/XBLs are more variable at higher frequencies, is also real but a larger sample of HBLs/XBLs needs to be investigated at high frequencies in order to make significant conclusions about 7 mm variability of these sources.

5.2 Spectral Index

The TELAMON program allows for a characterization of the spectral indices of Extreme Blazars and HBL for the first time, as presented in Sect. 4.2. This presented analysis also allows for comparison with other source classes observed in previous studies like the F-GAMMA program which focused their observations on FSRQs and lower peaked BL Lac objects. Fuhrmann et al. (2016) present average spectral indices of their sample sources for different frequency ranges and also Angelakis et al. (2019) perform various analyses of the spectral index evolution of their sample. Most of their analysis steps require a significantly larger data sample than is currently available of TELAMON data, which makes it hard to directly compare their results with results found in this work. Therefore, the raw F-GAMMA light curve data from Angelakis et al. (2019) are used to determine spectral indices, for all their observing epochs and sources, using the analysis presented in Sect. 3.5.1. The F-GAMMA program covers a much larger frequency range (2.64 GHz–345 GHz) than the TELAMON program. For the calculation of F-GAMMA spectral indices only flux densities measured at 14.6 GHz, 23.05 GHz, 32 GHz and 43 GHz are considered, to ensure comparability with TELAMON measurements. These specific frequencies are selected, because they are closest to the TELAMON observing frequencies between 19 GHz and 44 GHz. The spectral index calculation is carried out for all sources from Fuhrmann et al. (2016), which are mainly FSRQs and (lower-peaked) BL Lacs, as indicated in their Table 1. The calculated spectral indices are presented as a histogram plot in Fig. 5.2. The gray data include the entire Fuhrmann et al. (2016) sample, while the red and blue lines represent the sub-sample of FSRQs and BL Lacs, respectively. For comparison, the TELAMON HBL/XBL spectral indices (19 GHz–25 GHz)

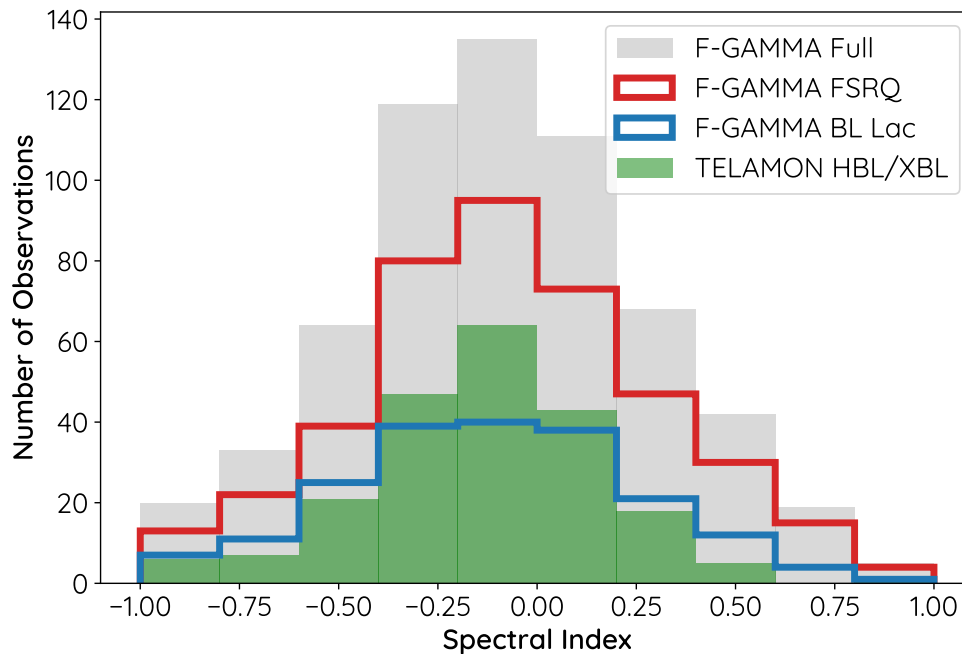


Fig. 5.2: Spectral index distribution of F-GAMMA sources calculated from the light curve data published in [Angelakis et al. \(2019\)](#). The red lines represent the distribution only for FSRQs, the blue line represent the distribution of only BL Lac objects in the F-GAMMA data. For comparison, the TELAMON HBL/XBL spectral indices (19 GHz-25 GHz) are plotted in green.

are shown in green. At first glance, all distributions look very similar, therefore multiple KS-tests are carried out to test, whether they have the same underlying statistical distribution. Comparing F-GAMMA BL Lac sources and TELAMON HBL/XBL leads to a p-value of $p = 0.29$, which means one cannot rule out that they are drawn from the same statistics. Things are very different when comparing the TELAMON HBL/XBL spectral index distribution to F-GAMMA FSRQs. Here, one finds a p-value of $p = 0.0049$, indicating that both distributions are statistically independent with very high significance. The same is true for the entire F-GAMMA sample compared to TELAMON HBL/XBL sources ($p = 0.011$). This trend can also be seen when looking at TELAMON data only. The TELAMON sample also includes six FSRQs which are statistically coincident with the F-GAMMA FSRQs ($p = 0.11$), but differ significantly from the TELAMON HBL/XBL sources ($p = 0.0061$). It is evident that HBLs/XBLs and FSRQs differ significantly from each other in their spectral index evolution, as well as in their light curve variability (see Sect. 5.1). But this only becomes clear in statistical analyses when looking at larger samples and not single, individual sources. It is hard to quantify this difference, but in terms of the spectral index, in Fig. 5.2 it is evident that HBLs/XBLs very rarely exhibit inverted spectra with spectral indices $\alpha > 0.25$, while FSRQs are much more likely to exhibit these kind of inverted spectra. This is also reflected in the average spectral index. For the TELAMON HBLs/XBLs one finds an average spectral

index over all sources and epochs of -0.13 , with a standard deviation of 0.29 , while for FSRQs in the F-GAMMA sample the average spectral index yields -0.07 , with a standard deviation of 0.37 . Note that the significance of these differences is unclear, but this might indicate that, as already discussed for modulation indices, FSRQs are more variable than HBL/XBL objects. Similar to Sect. 5.1, this is rather surprising due to the extreme nature of, especially, XBL objects, but could be explained by the three scenarios introduced in Sect. 5.1. This means, more data, also including flaring episodes of multiple HBL/XBL objects, are required to draw significant conclusions on this matter.

5.3 Flare Analysis

The variability brightness temperatures of FSRQs and BL Lacs have been analyzed in detail by many previous studies (e.g., Hovatta et al., 2009; Savolainen et al., 2010; Fuhrmann et al., 2016). In general, it was found that BL Lacs exhibit lower Doppler factors and variability brightness temperatures than FSRQs. In the study of Fuhrmann et al. (2016) it is presented that BL Lacs in their sample show comparably low variability Doppler factors throughout all frequencies, with many sources having variability Doppler factors in the range $0-2$. This is very similar to what has been found for the TELAMON HBL/XBL sample. All sources exhibit relatively low variability Doppler factors, with only two outliers with variability Doppler factors $\delta_{\text{var}} > 2$. In contrast to this, Savolainen et al. (2010) and Fuhrmann et al. (2016) found that the subclass of *Fermi*-detected sources shows slightly higher variability Doppler factors across all radio bands. Since all of the sources in the TELAMON sample are γ -ray detected, one would also expect to see this effect in the data presented in this thesis. It is difficult to tell if this trend is actually present in the data, since no direct comparison of non- γ -ray-detected sources with γ -ray detected sources solely from the TELAMON sample is possible. Note that the time ranges and total amount of data available in all studies referenced above is superior to the first year TELAMON data analyzed in this work. It is therefore expected that with increasing TELAMON observing time, there will be more stronger flares detected in the sample sources and therefore the lower limits to the actual variability Doppler factor presented in this work might increase with time. Due to this fact, it is currently not clear, if the TeV-detected sources in the TELAMON sample show similar or even higher variability Doppler factors than γ -ray detected sources analyzed by Fuhrmann et al. (2016) and Savolainen et al. (2010).

One should note that the low variability Doppler factors found in the TELAMON sample are quite typical for Blazars and are part of the Doppler crisis phenomenon introduced

in Sect. 2.4.3. Typically, explanation of the high-energy emission of Blazars involves very high Doppler factors, while in the radio regime significantly lower Doppler factors are detected. In order to identify if this is also the case for the sources at hand, the calculated variability Doppler factors and Doppler factors suggested by different SED-modelling studies are compared in Table 5.1. It becomes clear that for five sources, the Doppler factors required by SED-models are much larger than what has been found in the radio data. For the remaining four sources, no SED studies predicting limits on the Doppler factor were found, but it is very likely that similar high Doppler factors are required for modelling their SED. Even for the strongest radio flare (J0232+2017, $\delta_{\text{var}} = 4.4$) one finds $\delta_{\text{var}} \ll \delta_{\text{SED}}$. It is therefore expected that, even if some of the sources may exhibit stronger flares and therefore larger variability Doppler factors in the future, they may still not match the even higher Doppler factors predicted by SED studies. The Doppler crisis therefore remains unsolved and requires further investigation, e.g. with VLBI, especially during flaring episodes. This will help to test, e.g., for the scenario of a “spine-sheath” structure, where different Doppler factors are explained by different emitting regions, as introduced in Sect. 2.4.3. In that regard, the TELAMON program is very useful to detect such flares and trigger further observations with, e.g., VLBI.

Table 5.1: Lower limits to the Variability brightness temperatures and to the Doppler factors derived from flaring TELAMON sources. In addition to that, Doppler factors suggested by SED-modelling studies found in the literature are presented. For four of the sources, no SED studies predicting limits on the Doppler factor were found.

Source	T_{var} [K]	δ_{var}	δ_{SED}	δ_{SED}	Reference
J0214+5144	$8.6 \cdot 10^9$	0.64	-	-	-
J0232+2017	$1.3 \cdot 10^{12}$	4.4	> 40		Kaufmann et al. (2011)
J0303-2407	$1.3 \cdot 10^{11}$	2.8	~ 27		H. E. S. S. Collaboration et al. (2013)
J0416+0105	$9.3 \cdot 10^9$	1.2	> 50		H. E. S. S. Collaboration et al. (2012)
J1058+2817	$4.0 \cdot 10^{10}$	3.0	-	-	-
J1104+3812	$4.8 \cdot 10^9$	0.50	> 12		Abdo et al. (2011)
J1221+3010	$2.0 \cdot 10^{10}$	1.2	~ 20		Sato et al. (2008)
J1728+5013	$1.9 \cdot 10^9$	0.39	-	-	-
J2347+5142	$4.7 \cdot 10^{10}$	1.1	-	-	-

Chapter 6

Summary & Outlook

In this thesis, high frequency (19 GHz–44 GHz) radio data of the first ~ 1.2 years (August 2020 to October 2021) of the TELAMON program were used to characterize the variability properties of High-Peaked BL Lac objects and Extreme Blazars. The TELAMON program uses the Effelsberg 100-m telescope and is designed to track the evolution of TeV-detected Blazars with frequent (every 2–4 weeks) monitoring at multiple radio frequencies. These data were used to determine intrinsic modulation indices and spectral indices for all HBLs and XBLs in the sample with sufficient sampling. In terms of their intrinsic modulation index and spectral index evolution, HBLs and XBLs in the TELAMON sample do not show significant differences. A similar study of a largely coincident sample by Lindfors et al. (2016), using OVRO 15 GHz data, suggests a very similar intrinsic modulation index distribution as found in this thesis. Compared to a sample of low-peaked BL Lacs and FSRQs by the F-GAMMA program (Fuhrmann et al., 2016; Angelakis et al., 2019), HBLs and XBLs exhibit lower intrinsic modulation indices with a significantly different distribution. This means, sources from the F-GAMMA sample seem to be much more variable than HBLs and XBLs from the TELAMON sample. The same picture emerges when looking at the spectral index evolution. Here, the low-peaked BL Lacs and FSRQs from the F-GAMMA sample show a much broader distribution of spectral indices than found in TELAMON HBLs and XBLs. Especially inverted spectra with a spectral index $\alpha > 0.25$ are very rarely observed in the sample of HBLs and XBLs, while inverted spectra are not an uncommon finding in the F-GAMMA sample. Additionally, a manual flare analysis has been performed for the 14 mm light curves of the HBL and XBL sample. A total of nine flares were identified, while eight of them come from the sample of XBLs and only one flare was observed in an HBL source. Most of the flares show comparably low variability Doppler factors, which is typical for the phenomenon of the Doppler crisis. This means that these sources usually exhibit low Doppler factors in the radio regime while SED modelling of these sources requires

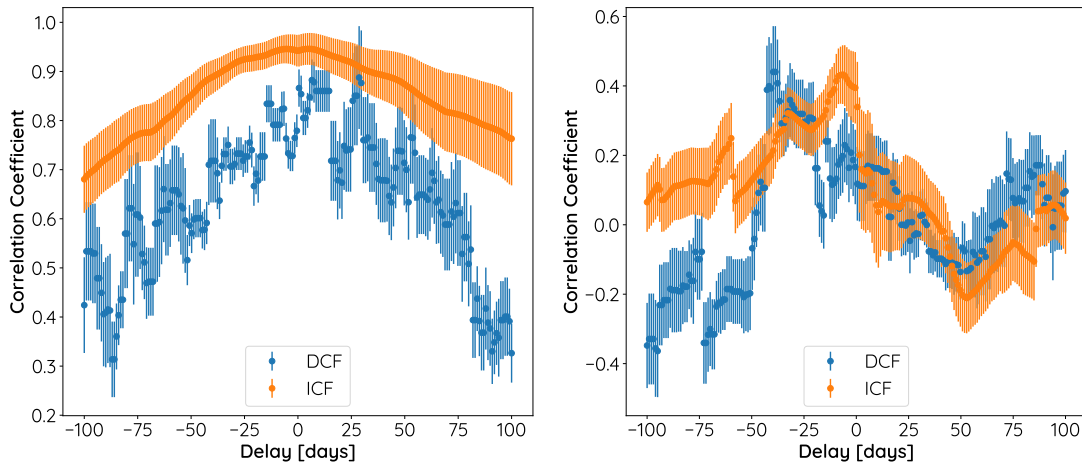


Fig. 6.1: Preliminary correlation analysis between 14 mm and 7 mm light curves of J0509+0541 (left) and J1104+3812 (right). For both sources the discrete correlation function (DCF) and interpolated correlation function (ICF) has been calculated.

very high Doppler factors. For all five flaring sources, where previous SED studies were found, this is also the case here. Future TELAMON monitoring will help to reveal, whether these sources show larger flares with higher associated Doppler factors in the future or if the Doppler crisis remains unsolved. The limited time range and sampling puts limits on the performed analysis, especially the 7 mm data are very sparse, due to the faintness of most HBLs and XBLs. More available TELAMON data in the future will allow for some other interesting studies, e.g., a correlation study between 7 mm and 14 mm radio emission or an analysis of the correlation of radio with VHE emission or possibly neutrino emission. Considering the TELAMON HBL/XBL annual flare rate of 0.3 and the average flare rise time of ~ 75 days, as a rough estimate one expects up to ~ 0.03 HBL/XBL flares per year, timely and spatially (90% containment region) coincident with IceCube Bronze/Gold neutrino track alerts. In the case of a strong correlation between HBL flares and neutrino emission this number is expected to be much higher, which can be revealed by the TELAMON program following up neutrino track alerts. Moreover, in the light of the upcoming Cherenkov Telescope Array (Cherenkov Telescope Array Consortium et al., 2019), the TeV-emitting sources presented in this thesis will become very relevant and joint TeV-radio studies will be possible with the help of TELAMON data. A preliminary correlation analysis of 14 mm and 7 mm data has already been tested (see Fig. 6.1), using the discrete correlation function (DCF, Edelson & Krolik, 1988; Peterson et al., 1998) and the interpolated correlation function (ICF, White & Peterson, 1994). In Fig. 6.1 one can see that for some sources, e.g., J0509+0541, one can already see a clear correlation in DCF and ICF, but it becomes clear that the limited time range still limits such analysis. In both plots presented here, the DCF and ICF suggest quite different correlation values, especially at higher absolute delay times, which is indicative of short and under-sampled light curves. This is

expected to drastically improve with time as more TELAMON data are being accumulated. On top of that, since spring 2021, the 20 mm receiver of the Effelsberg telescope has been added to the program, which helps to increase the radio coverage, e.g. during bad weather sessions. The same analysis presented in this thesis can also be carried out for the 20 mm data as soon as enough data are available from this band. It will be interesting to see how the 20 mm data compare with the 14 mm and 7 mm data presented in this work.

Bibliography

- Abazajian K. N., et al., 2009, *ApJS*, 182, 543
- Abdo A. A., et al., 2010, *ApJ*, 716, 30
- Abdo A. A., et al., 2011, *ApJ*, 736, 131
- Abdollahi S., et al., 2020, *ApJS*, 247, 33
- Ackermann M., et al., 2015, *ApJ*, 810, 14
- Aharonian F., et al., 2007, *A&A*, 475, L9
- Ahn C. P., et al., 2012, *ApJS*, 203, 21
- Ahnen M. L., et al., 2017, *A&A*, 603, A25
- Aller M. F., Aller H. D., Hughes P. A., 1992, *ApJ*, 399, 16
- Aller M. F., Aller H. D., Hughes P. A., 2003, *ApJ*, 586, 33
- Angelakis E., et al., 2019, *A&A*, 626, A60
- Antonucci R., 1993, *ARA&A*, 31, 473
- Baars J. W. M., Genzel R., Pauliny-Toth I. I. K., Witzel A., 1977, *A&A*, 500, 135
- Bach U., Kraus A., 2018, Effelsberg Radio Observatory 2017–2018 Biennial Report. In International VLBI Service for Geodesy and Astrometry 2017+2018 Biennial Report, edited by K. L. Armstrong, K. D. Baver, and D. Behrend, NASA/TP-2020-219041, 2020
- Bach U., Kraus A., Fürst E., Polatidis A., 2007, First report about the commissioning of the new Effelsberg sub-reflector, Effelsberg memo series
- Beckmann V., Shrader C., 2012, in Proceedings of “An INTEGRAL view of the high-energy sky (the first 10 years)” - 9th INTEGRAL Workshop and celebration of the 10th anniversary of the launch (INTEGRAL 2012). 15-19 October 2012. Bibliotheque Nationale de France. p. 69 ([arXiv:1302.1397](https://arxiv.org/abs/1302.1397))

- Biteau J., et al., 2020, [Nature Astronomy](#), **4**, 124
- Blandford R. D., Königl A., 1979, [ApJ](#), **232**, 34
- Blandford R. D., Payne D. G., 1982, [MNRAS](#), **199**, 883
- Blandford R. D., Znajek R. L., 1977, [MNRAS](#), **179**, 433
- Blandford R., Meier D., Readhead A., 2019, [Annual Review of Astronomy and Astrophysics](#), **57**, 467
- Blaufuss E., Kintscher T., Lu L., Tung C. F., 2019, in 36th International Cosmic Ray Conference (ICRC2019). p. 1021 ([arXiv:1908.04884](#))
- Chang Y. L., Arsioli B., Giommi P., Padovani P., Brandt C. H., 2019, [A&A](#), **632**, A77
- Cherenkov Telescope Array Consortium et al., 2019, Science with the Cherenkov Telescope Array, [doi:10.1142/10986](#).
- Chiu H.-Y., 1964, [Physics Today](#), **17**, 21
- Chou Y.-l., 1975, Statistical Analysis. Holt, Rinehart & Winston of Canada Ltd.
- Ciprini S., Tosti G., Teräsranata H., Aller H. D., 2004, [MNRAS](#), **348**, 1379
- Dhawan S., Jha S. W., Leibundgut B., 2018, [A&A](#), **609**, A72
- Donato D., Ghisellini G., Tagliaferri G., Fossati G., 2001, [A&A](#), **375**, 739
- Edelson R. A., Krolik J. H., 1988, [ApJ](#), **333**, 646
- Edelson R., Turner T. J., Pounds K., Vaughan S., Markowitz A., Marshall H., Dobbie P., Warwick R., 2002, [ApJ](#), **568**, 610
- Event Horizon Telescope Collaboration et al., 2019, [ApJ](#), **875**, L1
- Fanaroff B. L., Riley J. M., 1974, [MNRAS](#), **167**, 31P
- Fossati G., Maraschi L., Celotti A., Comastri A., Ghisellini G., 1998, [MNRAS](#), **299**, 433
- Fuhrmann L., et al., 2016, [A&A](#), **596**, A45
- Ghisellini G., 1999, [Astroparticle Physics](#), **11**, 11
- Ghisellini G., Tavecchio F., Chiaberge M., 2005, [A&A](#), **432**, 401
- Giommi P., Glauch T., Padovani P., Resconi E., Turcati A., Chang Y. L., 2020, [MNRAS](#), **497**, 865
- Giroletti M., et al., 2004, [ApJ](#), **600**, 127

- Giroletti M., Giovannini G., Cotton W. D., Taylor G. B., Pérez-Torres M. A., Chiaberge M., Edwards P. G., 2008, *A&A*, **488**, 905
- Greenstein J. L., 1963, *Nature*, **197**, 1041
- H. E. S. S. Collaboration et al., 2012, *A&A*, **538**, A103
- H. E. S. S. Collaboration et al., 2013, *A&A*, **559**, A136
- Hachisuka K., et al., 2006, *ApJ*, **645**, 337
- Henri G., Saugé L., 2006, *ApJ*, **640**, 185
- Heßdörfer J., 2021, Flux Density Measurements of TeV Blazars with the Effelsberg 100 m Telescope, B.Sc. Thesis, Julius-Maximilians Universität, Würzburg
- Hillas A. M., 1984, *ARA&A*, **22**, 425
- Hovatta T., Valtaoja E., Tornikoski M., Lähteenmäki A., 2009, *A&A*, **494**, 527
- Hovatta T., et al., 2021, *A&A*, **650**, A83
- IceCube Collaboration et al., 2018, *Science*, **361**, 147
- Jansky K. G., 1933, In *Electrical Disturbances Apparently of Extraterrestrial Origin*, 1982. Springer Netherlands, Dordrecht, p. 23, doi:10.1007/978-94-009-7752-5_2
- Kadler M., et al., 2016, *Nature Physics*, **12**, 807
- Kadler M., et al., 2021, *PoS*, ICRC2021, 974
- Kaufmann S., Wagner S. J., Tibolla O., Hauser M., 2011, *A&A*, **534**, A130
- Keenan M., Meyer E. T., Georganopoulos M., Reddy K., French O. J., 2021, *MNRAS*, **505**, 4726
- Kellermann K. I., Sramek R., Schmidt M., Shaffer D. B., Green R., 1989, *AJ*, **98**, 1195
- Kraus J. D., 1966, *Radio Astronomy*. McGraw-Hill Inc., New York
- Kraus A., et al., 2003, *A&A*, **401**, 161
- Lahteenmaki A., Valtaoja E., Wiik K., 1999, *ApJ*, **511**, 112
- Lico R., Giroletti M., Orienti M., Costamante L., Pavlidou V., D’Ammando F., Tavacchio F., 2017, *A&A*, **606**, A138
- Lindfors E. J., et al., 2016, *A&A*, **593**, A98
- Lioudakis I., et al., 2017, *MNRAS*, **466**, 4625

- Mannheim K., 1993, *A&A*, [269](#), [67](#)
- Matthews T. A., Sandage A. R., 1963, *ApJ*, [138](#), [30](#)
- Moré J. J., 1978, in Watson G. A., ed., *Numerical Analysis*. Springer Berlin Heidelberg, Berlin, Heidelberg, pp 105–116
- Murase K., Oikonomou F., Petropoulou M., 2018, *ApJ*, [865](#), [124](#)
- Nieppola E., Tornikoski M., Valtaoja E., 2006, *A&A*, [445](#), [441](#)
- Ott M., Witzel A., Quirrenbach A., Krichbaum T. P., Standke K. J., Schalinski C. J., Hummel C. A., 1994, *A&A*, [284](#), [331](#)
- Padovani P., Giommi P., 1995, *ApJ*, [444](#), [567](#)
- Padovani P., Petropoulou M., Giommi P., Resconi E., 2015, *MNRAS*, [452](#), [1877](#)
- Padovani P., Giommi P., Resconi E., Glauch T., Arsioli B., Sahakyan N., Huber M., 2018, *MNRAS*, [480](#), [192](#)
- Paiano S., Landoni M., Falomo R., Treves A., Scarpa R., Righi C., 2017, *ApJ*, [837](#), [144](#)
- Perley R. A., Butler B. J., 2013, *ApJS*, [204](#), [19](#)
- Perley R. A., Butler B. J., 2017, *ApJS*, [230](#), [7](#)
- Peterson B. M., Wanders I., Horne K., Collier S., Alexander T., Kaspi S., Maoz D., 1998, *PASP*, [110](#), [660](#)
- Pian E., et al., 1998, *ApJ*, [492](#), [L17](#)
- Piner B. G., Edwards P. G., 2018, *ApJ*, [853](#), [68](#)
- Plavin A., Kovalev Y. Y., Kovalev Y. A., Troitsky S., 2020, *ApJ*, [894](#), [101](#)
- Plavin A. V., Kovalev Y. Y., Kovalev Y. A., Troitsky S. V., 2021, *ApJ*, [908](#), [157](#)
- Readhead A. C. S., 1994, *ApJ*, [426](#), [51](#)
- Richards J. L., et al., 2011, *ApJS*, [194](#), [29](#)
- Rodrigues X., Garrappa S., Gao S., Paliya V. S., Franckowiak A., Winter W., 2021, *ApJ*, [912](#), [54](#)
- Romero G. E., Boettcher M., Markoff S., Tavecchio F., 2017, *Space Sci. Rev.*, [207](#), [5](#)
- Ruze J., 1966, *IEEE Proceedings*, [54](#), [633](#)

- Rybicki G. B., Lightman A. P., 1979, *Radiative Processes in Astrophysics*. John Wiley & Sons, Inc., New York
- Sacahui J. R., Penacchioni A. V., Marinelli A., Sharma A., Castro M., Osorio J. M., Morales M. A., 2021, [Rev. Mexicana Astron. Astrofis.](#), **57**, 251
- Sato R., Kataoka J., Takahashi T., Medejski G. M., Rügamer S., Wagner S. J., 2008, [AIP Conference Proceedings](#), 1085, 447
- Savolainen T., Homan D. C., Hovatta T., Kadler M., Kovalev Y. Y., Lister M. L., Ros E., Zensus J. A., 2010, [A&A](#), **512**, A24
- Schmidt M., 1963, [Nature](#), **197**, 1040
- Seyfert C. K., 1943, [ApJ](#), **97**, 28
- Shakura N. I., Sunyaev R. A., 1973, [A&A](#), **500**, 33
- Shapiro S. S., Wilk M. B., 1965, [Biometrika](#), **52**, 591
- Shaw M. S., et al., 2012, [ApJ](#), **748**, 49
- Shaw M. S., et al., 2013, [ApJ](#), **764**, 135
- Shu F., 1991, *Physics of Astrophysics: Volume I Radiation*. University Science Books, Mill Valley, CA
- Sikora M., Begelman M. C., Rees M. J., 1994, [ApJ](#), **421**, 153
- Singh K. K., Meintjes P. J., 2020, [Astronomische Nachrichten](#), **341**, 713
- Soldi S., et al., 2008, [A&A](#), **486**, 411
- Sowards-Emmerd D., Romani R. W., Michelson P. F., Healey S. E., Nolan P. L., 2005, [ApJ](#), **626**, 95
- Sun W.-H., Malkan M. A., 1989, [ApJ](#), **346**, 68
- Tavecchio F., Maraschi L., Ghisellini G., 1998, [ApJ](#), **509**, 608
- Tavecchio F., Ghisellini G., Ghirlanda G., Foschini L., Maraschi L., 2010, [MNRAS](#), **401**, 1570
- Tavecchio F., Ghisellini G., Guetta D., 2014, [ApJ](#), **793**, L18
- Urry C. M., Padovani P., 1995, [PASP](#), **107**, 803
- Venters T. M., Pavlidou V., 2007, [ApJ](#), **666**, 128
- White R. J., Peterson B. M., 1994, [PASP](#), **106**, 879
- Zijlstra A. A., van Hoof P. A. M., Perley R. A., 2008, [ApJ](#), **681**, 1296

Appendix A

Averaged Light Curves

In this chapter, all averaged light curves (as described in Sect. 3.5.2) are presented. Each plot consists of an upper panel, which shows the light curve at 14 mm and - if detected - at 7 mm. The lower panel indicates the dates when the source was observed at either 14 mm or 7 mm. For sources where flares are detected, the flare start point and peak point used for the flare analysis in Sect. 4.3 are highlighted with red circles. Note that all plots have different y-axes scales, excluding zero, in order to improve readability.

Fig. A.1: Sub-band averaged light curves of the four calibrators from August 2020 to October 2021 at 14 mm and 7 mm, including the two main calibrator sources 3C286 and NGC7027.

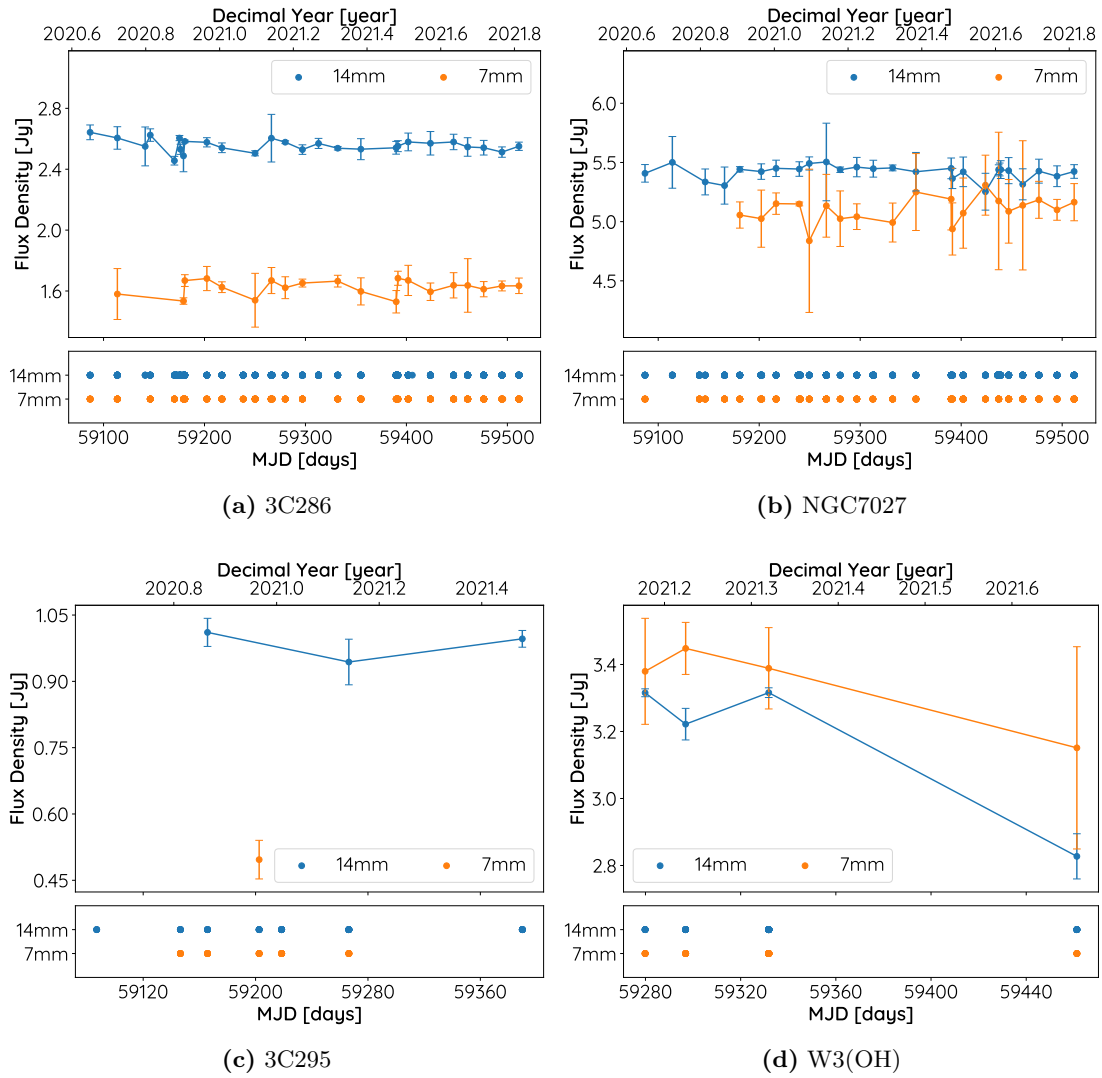
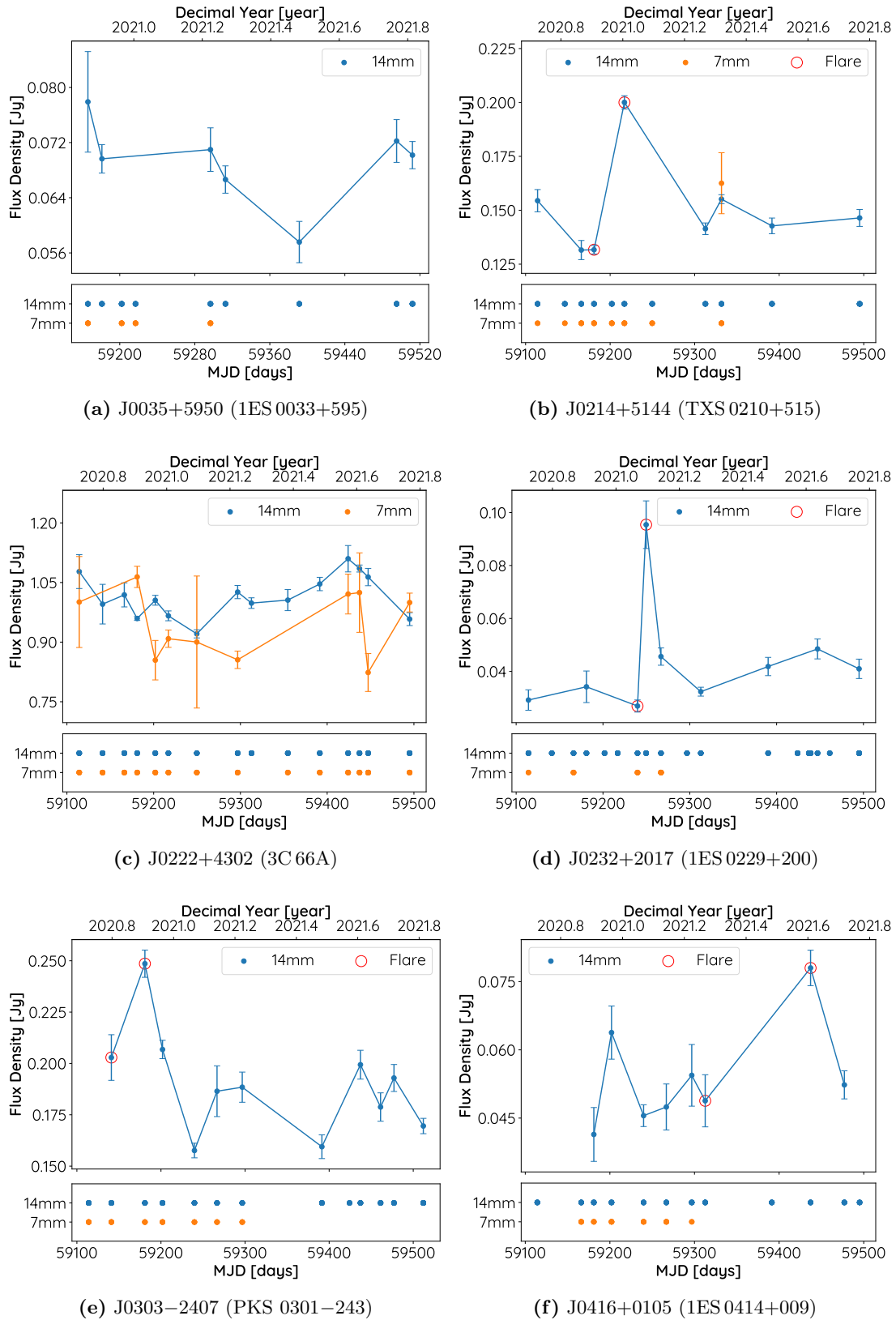
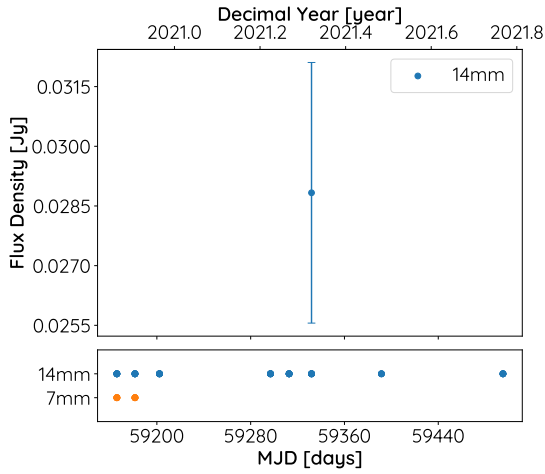
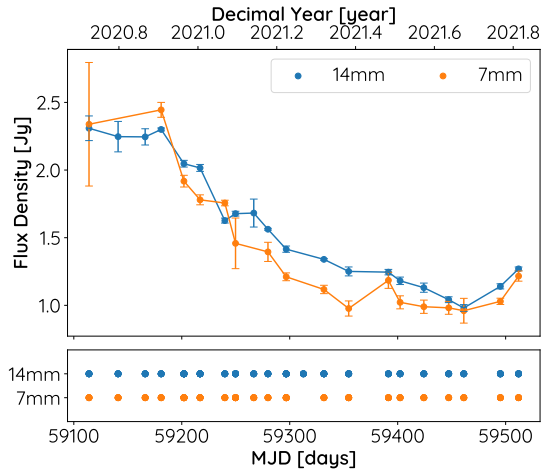


Fig. A.2: Sub-band averaged light curves of all detected HBLs and XBLs in the TELAMON sample from August 2020 to October 2021 at 14 mm and 7 mm.

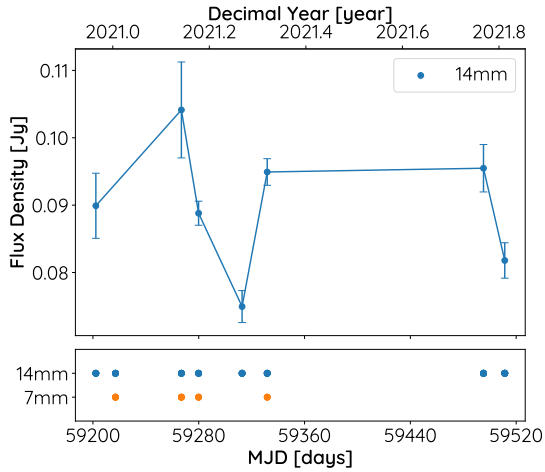




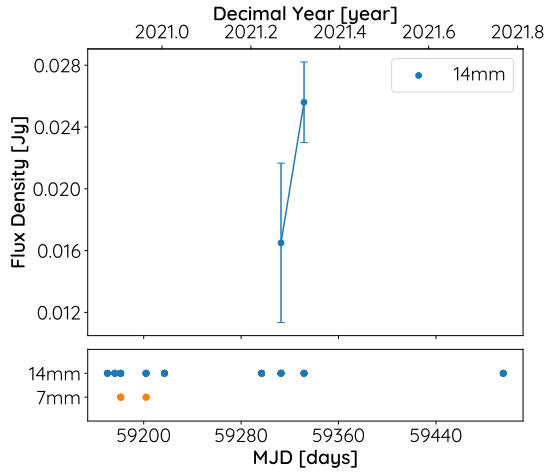
(g) J0507+6737 (1ES 0502+675)



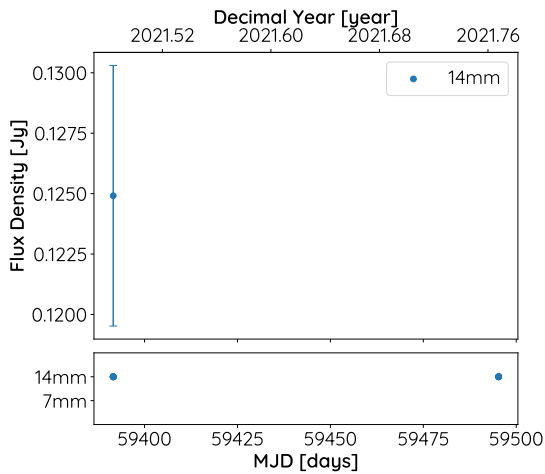
(h) J0509+0541 (TXS 0506+056)



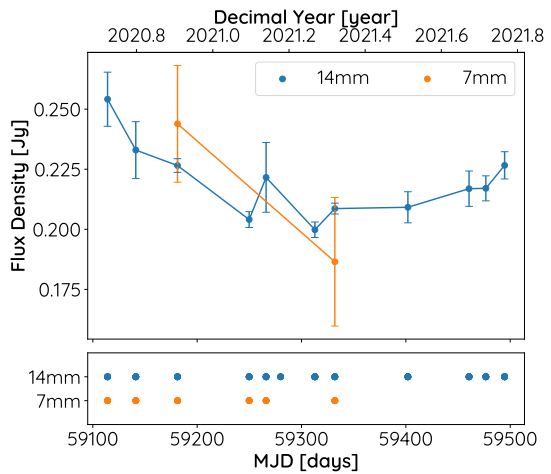
(i) J0650+2502 (1ES 0647+250)



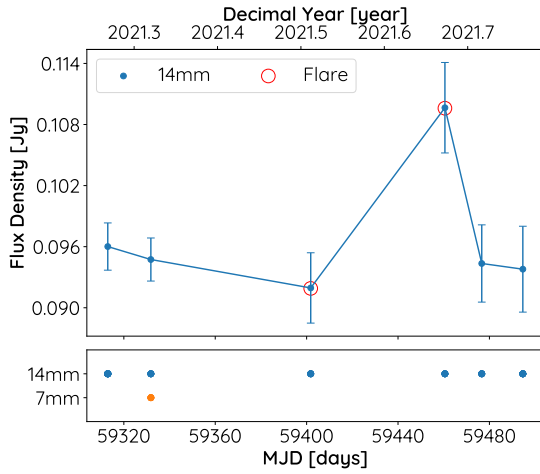
(j) J0658+0637 (NVSS J065844+063711)



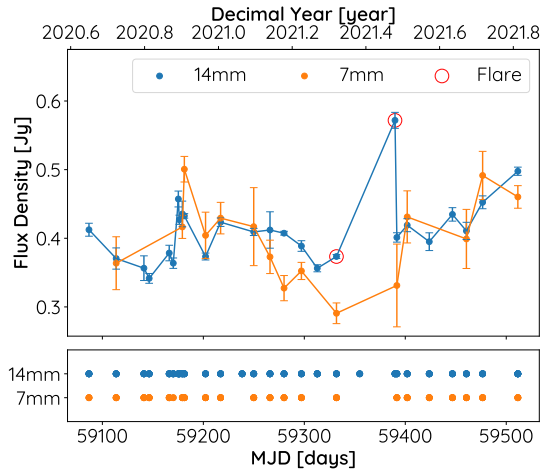
(k) J0913-2103 (MRC 0910-208)



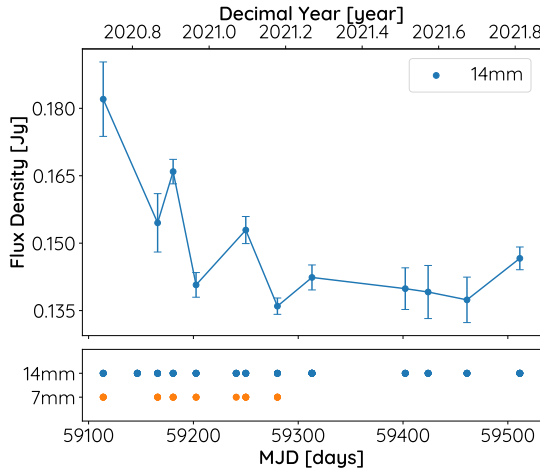
(l) J1015+4926 (1ES 1011+496)



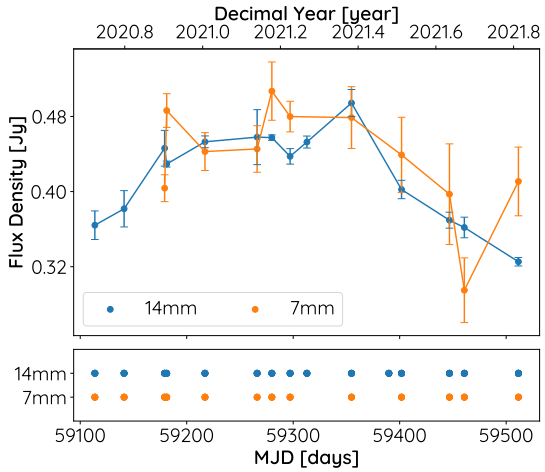
(m) J1058+2817 (GB6 J1058+2817)



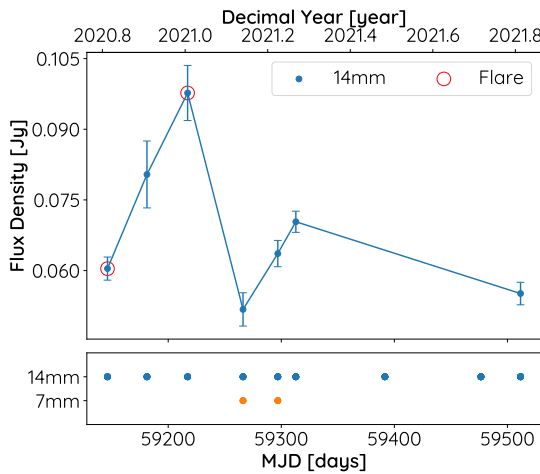
(n) J1104+3812 (Mrk 421)



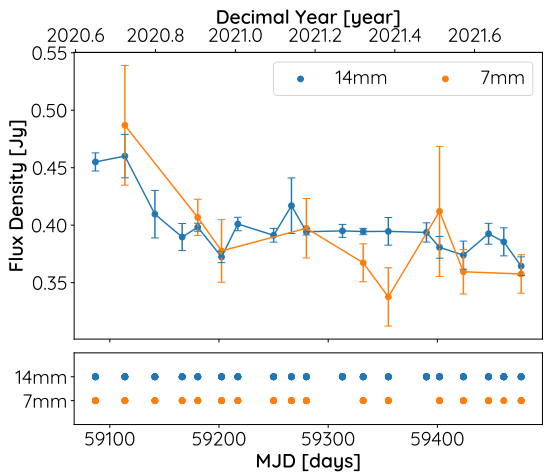
(o) J1136+7009 (Mrk 180)



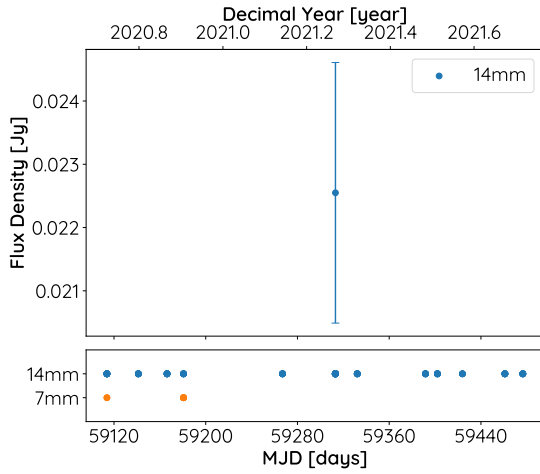
(p) J1217+3007 (ON 325)



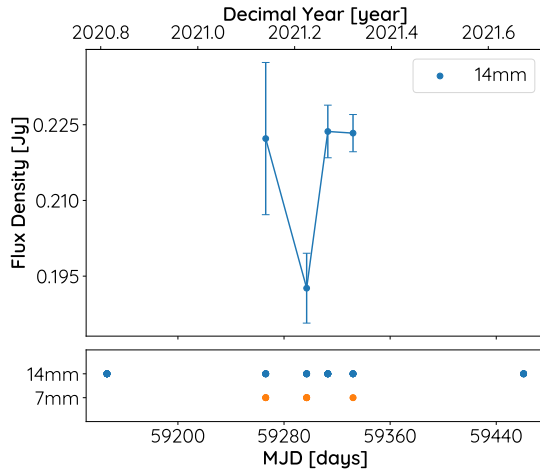
(q) J1221+3010 (1ES 1218+304)



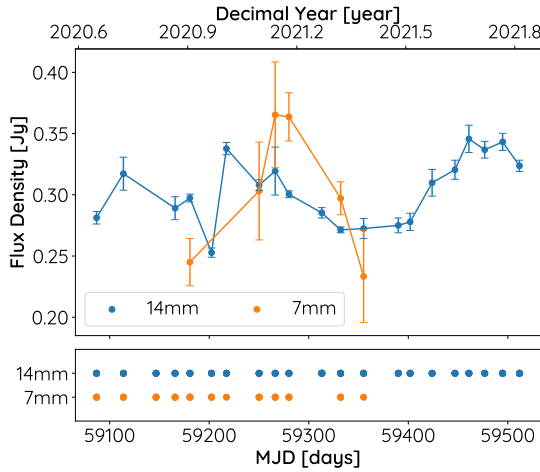
(r) J1427+2348 (OQ 240)



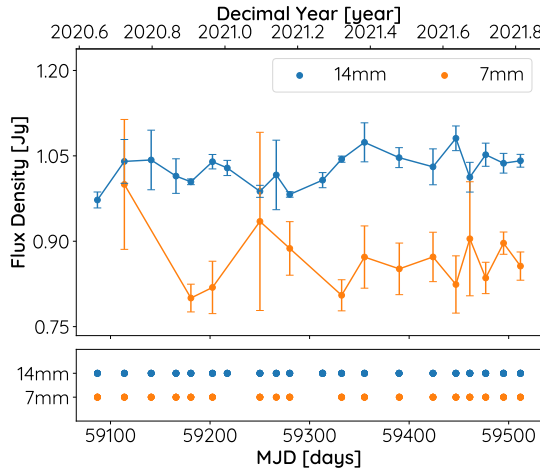
(s) J1428+4240 (1ES 1426+428)



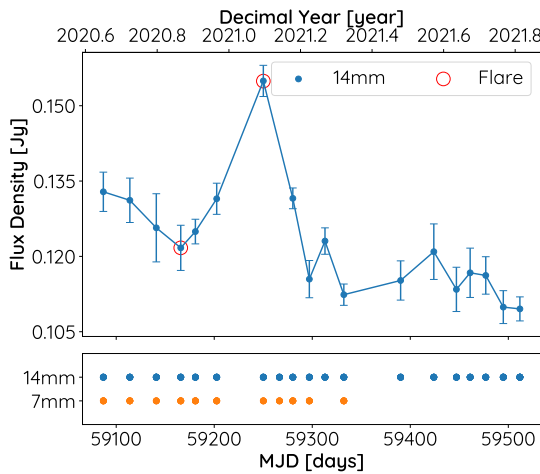
(t) J1518-2731 (TXS 1515-273)



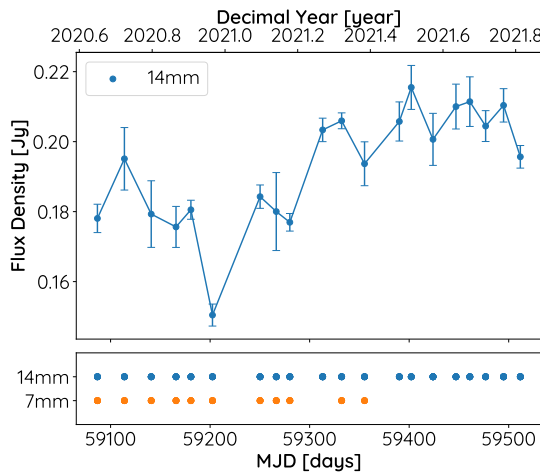
(u) J1555+1111 (PG 1553+113)



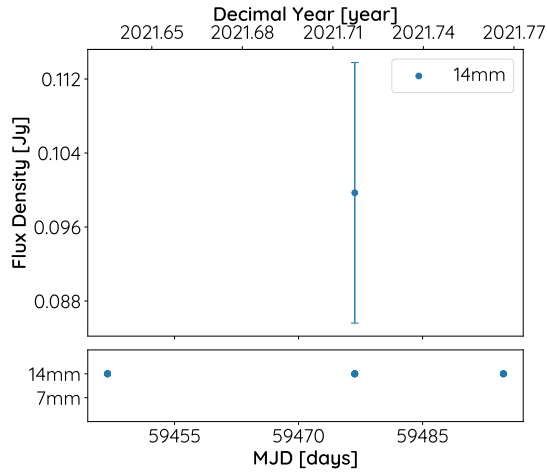
(v) J1653+3945 (Mrk 501)



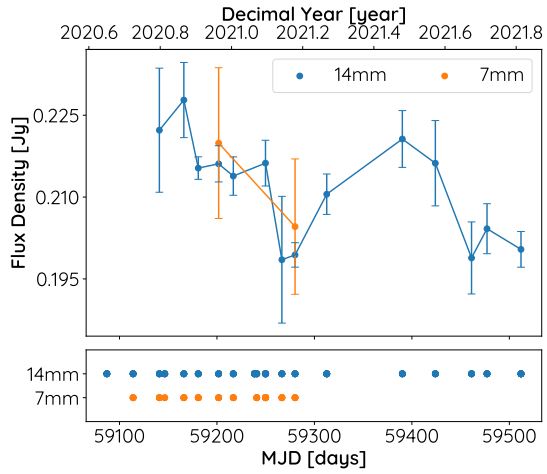
(w) J1728+5013 (1Zw 187)



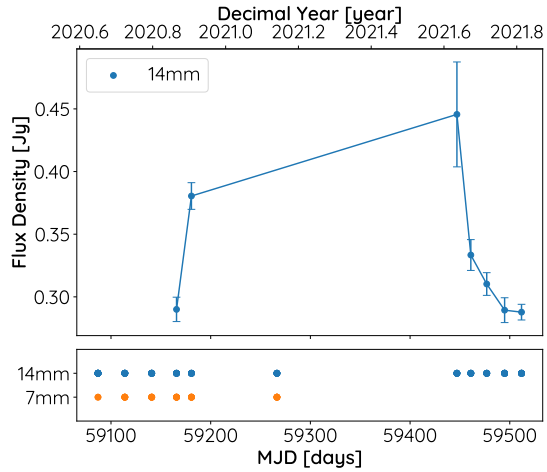
(x) J1743+1935 (1ES 1741+196)



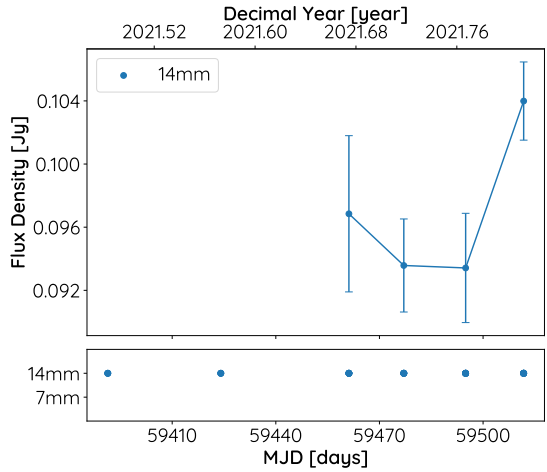
(y) J1958-3011 (1RXS J195815.6–301119)



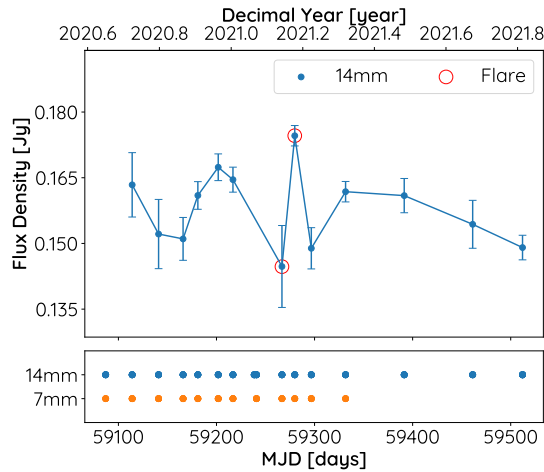
(z) J1959+6508 (1ES 1959+650)



(aa) J2158-3013 (PKS 2155–304)



(ab) J2243+2021 (RGB J2243+203)



(ac) J2347+5142 (1ES 2344+514)

Appendix B

Spectra

In this section, the spectra of all calibrators and XBLs and HBLs monitored by TELAMON between August 2020 and October 2021 at 14 mm and 7 mm are presented. The different colors represent the MJD of the observation as indicated by the color map. Note that all plots have different y-axes scales, excluding zero, in order to improve readability.

Fig. B.1: Spectra of the four calibrators from August 2020 to October 2021 at 14 mm and 7 mm, including the two main calibrator sources 3C286 and NGC7027. The color map indicates the MJD of the observation.

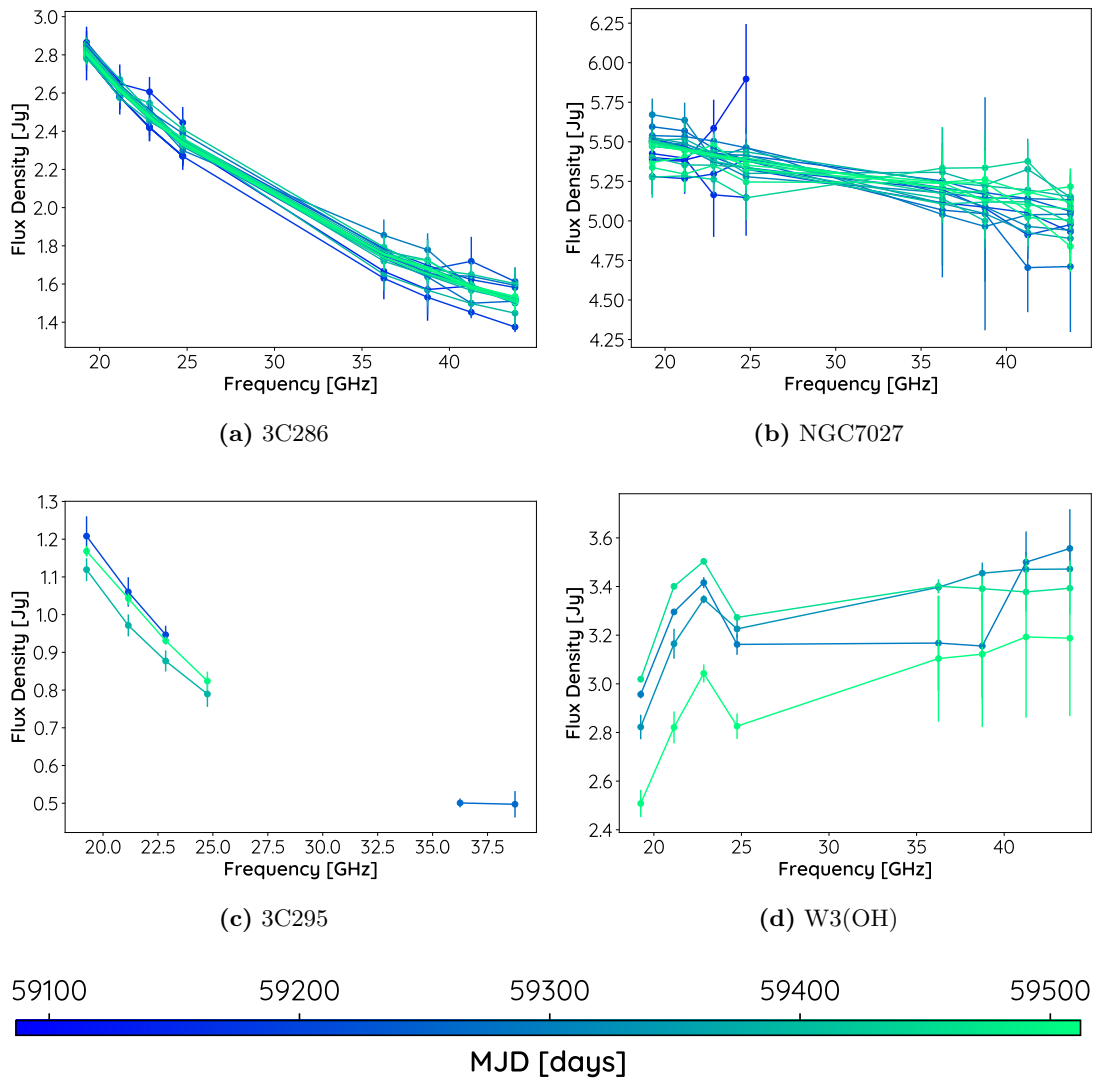
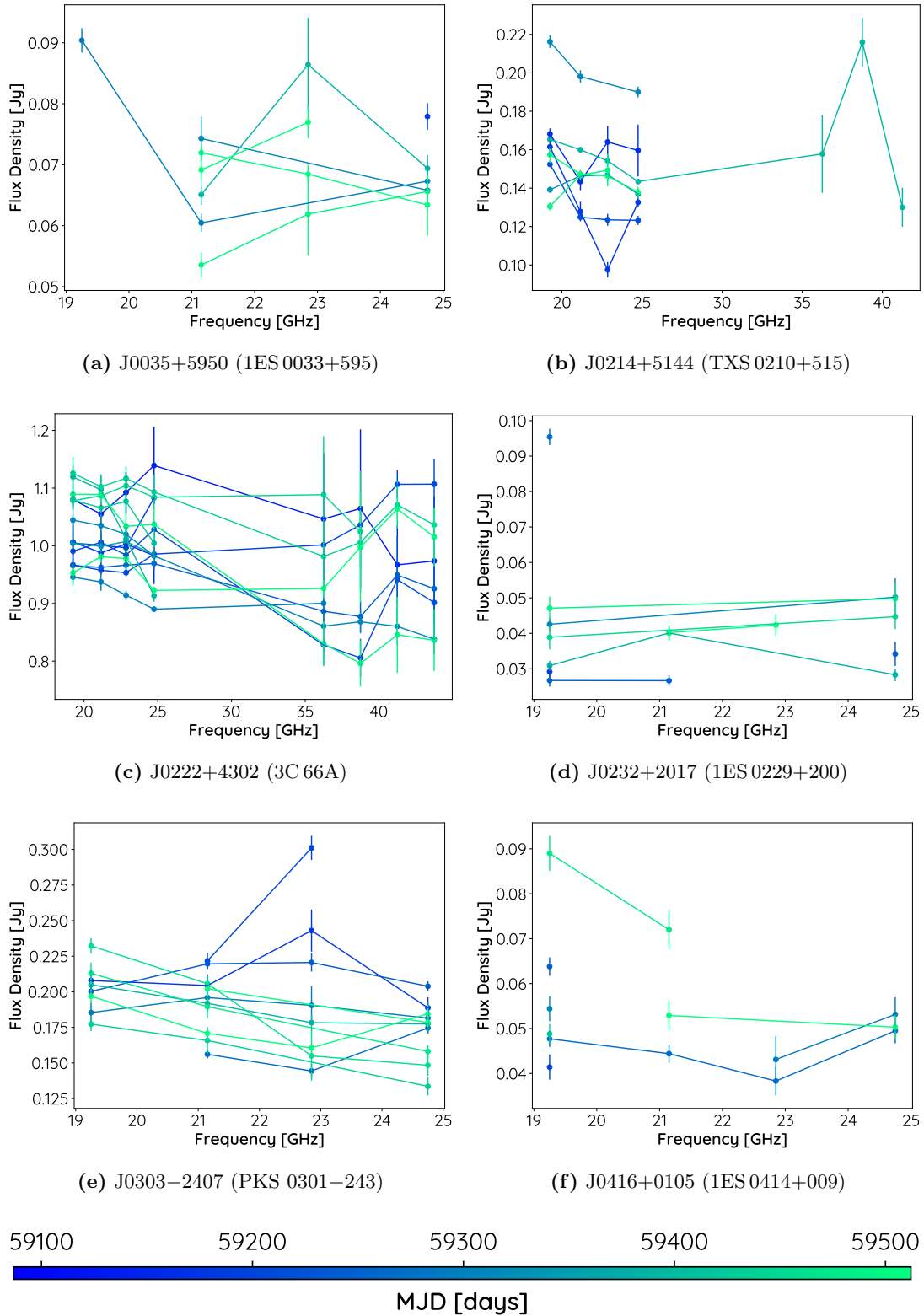
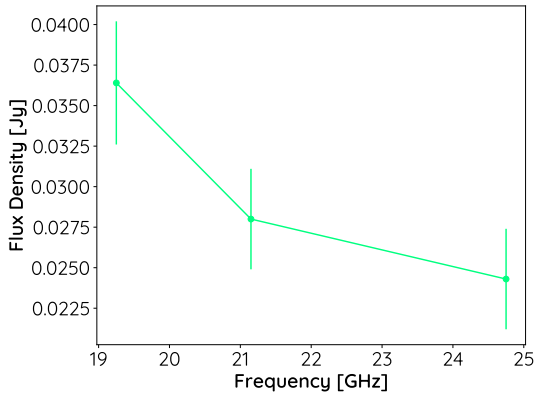
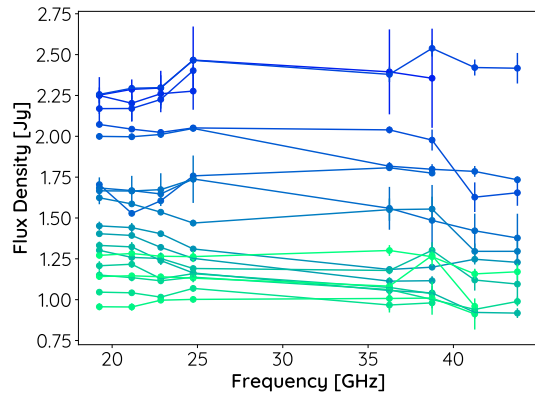


Fig. B.2: Spectra of all detected HBLs and XBLs in the TELAMON sample from August 2020 to October 2021. The color map indicates the MJD of when the observation took place.

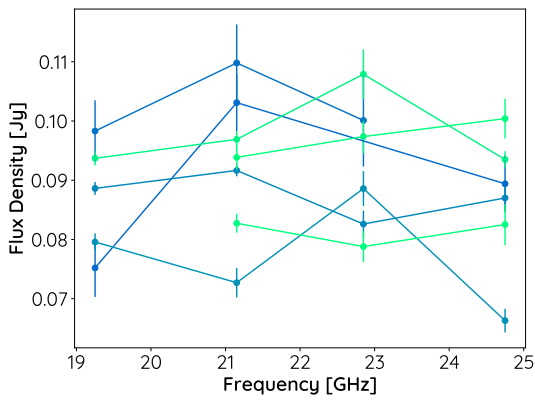




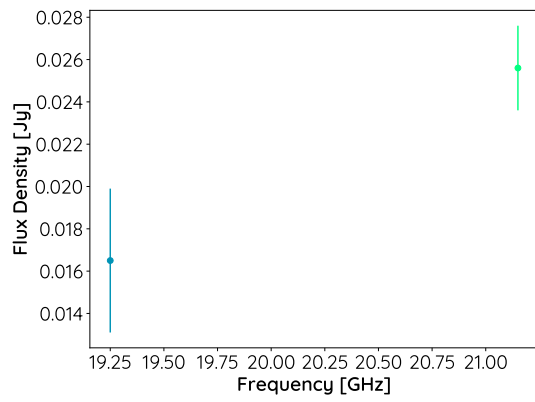
(g) J0507+6737 (1ES 0502+675)



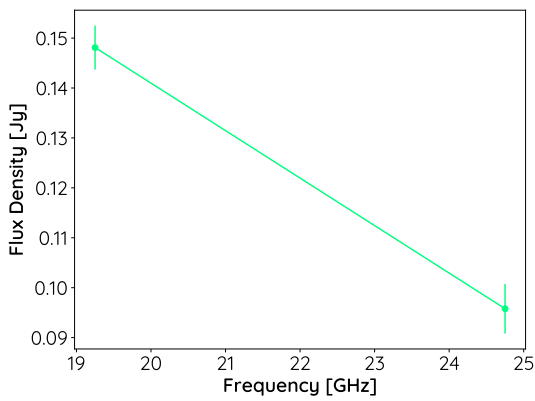
(h) J0509+0541 (TXS 0506+056)



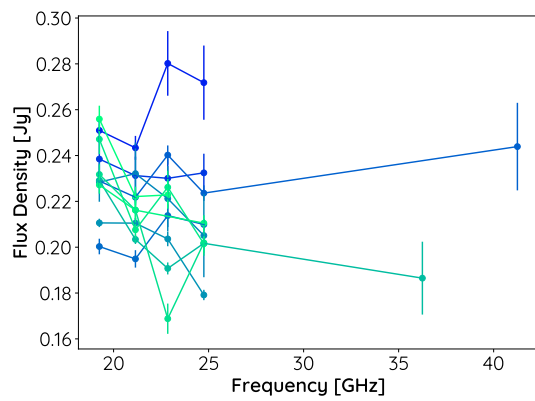
(i) J0650+2502 (1ES 0647+250)



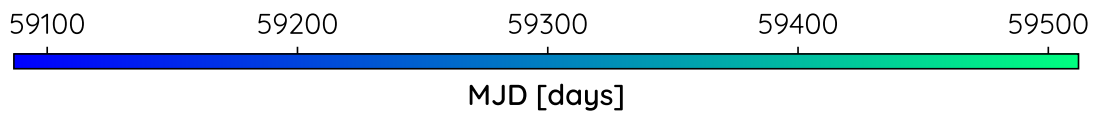
(j) J0658+0637 (NVSS J065844+063711)

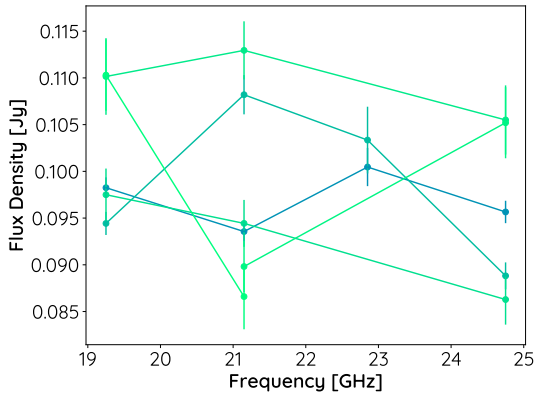


(k) J0913-2103 (MRC 0910-208)

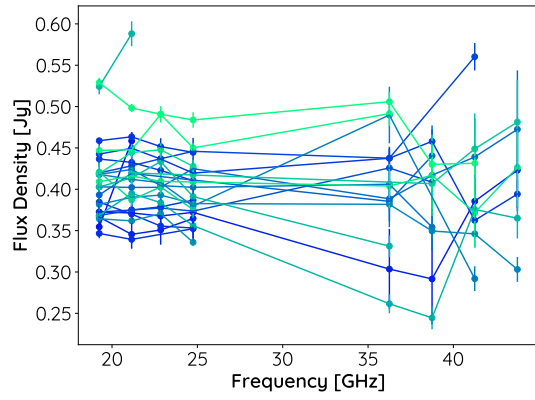


(l) J1015+4926 (1ES 1011+496)

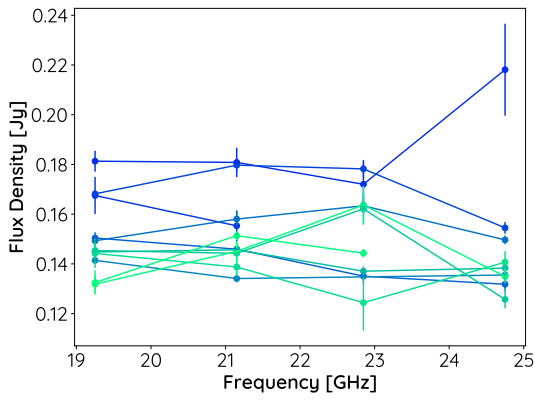




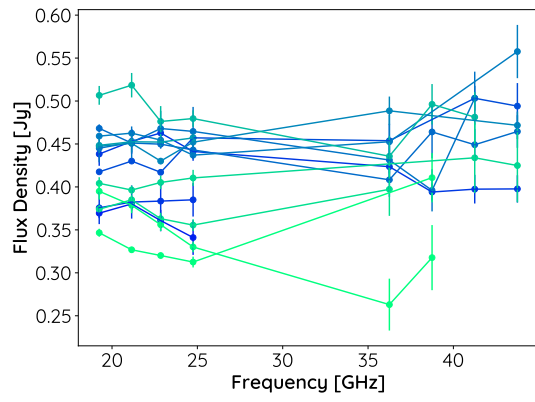
(m) J1058+2817 (GB6 J1058+2817)



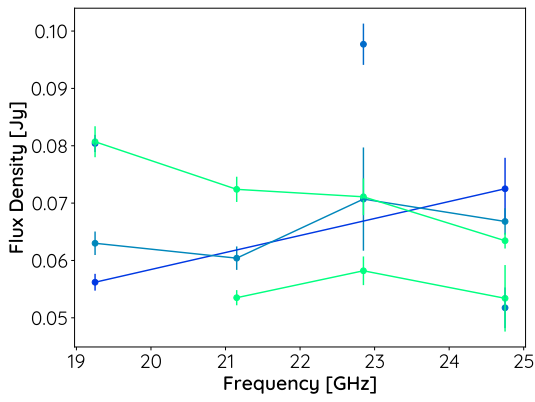
(n) J1104+3812 (Mrk 421)



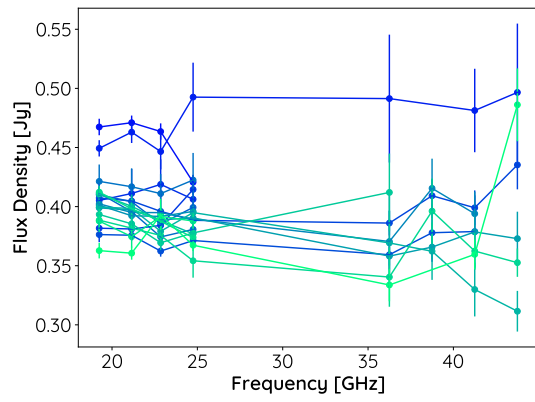
(o) J1136+7009 (Mrk 180)



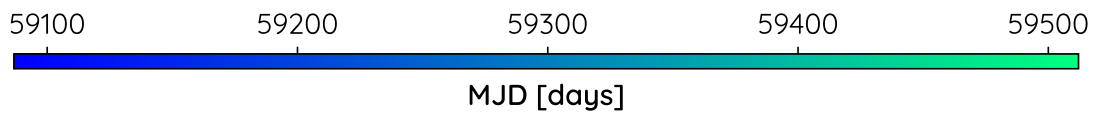
(p) J1217+3007 (ON 325)

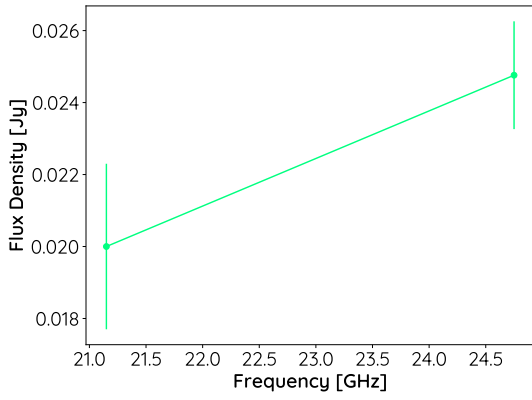


(q) J1221+3010 (1ES 1218+304)

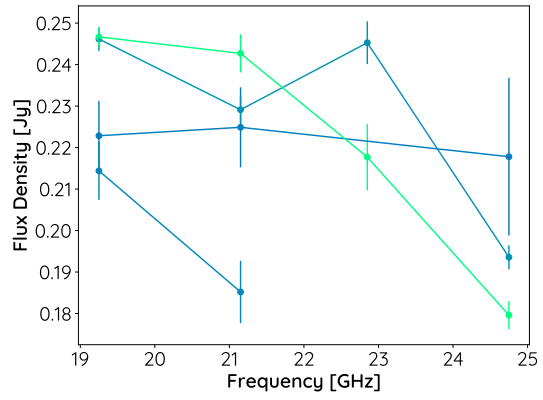


(r) J1427+2348 (OQ 240)

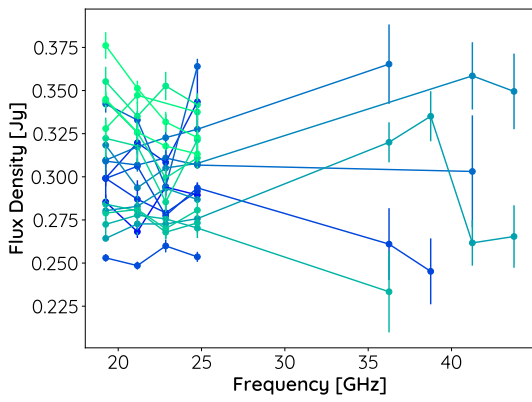




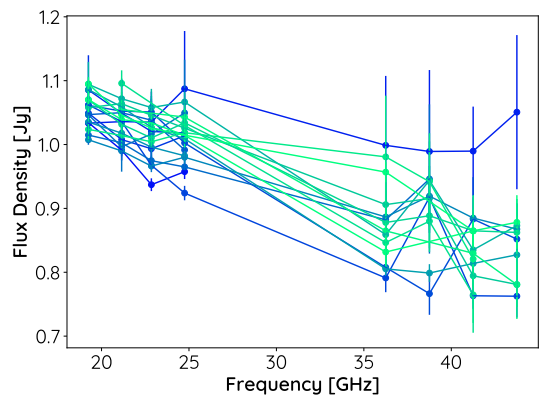
(s) J1428+4240 (1ES 1426+428)



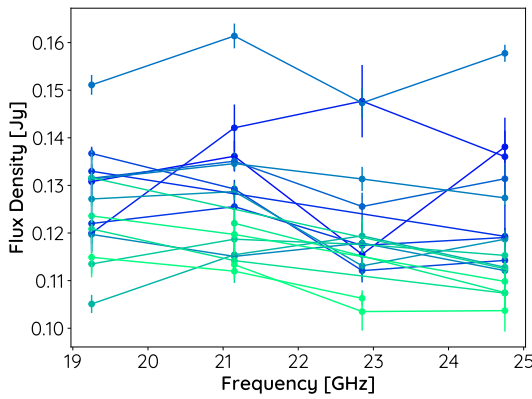
(t) J1518-2731 (TXS 1515-273)



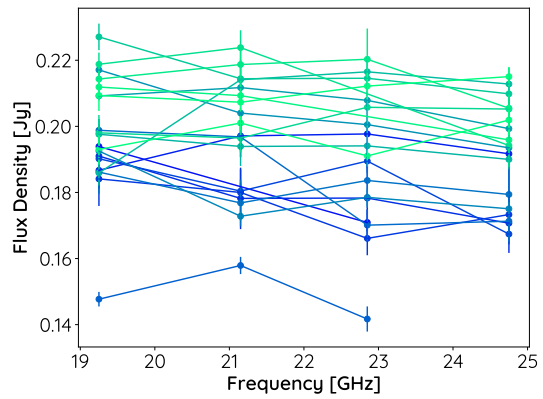
(u) J1555+1111 (PG 1553+113)



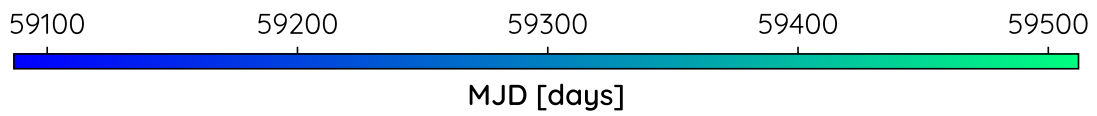
(v) J1653+3945 (Mrk 501)

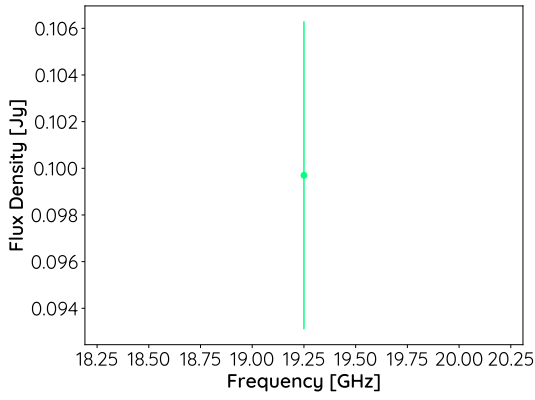


(w) J1728+5013 (IZw 187)

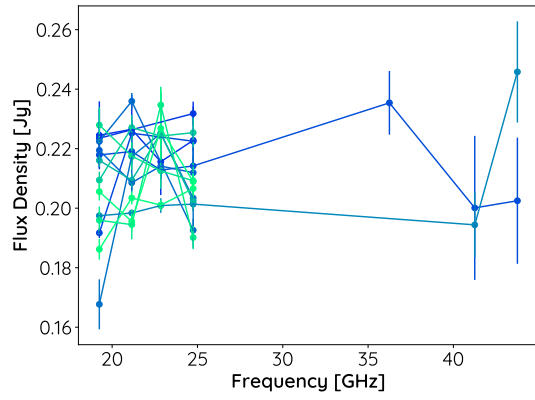


(x) J1743+1935 (1ES 1741+196)

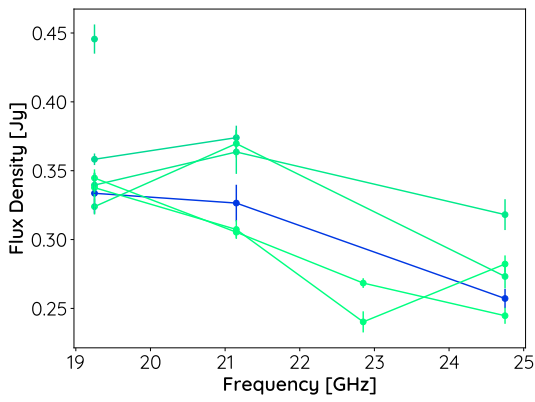




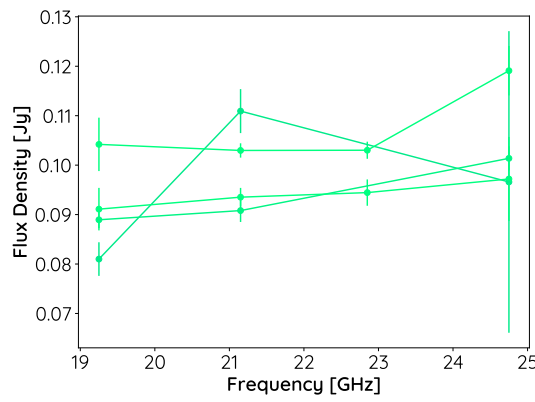
(y) J1958-3011 (1RXS J195815.6–301119)



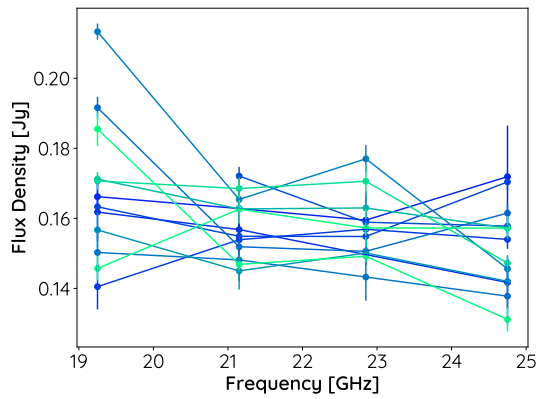
(z) J1959+6508 (1ES 1959+650)



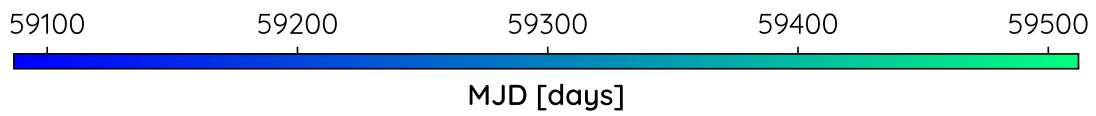
(aa) J2158-3013 (PKS 2155–304)



(ab) J2243+2021 (RGB J2243+203)



(ac) J2347+5142 (1ES 2344+514)

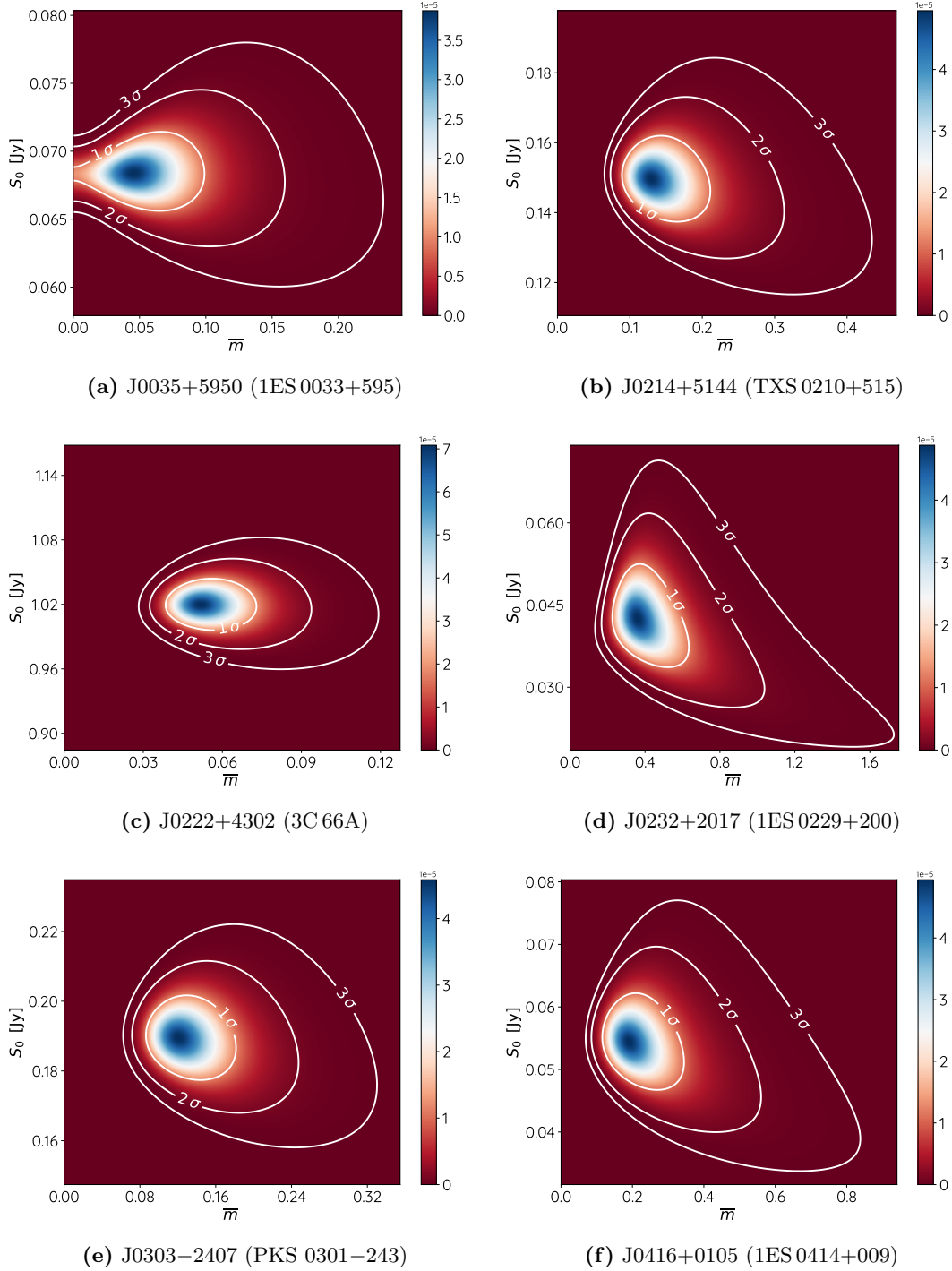


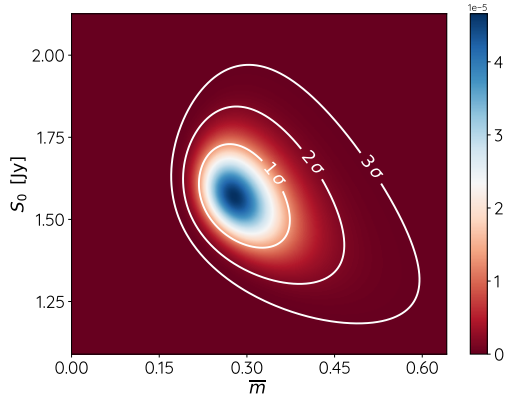
Appendix C

Intrinsic Modulation Index

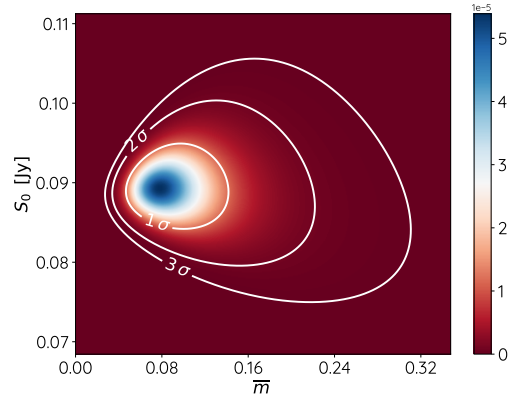
In this section, all likelihood maps used for the calculation of the intrinsic modulation index from TELAMON light curves at 14 mm and 7 mm are presented. The color map indicates the value of the likelihood map $\mathcal{L}(S_0, \bar{m})$ as defined in Equation (4.9). For five sources (J0507+6737, J0658+0637, J0913-2103, J1428+4240, J1958-3011) there was not enough light curve data available at 14 mm (i.e., < 3 detections) to calculate the modulation index. On the other hand, at 7 mm only six sources have a good enough sampling (i.e., > 2 detections) to calculate a modulation index. Note that all plots have different y-axes scales, excluding zero, in order to improve readability.

Fig. C.1: Likelihood maps calculated from TELAMON 14 mm light curves for all sources detected in more than two epochs at this wavelength. The color map indicates the value of the likelihood map $\mathcal{L}(S_0, \bar{m})$ as defined in Equation (4.9).

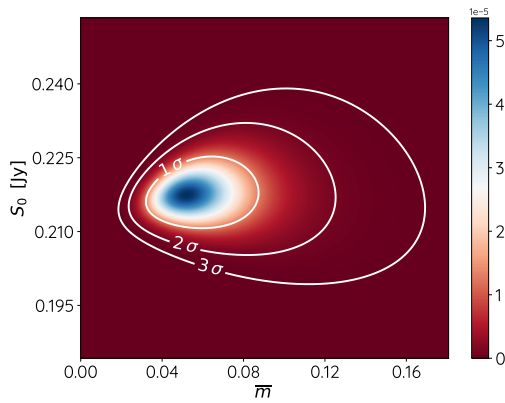




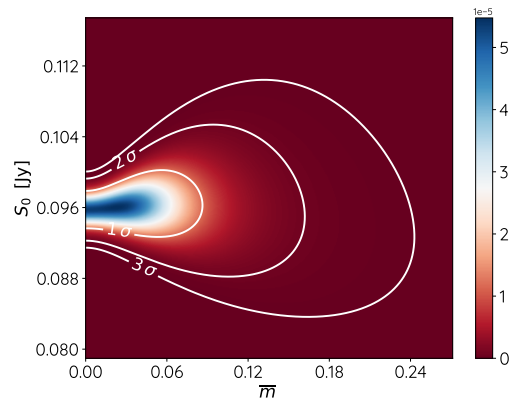
(g) J0509+0541 (TXS 0506+056)



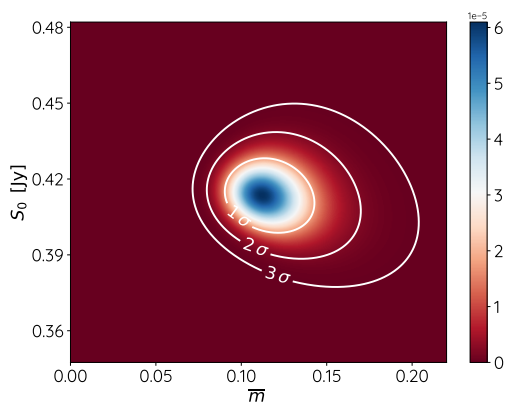
(h) J0650+2502 (1ES 0647+250)



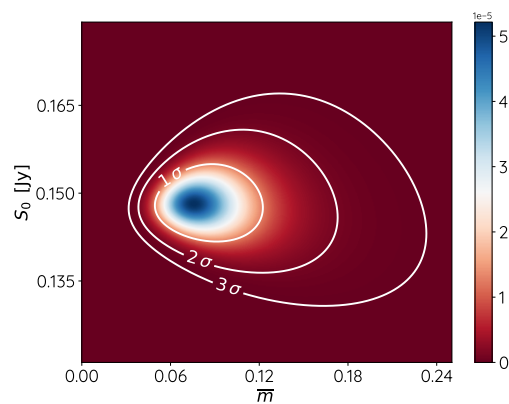
(i) J1015+4926 (1ES 1011+496)



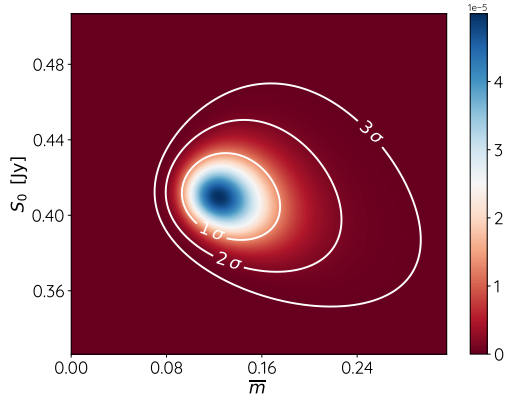
(j) J1058+2817 (GB6 J1058+2817)



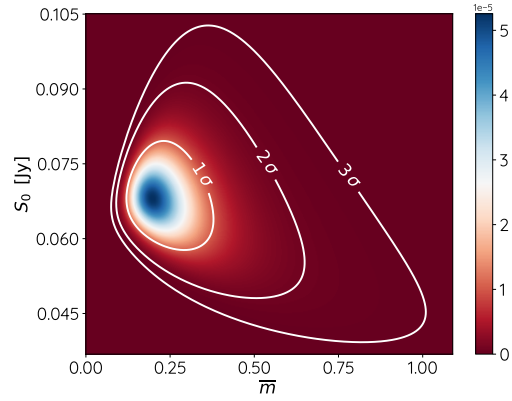
(k) J1104+3812 (Mrk 421)



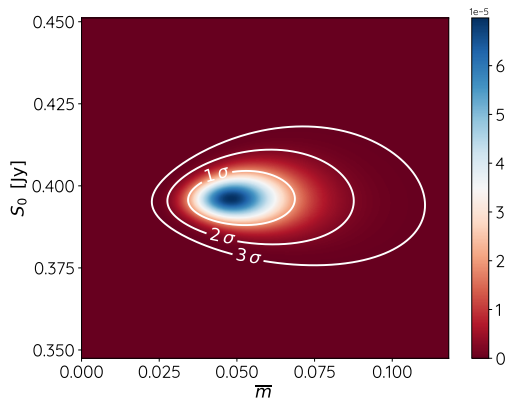
(l) J1136+7009 (Mrk 180)



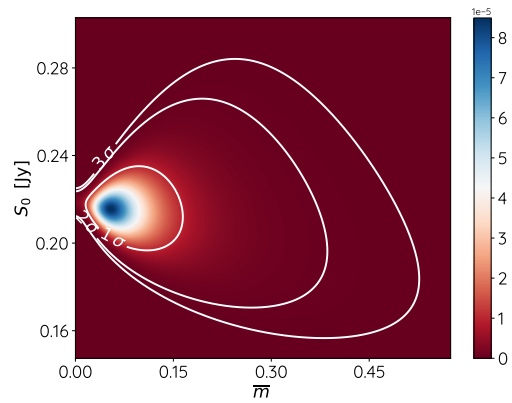
(m) J1217+3007 (ON 325)



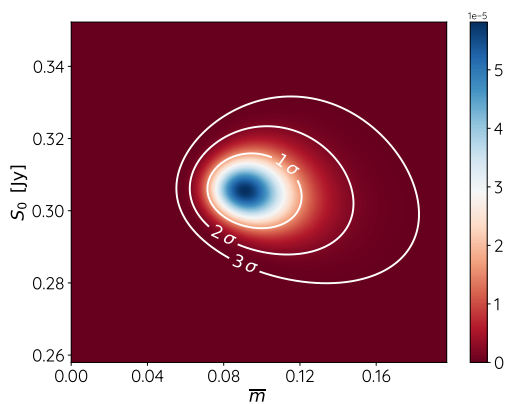
(n) J1221+3010 (1ES 1218+304)



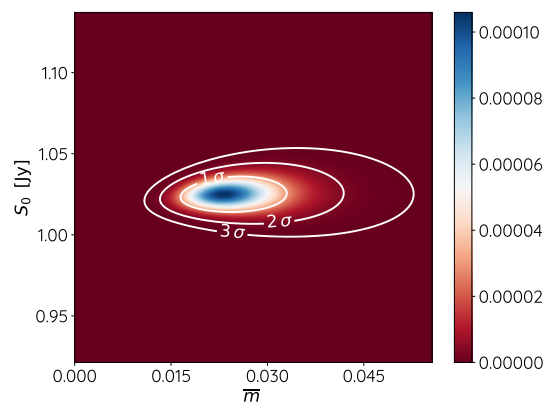
(o) J1427+2348 (OQ 240)



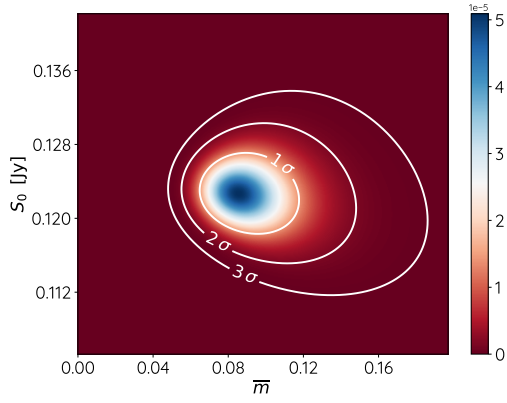
(p) J1518-2731 (TXS 1515-273)



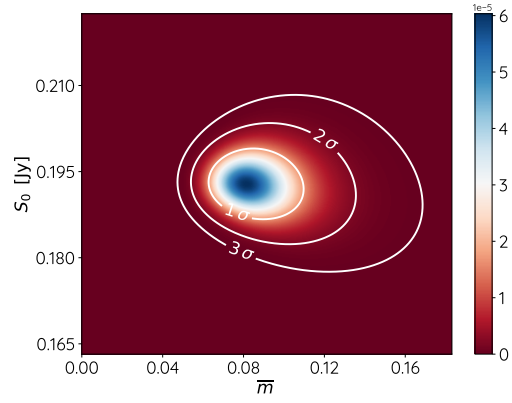
(q) J1555+1111 (PG 1553+113)



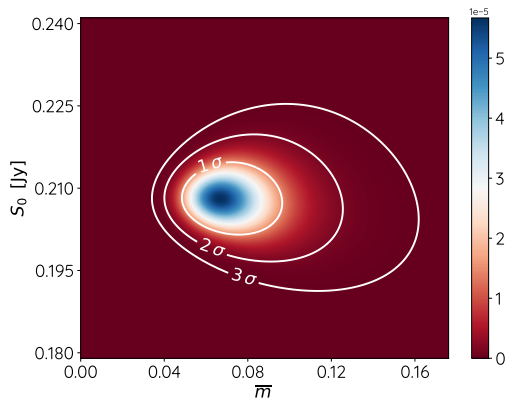
(r) J1653+3945 (Mrk 501)



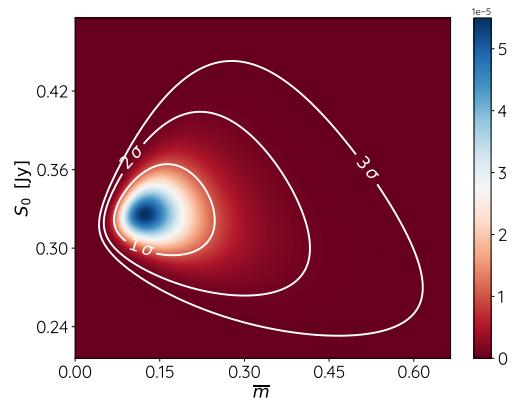
(s) J1728+5013 (IZw 187)



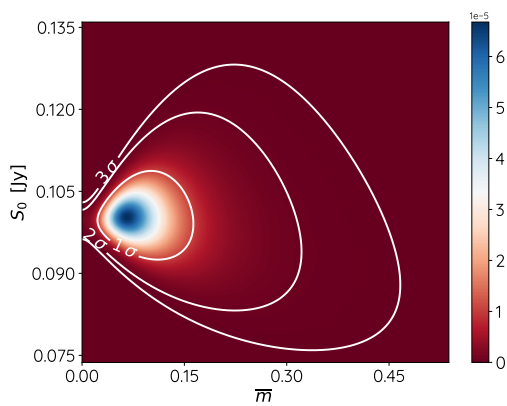
(t) J1743+1935 (1ES 1741+196)



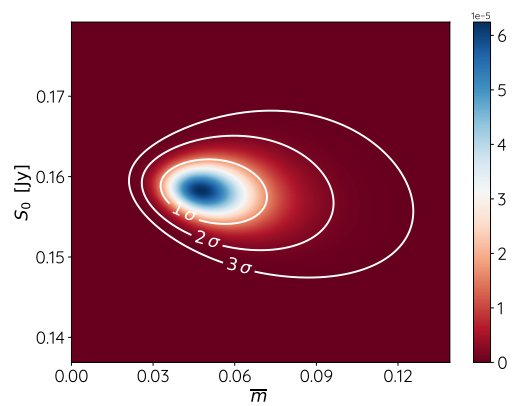
(u) J1959+6508 (1ES 1959+650)



(v) J2158-3013 (PKS 2155-304)

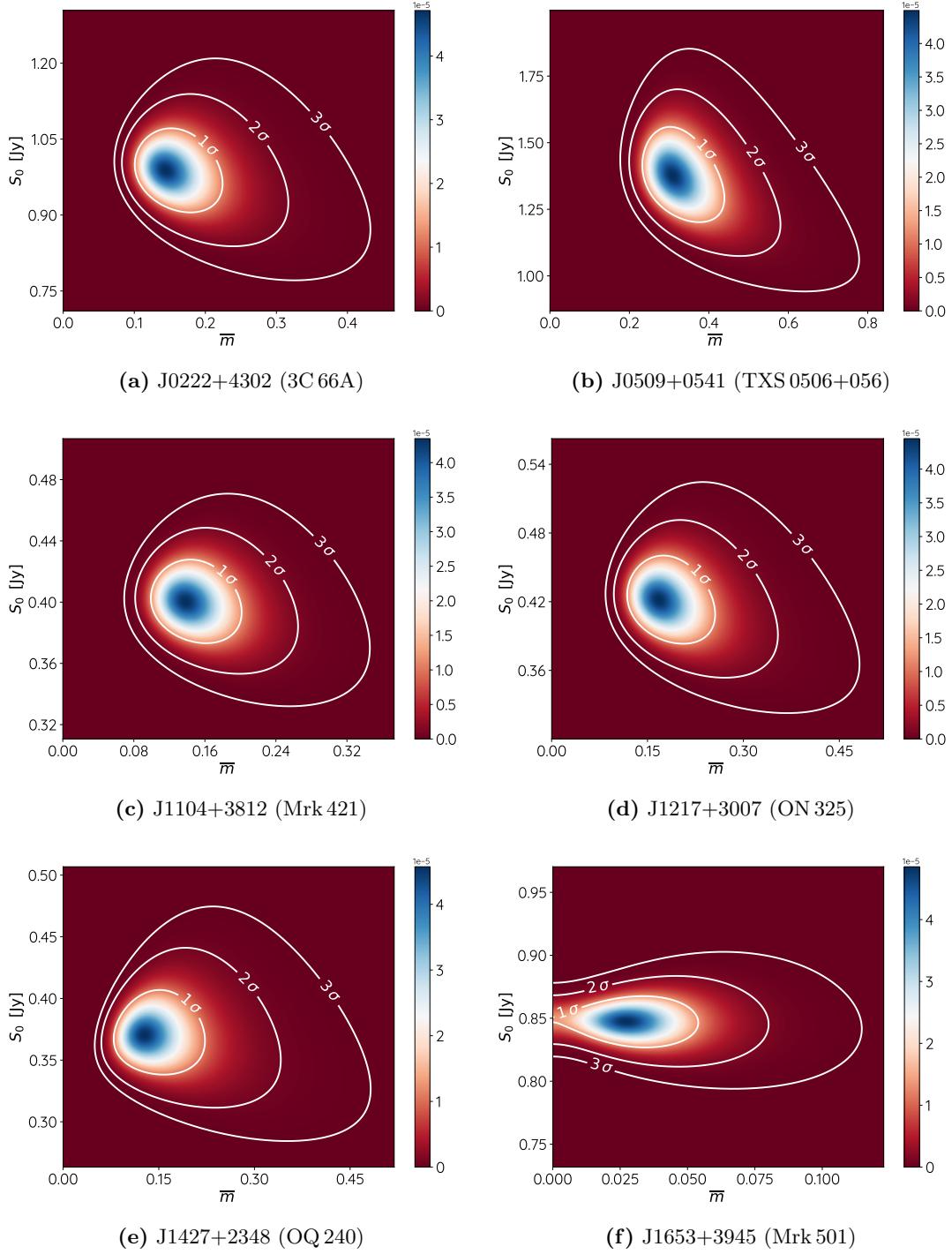


(w) J2243+2021 (RGB J2243+203)



(x) J2347+5142 (1ES 2344+514)

Fig. C.-1: Likelihood maps calculated from TELAMON 7 mm light curves for all sources detected in more than two epochs at this wavelength. The colormap indicates the value of the likelihood map $\mathcal{L}(S_0, \bar{m})$ as defined in Equation (4.9).



Appendix D

Calibration Factor Evolution

Fig. D.1: Calibration factor evolution for all sub-frequencies of the 14 mm receiver, namely 19.25 GHz, 21.15 GHz, 22.85 GHz, 24.75 GHz.

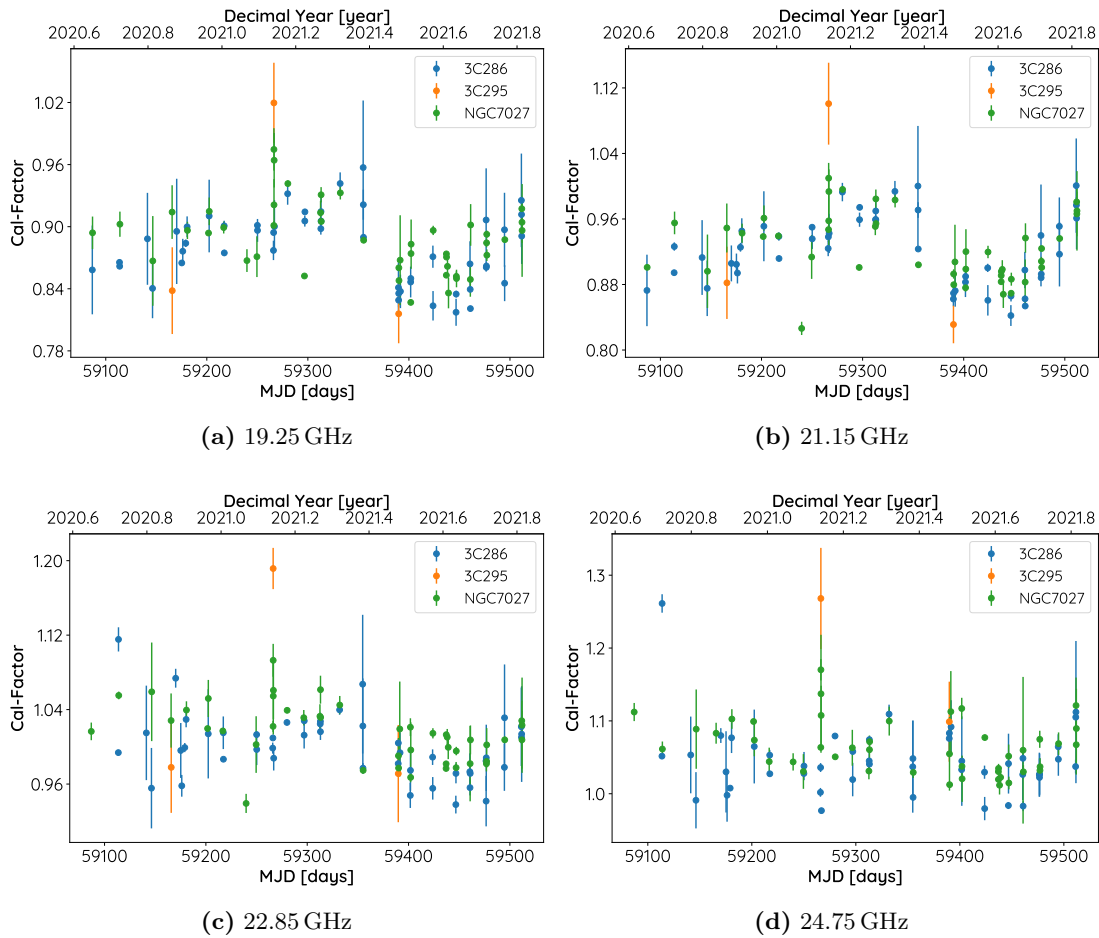
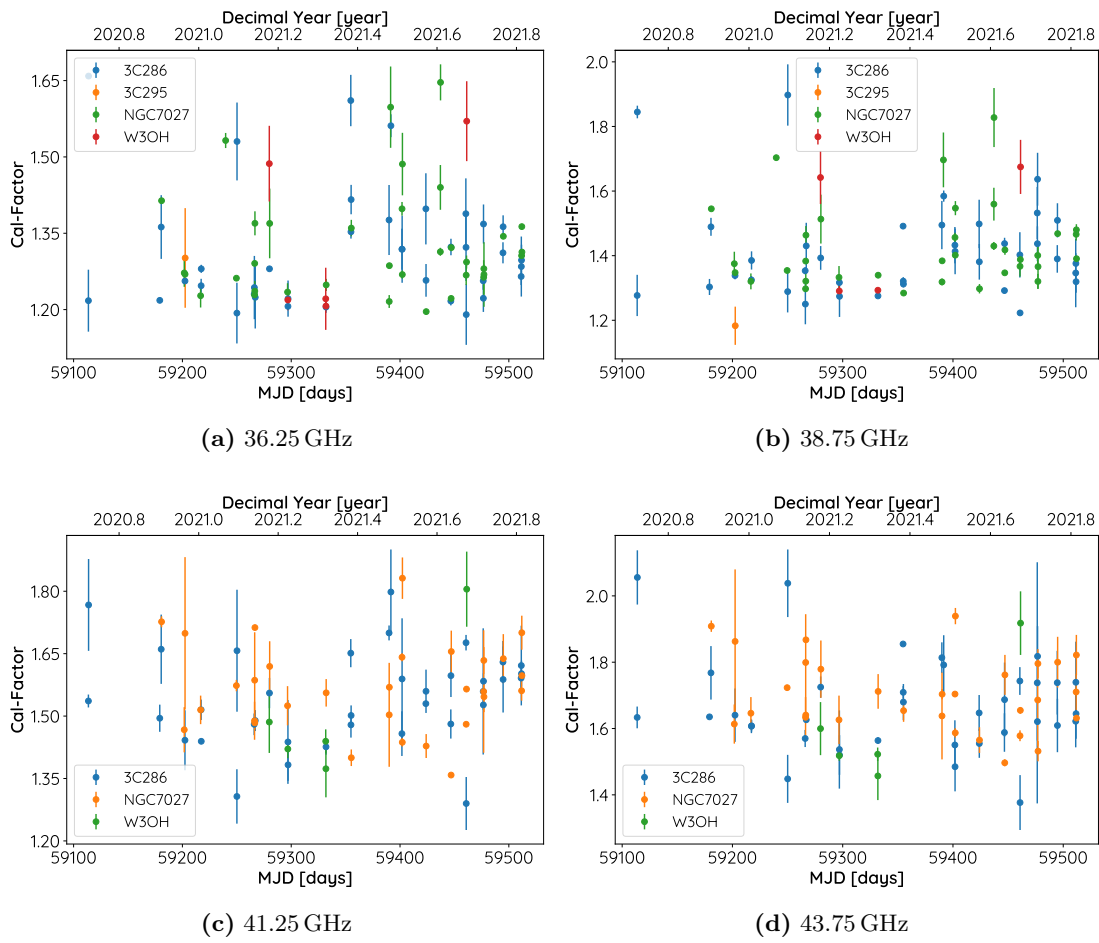


Fig. D.2: Calibration factor evolution for all sub-frequencies of the 7 mm receiver, namely 36.25 GHz, 38.75 GHz, 41.25 GHz, 43.75 GHz



Appendix E

Tables

E.1 Spectral Indices

Table E.1: Spectral Indices calculated from TELAMON data between 19 GHz and 25 GHz and between 19 GHz and 44 GHz.

Source	MJD [days]	Spectral Index (19 GHz-25 GHz)	Spectral Index (19 GHz-44 GHz)
J0214+5144	59114	-0.63 ± 0.60	-
J0214+5144	59165	-0.57 ± 1.04	-
J0214+5144	59180	-1.00 ± 0.17	-
J0214+5144	59312	-0.03 ± 0.21	-
J0214+5144	59331	-0.56 ± 0.07	-0.43 ± 0.16
J0214+5144	59494	-0.46 ± 0.10	-
J0222+4302	59114	$+0.04 \pm 0.17$	-0.09 ± 0.05
J0222+4302	59140	-0.06 ± 0.07	-
J0222+4302	59165	0.44 ± 0.21	-
J0222+4302	59180	-0.04 ± 0.07	0.09 ± 0.05
J0222+4302	59202	0.11 ± 0.08	-0.28 ± 0.07
J0222+4302	59216	0.02 ± 0.01	-0.08 ± 0.03
J0222+4302	59249	-0.27 ± 0.04	-0.26 ± 0.04
J0222+4302	59296	-0.25 ± 0.09	-0.32 ± 0.02
J0222+4302	59312	-0.06 ± 0.05	-
J0222+4302	59354	-0.85 ± 0.14	-
J0222+4302	59391	-0.30 ± 0.08	-
J0222+4302	59423	-0.07 ± 0.07	-0.11 ± 0.03
J0222+4302	59437	0.02 ± 0.04	0.01 ± 0.03
J0222+4302	59446	-0.22 ± 0.10	-0.39 ± 0.05
J0222+4302	59494	-0.25 ± 0.15	0.04 ± 0.08
J0303-2407	59140	-0.29 ± 0.44	-
J0303-2407	59202	0.13 ± 0.27	-
J0303-2407	59266	-0.03 ± 0.22	-
J0303-2407	59296	-0.63 ± 0.11	-

Table E.1 (Continued)

Source	MJD [days]	Spectral Index (19 GHz-25 GHz)	Spectral Index (19 GHz-44 GHz)
J0303-2407	59437	-1.00 ± 2.42	-
J0303-2407	59511	-0.73 ± 0.55	-
J0416+0105	59239	-0.13 ± 0.57	-
J0509+0541	59114	0.20 ± 0.09	0.11 ± 0.05
J0509+0541	59140	0.07 ± 0.08	-
J0509+0541	59165	0.54 ± 0.16	-
J0509+0541	59180	0.19 ± 0.08	0.14 ± 0.04
J0509+0541	59202	-0.06 ± 0.05	-0.06 ± 0.04
J0509+0541	59216	0.10 ± 0.04	-0.19 ± 0.04
J0509+0541	59239	0.24 ± 0.45	0.18 ± 0.09
J0509+0541	59249	0.23 ± 0.18	0.14 ± 0.12
J0509+0541	59266	0.11 ± 0.08	-
J0509+0541	59279	-0.35 ± 0.07	-0.27 ± 0.05
J0509+0541	59296	-0.43 ± 0.18	-0.30 ± 0.04
J0509+0541	59331	-0.46 ± 0.10	-0.44 ± 0.07
J0509+0541	59354	-0.58 ± 0.10	-0.44 ± 0.04
J0509+0541	59391	-0.35 ± 0.04	-0.12 ± 0.06
J0509+0541	59401	-0.27 ± 0.20	-0.22 ± 0.04
J0509+0541	59423	-0.09 ± 0.08	-0.21 ± 0.03
J0509+0541	59446	0.00 ± 0.12	-0.09 ± 0.05
J0509+0541	59460	0.22 ± 0.08	0.09 ± 0.07
J0509+0541	59494	-0.06 ± 0.02	-0.16 ± 0.08
J0509+0541	59511	-0.04 ± 0.04	-0.07 ± 0.04
J0650+2502	59279	-0.11 ± 0.25	-
J0650+2502	59312	-0.51 ± 0.52	-
J0650+2502	59331	0.01 ± 0.20	-
J1015+4926	59114	0.19 ± 0.34	-
J1015+4926	59140	-0.10 ± 0.08	-
J1015+4926	59180	-0.03 ± 0.19	0.00 ± 0.14
J1015+4926	59249	0.24 ± 0.14	-
J1015+4926	59266	-0.31 ± 0.18	-
J1015+4926	59312	-0.57 ± 0.23	-
J1015+4926	59331	-0.59 ± 0.27	-0.57 ± 0.22
J1015+4926	59401	-0.81 ± 0.51	-
J1015+4926	59460	-0.65 ± 0.35	-
J1058+2817	59312	-0.06 ± 0.17	-
J1058+2817	59331	-0.22 ± 0.42	-
J1104+3812	59114	-0.04 ± 0.03	-0.01 ± 0.07
J1104+3812	59140	-0.01 ± 0.19	-
J1104+3812	59165	0.17 ± 0.03	-
J1104+3812	59170	-0.35 ± 0.07	-
J1104+3812	59175	-0.03 ± 0.08	-
J1104+3812	59176	-0.21 ± 0.05	-
J1104+3812	59179	-0.24 ± 0.11	-0.08 ± 0.08
J1104+3812	59180	0.23 ± 0.01	0.24 ± 0.06
J1104+3812	59202	0.07 ± 0.05	0.11 ± 0.04

Table E.1 (Continued)

Source	MJD [days]	Spectral Index (19 GHz-25 GHz)	Spectral Index (19 GHz-44 GHz)
J1104+3812	59249	0.26 ± 0.12	0.22 ± 0.08
J1104+3812	59266	-0.17 ± 0.11	-0.11 ± 0.07
J1104+3812	59279	-0.24 ± 0.10	-0.28 ± 0.11
J1104+3812	59296	-0.00 ± 0.13	-0.16 ± 0.06
J1104+3812	59312	-0.25 ± 0.18	-
J1104+3812	59331	-0.15 ± 0.27	-0.28 ± 0.16
J1104+3812	59391	-0.15 ± 0.14	-0.24 ± 0.11
J1104+3812	59401	-	0.04 ± 0.06
J1104+3812	59423	-0.32 ± 0.24	-
J1104+3812	59446	0.14 ± 0.19	-
J1104+3812	59460	-0.02 ± 0.05	-0.03 ± 0.03
J1104+3812	59476	0.07 ± 0.20	0.12 ± 0.11
J1104+3812	59511	-0.38 ± 0.09	-0.17 ± 0.08
J1136+7009	59114	0.07 ± 0.39	-
J1136+7009	59180	-0.19 ± 0.30	-
J1136+7009	59202	-0.56 ± 0.09	-
J1136+7009	59249	0.01 ± 0.21	-
J1136+7009	59312	-0.23 ± 0.12	-
J1136+7009	59401	-0.43 ± 0.41	-
J1136+7009	59423	-0.07 ± 0.22	-
J1136+7009	59460	0.08 ± 0.39	-
J1217+3007	59114	-0.12 ± 0.22	-
J1217+3007	59140	0.09 ± 0.03	-
J1217+3007	59179	0.01 ± 0.14	-0.16 ± 0.04
J1217+3007	59180	0.20 ± 0.16	0.21 ± 0.08
J1217+3007	59216	-0.20 ± 0.05	-0.09 ± 0.05
J1217+3007	59266	0.22 ± 0.07	-0.05 ± 0.09
J1217+3007	59279	-0.12 ± 0.12	-0.07 ± 0.10
J1217+3007	59296	0.02 ± 0.25	0.13 ± 0.08
J1217+3007	59312	0.07 ± 0.02	-
J1217+3007	59354	-0.25 ± 0.13	-0.12 ± 0.07
J1217+3007	59401	0.07 ± 0.10	0.09 ± 0.05
J1217+3007	59446	-0.21 ± 0.16	-0.14 ± 0.14
J1217+3007	59460	-0.73 ± 0.08	-0.65 ± 0.10
J1217+3007	59511	-0.41 ± 0.07	-0.26 ± 0.21
J1221+3010	59296	0.28 ± 0.23	-
J1221+3010	59312	-0.92 ± 0.10	-
J1427+2348	59086	-0.40 ± 0.21	-
J1427+2348	59114	0.17 ± 0.17	0.11 ± 0.05
J1427+2348	59140	0.05 ± 0.08	-
J1427+2348	59165	0.45 ± 0.18	-
J1427+2348	59180	-0.16 ± 0.05	-0.06 ± 0.04
J1427+2348	59202	-0.09 ± 0.08	-0.06 ± 0.04
J1427+2348	59216	-0.13 ± 0.11	-
J1427+2348	59249	-0.30 ± 0.12	-
J1427+2348	59266	-0.05 ± 0.08	-

Table E.1 (Continued)

Source	MJD [days]	Spectral Index (19 GHz-25 GHz)	Spectral Index (19 GHz-44 GHz)
J1427+2348	59279	-0.13 ± 0.04	-0.09 ± 0.04
J1427+2348	59312	-0.06 ± 0.06	-
J1427+2348	59331	-0.09 ± 0.03	-0.12 ± 0.02
J1427+2348	59354	-0.05 ± 0.11	-0.23 ± 0.06
J1427+2348	59389	-0.33 ± 0.02	-
J1427+2348	59401	-0.23 ± 0.10	-0.12 ± 0.12
J1427+2348	59423	-0.30 ± 0.09	-0.10 ± 0.04
J1427+2348	59446	-0.38 ± 0.01	-
J1427+2348	59460	0.04 ± 0.11	-
J1427+2348	59476	0.08 ± 0.12	0.01 ± 0.09
J1518-2731	59312	-0.86 ± 0.33	-
J1518-2731	59331	-1.00 ± 0.30	-
J1555+1111	59086	0.17 ± 0.23	-
J1555+1111	59114	0.41 ± 0.21	-
J1555+1111	59165	-0.01 ± 0.18	-
J1555+1111	59180	-0.10 ± 0.19	-0.13 ± 0.12
J1555+1111	59202	0.04 ± 0.10	-
J1555+1111	59216	0.19 ± 0.50	-
J1555+1111	59249	-0.02 ± 0.03	-0.03 ± 0.03
J1555+1111	59266	0.23 ± 0.01	0.26 ± 0.01
J1555+1111	59279	-0.23 ± 0.31	-0.10 ± 0.22
J1555+1111	59312	0.13 ± 0.08	-
J1555+1111	59331	0.16 ± 0.05	0.16 ± 0.05
J1555+1111	59354	-0.03 ± 0.05	-0.11 ± 0.08
J1555+1111	59389	-0.24 ± 0.10	-
J1555+1111	59401	-0.05 ± 0.13	-
J1555+1111	59423	-0.22 ± 0.40	-
J1555+1111	59446	-0.50 ± 0.17	-
J1555+1111	59460	-0.09 ± 0.15	-
J1555+1111	59494	-0.59 ± 0.06	-
J1555+1111	59511	-0.41 ± 0.08	-
J1653+3945	59086	-0.30 ± 0.20	-
J1653+3945	59114	0.06 ± 0.06	-0.03 ± 0.02
J1653+3945	59140	-0.27 ± 0.06	-
J1653+3945	59165	-0.05 ± 0.11	-
J1653+3945	59180	-0.48 ± 0.13	-0.42 ± 0.06
J1653+3945	59202	-0.20 ± 0.07	-0.43 ± 0.05
J1653+3945	59216	-0.23 ± 0.09	-
J1653+3945	59249	-0.20 ± 0.03	-0.20 ± 0.03
J1653+3945	59266	-0.10 ± 0.19	-
J1653+3945	59279	-0.18 ± 0.06	-0.18 ± 0.03
J1653+3945	59312	-0.21 ± 0.01	-
J1653+3945	59331	-0.30 ± 0.02	-0.40 ± 0.04
J1653+3945	59354	-0.08 ± 0.05	-0.32 ± 0.05
J1653+3945	59389	-0.10 ± 0.05	-0.30 ± 0.05
J1653+3945	59423	-0.18 ± 0.13	-0.26 ± 0.02

Table E.1 (Continued)

Source	MJD [days]	Spectral Index (19 GHz-25 GHz)	Spectral Index (19 GHz-44 GHz)
J1653+3945	59446	-	-0.45 ± 0.05
J1653+3945	59460	-0.03 ± 0.06	-0.10 ± 0.05
J1653+3945	59476	-	-0.38 ± 0.06
J1653+3945	59494	-0.18 ± 0.03	-0.24 ± 0.03
J1653+3945	59511	-0.35 ± 0.05	-0.36 ± 0.04
J1728+5013	59086	0.07 ± 0.45	-
J1728+5013	59114	0.85 ± 0.40	-
J1728+5013	59165	-0.19 ± 0.14	-
J1728+5013	59180	-0.79 ± 0.18	-
J1728+5013	59202	-0.10 ± 0.21	-
J1728+5013	59249	0.11 ± 0.19	-
J1728+5013	59279	-0.11 ± 0.14	-
J1728+5013	59296	-0.23 ± 0.09	-
J1728+5013	59312	-0.32 ± 0.20	-
J1728+5013	59331	0.18 ± 0.23	-
J1728+5013	59389	0.08 ± 0.09	-
J1743+1935	59114	0.28 ± 0.16	-
J1743+1935	59140	-0.41 ± 0.10	-
J1743+1935	59165	-0.20 ± 0.22	-
J1743+1935	59180	-0.40 ± 0.21	-
J1743+1935	59249	-0.64 ± 0.17	-
J1743+1935	59266	-0.13 ± 0.17	-
J1743+1935	59279	-0.37 ± 0.29	-
J1743+1935	59312	-0.45 ± 0.07	-
J1743+1935	59331	-0.19 ± 0.09	-
J1743+1935	59354	-0.15 ± 0.02	-
J1743+1935	59389	0.58 ± 0.26	-
J1743+1935	59401	-0.31 ± 0.11	-
J1743+1935	59423	0.19 ± 0.10	-
J1743+1935	59460	-0.18 ± 0.13	-
J1743+1935	59494	0.16 ± 0.06	-
J1743+1935	59511	-0.10 ± 0.28	-
J1959+6508	59140	-0.09 ± 0.13	-
J1959+6508	59202	-0.08 ± 0.07	-0.02 ± 0.06
J1959+6508	59216	-0.11 ± 0.11	-
J1959+6508	59266	1.00 ± 0.07	-
J1959+6508	59279	0.08 ± 0.02	0.08 ± 0.05
J1959+6508	59312	-0.19 ± 0.20	-
J1959+6508	59389	0.32 ± 0.15	-
J1959+6508	59423	-0.34 ± 0.06	-
J1959+6508	59460	-0.01 ± 0.53	-
J1959+6508	59476	0.10 ± 0.20	-
J1959+6508	59511	0.29 ± 0.21	-
J2158-3013	59494	-0.81 ± 0.68	-
J2158-3013	59511	-1.00 ± 0.30	-
J2243+2021	59494	0.21 ± 0.04	-

Table E.1 (Continued)

Source	MJD [days]	Spectral Index (19 GHz-25 GHz)	Spectral Index (19 GHz-44 GHz)
J2243+2021	59511	0.32 ± 0.38	-
J2347+5142	59114	-0.10 ± 0.15	-
J2347+5142	59165	0.23 ± 0.18	-
J2347+5142	59180	0.12 ± 0.29	-
J2347+5142	59216	-0.57 ± 0.55	-
J2347+5142	59266	-0.32 ± 0.06	-
J2347+5142	59279	-1.00 ± 13.12	-
J2347+5142	59296	-0.34 ± 0.14	-
J2347+5142	59331	-0.33 ± 0.06	-
J2347+5142	59391	-0.57 ± 0.21	-
J2347+5142	59460	0.25 ± 0.23	-
J2347+5142	59511	-0.83 ± 0.57	-

Table E.2: Spectral Indices calculated from the F-GAMMA data using flux density values at 14.6 GHz, 23.05 GHz, 32 GHz and 43 GHz (full table available on the enclosed CD).

Source	Alt Name	MJD [days]	Spectral Index
J0006-0623	PKS0003-066	54380	-0.37 ± 0.03
J0006-0623	PKS0003-066	54672	0.24 ± 0.10
J0006-0623	PKS0003-066	54725	-0.19 ± 0.73
J0006-0623	PKS0003-066	54855	-0.08 ± 0.30
J0050-0929	PKS0048-097	55137	-0.14 ± 0.05
J0050-0929	PKS0048-097	55150	-0.23 ± 0.08
J0050-0929	PKS0048-097	55163	-0.12 ± 0.05
J0050-0929	PKS0048-097	56199	0.05 ± 0.25
...
...
J2327+0940	PKS325+093	56661	-0.03 ± 0.35
J2348-1631	PKS2345-16	54380	-0.17 ± 0.06

E.2 Intrinsic Modulation Indices

Table E.3: Intrinsic modulation indices derived from the F-GAMMA measurements at 23.05 GHz ($\overline{m}_{23\text{ GHz}}$) and 43 GHz ($\overline{m}_{43\text{ GHz}}$). For the sources where no modulation index is presented, there were not enough light curve data available to calculate the modulation index.

Source	Alt Name	$\overline{m}_{23\text{ GHz}}$	$\overline{m}_{43\text{ GHz}}$
J0006-0623	PKS 0003-066	0.117 ^{+0.033} _{-0.024}	0.174 ^{+0.092} _{-0.054}
J0050-0929	PKS 0048-097	0.187 ^{+0.037} _{-0.029}	0.204 ^{+0.071} _{-0.051}
J0102+5824	87GB 0059+5808	0.363 ^{+0.049} _{-0.040}	0.371 ^{+0.092} _{-0.065}
J0108+0135	PKS 0106+01	0.099 ^{+0.045} _{-0.028}	-
J0136+4751	BZQ J0136+4751	0.283 ^{+0.073} _{-0.052}	0.246 ^{+0.179} _{-0.087}
J0217+0144	PKS 0215+015	0.273 ^{+0.030} _{-0.026}	0.345 ^{+0.078} _{-0.057}
J0217+7349	HB89 0212+735	0.074 ^{+0.073} _{-0.048}	-
J0221+3556	B2 0218+35	0.147 ^{+0.034} _{-0.027}	0.142 ^{+0.162} _{-0.142}
J0222+4302	3C 66A	0.189 ^{+0.029} _{-0.024}	0.234 ^{+0.061} _{-0.045}
J0237+2848	HB89 0234+285	0.177 ^{+0.019} _{-0.016}	0.153 ^{+0.035} _{-0.027}
J0238+1636	HB89 0235+164	0.598 ^{+0.084} _{-0.066}	0.493 ^{+0.113} _{-0.081}
J0241-0815	NGC 1052	0.151 ^{+0.021} _{-0.017}	0.318 ^{+0.068} _{-0.051}
J0303+4716	4C+47.08	0.067 ^{+0.031} _{-0.021}	0.137 ^{+0.105} _{-0.055}
J0321+1221	PKS 0321+1221	0.000 ^{+0.068} _{-0.000}	-
J0336+3218	NRAO 140	0.356 ^{+0.111} _{-0.075}	0.485 ^{+0.269} _{-0.138}
J0339-0146	CTA 26	0.200 ^{+0.043} _{-0.033}	0.059 ^{+0.073} _{-0.048}
J0418+3801	3C 111	0.476 ^{+0.061} _{-0.050}	-
J0433+0521	3C 120	0.247 ^{+0.046} _{-0.035}	0.193 ^{+0.071} _{-0.047}
J0442-0017	NRAO 190	0.059 ^{+0.164} _{-0.059}	-
J0530+1331	PKS 0528+134	0.528 ^{+0.073} _{-0.058}	0.551 ^{+0.149} _{-0.100}
J0532+0732	PMN J0532+0732	0.017 ^{+0.073} _{-0.017}	-
J0607-0834	HB89 0605-085	0.030 ^{+0.026} _{-0.030}	-
J0654+4514	B3 0650+453	0.406 ^{+0.106} _{-0.075}	0.330 ^{+0.133} _{-0.086}
J0719+3307	B2 0716+33	0.167 ^{+0.205} _{-0.101}	0.403 ^{+0.370} _{-0.171}
J0721+7120	S5 0716+714	0.421 ^{+0.044} _{-0.037}	0.546 ^{+0.098} _{-0.075}
J0738+1742	PKS 0735+178	0.170 ^{+0.030} _{-0.025}	0.302 ^{+0.118} _{-0.073}
J0739+0137	HB89 0736+017	0.183 ^{+0.096} _{-0.056}	-
J0750+1231	PKS 0748+126	0.139 ^{+0.027} _{-0.021}	0.149 ^{+0.067} _{-0.041}
J0808-0751	PKS 0805-07	0.326 ^{+0.074} _{-0.053}	0.447 ^{+0.282} _{-0.141}
J0818+4222	B3 0814+425	0.277 ^{+0.035} _{-0.029}	0.303 ^{+0.077} _{-0.055}
J0824+5552	BZQ J0824+5552	0.175 ^{+0.074} _{-0.049}	-
J0830+2410	OJ 248	0.141 ^{+0.041} _{-0.030}	0.106 ^{+0.050} _{-0.031}
J0841+7053	S5 0836+710	0.214 ^{+0.026} _{-0.022}	0.513 ^{+0.127} _{-0.089}
J0920+4441	S4 0917+44	0.218 ^{+0.032} _{-0.026}	0.397 ^{+0.107} _{-0.075}
J0948+0022	PMN J0948+0022	0.260 ^{+0.048} _{-0.038}	0.350 ^{+0.100} _{-0.071}
J0958+6533	S4 0954+658	0.195 ^{+0.027} _{-0.023}	0.581 ^{+0.215} _{-0.133}
J1041+0610	PKS 1038+064	0.110 ^{+0.036} _{-0.025}	0.154 ^{+0.082} _{-0.046}
J1104+3812	MRK 421	0.162 ^{+0.028} _{-0.024}	0.287 ^{+0.080} _{-0.058}
J1130-1449	PKS 1127-14	0.245 ^{+0.033} _{-0.027}	0.380 ^{+0.084} _{-0.061}
J1159+2914	4C+29.45	0.417 ^{+0.053} _{-0.043}	0.393 ^{+0.107} _{-0.073}
J1217+3007	BZB J1217+3007	0.075 ^{+0.040} _{-0.033}	0.153 ^{+0.091} _{-0.062}

Table E.3 (Continued)

Source	Alt Name	$\bar{m}_{23} \text{ GHz}$	$\bar{m}_{43} \text{ GHz}$
J1221+2813	W Comae	0.186 ^{+0.044} _{-0.034}	0.231 ^{+0.081} _{-0.058}
J1224+2122	PG 1222+216	0.537 ^{+0.145} _{-0.097}	0.550 ^{+0.266} _{-0.144}
J1310+3220	OP+313	0.238 ^{+0.029} _{-0.024}	0.244 ^{+0.056} _{-0.042}
J1332-0509	PKS 1329-049	0.359 ^{+0.073} _{-0.054}	0.320 ^{+0.093} _{-0.064}
J1345+4452	B3 1343+451	0.041 ^{+0.060} _{-0.041}	0.223 ^{+0.352} _{-0.119}
J1357+1919	HB89 1354+195	0.075 ^{+0.054} _{-0.037}	-
J1408-0752	PKS B1406-076	0.085 ^{+0.050} _{-0.031}	0.197 ^{+0.203} _{-0.081}
J1504+1029	PKS 1502+106	0.511 ^{+0.082} _{-0.063}	0.753 ^{+0.217} _{-0.143}
J1512-0905	PKS 1510-089	0.378 ^{+0.041} _{-0.035}	0.265 ^{+0.047} _{-0.038}
J1522+3144	B2 1520+31	0.110 ^{+0.053} _{-0.037}	0.282 ^{+0.164} _{-0.092}
J1550+0527	PKS 1548+056	0.000 ^{+0.040} _{-0.000}	-
J1553+1256	PKS 1551+130	0.137 ^{+0.068} _{-0.050}	-
J1613+3412	1611+343	0.083 ^{+0.029} _{-0.021}	0.251 ^{+0.129} _{-0.071}
J1635+3808	4C+38.41	0.258 ^{+0.024} _{-0.021}	-
J1638+5720	S4 1637+57	0.069 ^{+0.054} _{-0.037}	-
J1642+6856	8C 1642+690	0.144 ^{+0.045} _{-0.032}	-
J1653+3945	MRK 501	0.084 ^{+0.013} _{-0.011}	0.224 ^{+0.042} _{-0.033}
J1733-1304	PKS 1730-13	0.212 ^{+0.024} _{-0.021}	0.301 ^{+0.066} _{-0.049}
J1748+7005	S4 1749+70	0.067 ^{+0.087} _{-0.058}	-
J1751+0939	OT+081	0.351 ^{+0.041} _{-0.035}	0.369 ^{+0.073} _{-0.055}
J1800+7828	S5 1803+78	0.090 ^{+0.015} _{-0.013}	0.104 ^{+0.049} _{-0.037}
J1806+6949	3C 371	0.074 ^{+0.017} _{-0.014}	0.067 ^{+0.082} _{-0.060}
J1824+5651	4C+56.27	0.171 ^{+0.031} _{-0.024}	0.251 ^{+0.101} _{-0.062}
J1848+3219	B2 1846+32A	0.354 ^{+0.060} _{-0.047}	0.457 ^{+0.137} _{-0.093}
J1849+6705	S4 1849+67	0.290 ^{+0.041} _{-0.033}	0.304 ^{+0.093} _{-0.065}
J1927+7358	8C 1928+738	0.079 ^{+0.034} _{-0.023}	-
J2025-0735	PKS 2023-07	0.230 ^{+0.034} _{-0.028}	0.270 ^{+0.063} _{-0.046}
J2031+1219	PKS 2029+121	0.077 ^{+0.058} _{-0.036}	-
J2129-1538	PKS 2126-158	0.000 ^{+0.352} _{-0.000}	-
J2143+1743	OX 169	0.192 ^{+0.032} _{-0.027}	0.198 ^{+0.066} _{-0.050}
J2147+0929	PKS 2144+092	0.289 ^{+0.050} _{-0.040}	0.276 ^{+0.105} _{-0.068}
J2158-1501	PKS 2155-152	0.092 ^{+0.036} _{-0.024}	0.231 ^{+0.171} _{-0.079}
J2203+1725	PKS 2201+171	0.330 ^{+0.087} _{-0.061}	0.309 ^{+0.195} _{-0.098}
J2203+3145	PKS 2201+315	0.108 ^{+0.021} _{-0.017}	0.215 ^{+0.074} _{-0.049}
J2229-0832	PKS 2227-08	0.325 ^{+0.062} _{-0.047}	0.346 ^{+0.141} _{-0.088}
J2232+1143	CTA 102	0.279 ^{+0.029} _{-0.025}	0.274 ^{+0.047} _{-0.037}
J2327+0940	PKS 325+093	0.432 ^{+0.080} _{-0.061}	0.304 ^{+0.125} _{-0.081}
J2348-1631	PKS 2345-16	0.217 ^{+0.078} _{-0.051}	0.274 ^{+0.360} _{-0.123}

E.3 Raw TELAMON Flux Density Data

Table E.4: Raw TELAMON flux density values for all sources, frequencies and epochs. These data were used for the analysis in this thesis (full table available on the enclosed CD).

Source	Frequency [GHz]	Epoch Date	Flux Density [Jy]	MJD [days]
J1104+3812	21.15	2020-08-25	0.4585 ± 0.0107	59086.7281
J1104+3812	19.25	2020-08-25	0.3546 ± 0.0080	59086.7281
J1221+2813	22.85	2020-08-25	0.6918 ± 0.0078	59086.7482
J1221+2813	24.75	2020-08-25	0.7211 ± 0.0087	59086.7482
J1221+2813	21.15	2020-08-25	0.7113 ± 0.0118	59086.7482
J1221+2813	19.25	2020-08-25	0.6705 ± 0.0139	59086.7482
J1221+2813	22.85	2020-08-25	0.5792 ± 0.0074	59086.7517
J1221+2813	24.75	2020-08-25	0.5989 ± 0.0078	59086.7517
...
...
J0035+5950	22.85	2021-10-24	0.0681 ± 0.0022	59512.0675
J0035+5950	24.75	2021-10-24	0.0634 ± 0.0050	59512.0675

Acknowledgements

I would first like to thank my thesis advisor Prof. Dr. Matthias Kadler of the Chair of Astronomy at the Julius-Maximilians-University of Würzburg. The door to his (virtual) office was always open whenever I had a question about my research or writing.

I would also like to thank Petra Benke, Andrea Gokus, Jonas Heßdörfer, Georgios Paraschos, Florian Rösch, Jonas Sinapius and Philip Weber who were involved in the TELAMON observations. Special thanks to Jonas Heßdörfer and Florian Rösch for proof-reading this thesis. They always had an open ear for my questions. Without their participation and input, the work could not have been done successfully. Additionally, I would like to thank everyone else at the Chair of Astronomy in Würzburg, including the chair holder Prof. Dr. Karl Mannheim, for always providing a productive work environment.

On top of that, I'd like to thank Uwe Bach and Alex Kraus from the Max-Planck-Institute for Radio Astronomy in Bonn/Effelsberg for introducing me to the observations with the Effelsberg 100-m telescope and for their helpful input on the data reduction. Special thanks go to the Effelsberg operators for their help during the observing sessions.

Finally, I must express my very profound gratitude to my parents for providing me with unfailing support and continuous encouragement throughout my years of study and through the process of researching and writing this thesis. And Thanks to Paula, for all her love and support.

This accomplishment would not have been possible without all of them. Thank you.

This work is based on observations with the Effelsberg 100-m telescope. This research has made use of NASA's Astrophysics Data System and of the NASA/IPAC Extragalactic Database (NED), which is operated by the Jet Propulsion Laboratory, California Institute of Technology, under contract with the National Aeronautics and Space Administration.

Declaration of Authorship

I, Florian Eppel, declare that this thesis titled, ‘Variability Study of High Peaked BL Lac Objects at Millimeter Wavelengths’ and the work presented in it are my own. I confirm that:

- Where any part of this thesis has previously been submitted for a degree or any other qualification at this University or any other institution, this has been clearly stated.
- Where I have consulted the published work of others, this is always clearly attributed.
- Where I have quoted from the work of others, the source is always given. With the exception of such quotations, this thesis is entirely my own work.
- I have acknowledged all main sources of help.
- Where the thesis is based on work done by myself jointly with others, I have made clear exactly what was done by others and what I have contributed myself.

Signed:

Date:
